

Global Optimization in Conceptual Process Design

Dissertation

zur Erlangung des akademischen Grades

Doktoringenieur

(Dr.-Ing.)

von Dipl.-Ing. Christian Kunde

geb. am 05.05.1986 in Schkeuditz

genehmigt durch die Fakultät für Elektrotechnik und

Informationstechnik

der Otto-von-Guericke-Universität Magdeburg

Gutachter: Prof. Dr. A. Kienle

Prof. Dr. A. Seidel-Morgenstern

Jun.-Prof. Dr. D. Michaels

Promotionskolloquium am 29.05.2017

Abstract

Mathematical optimization is increasingly employed to solve chemical process design tasks. Process design and process analysis tasks typically yield non-linear problems with many continuous decision variables like operating parameters and discrete decision variables like structural degrees of freedom. Solving these mixed-integer nonlinear programs (MINLP) is very hard, in general. Most often, heuristic or local optimization methods are employed to find good solutions for MINLP. However, finding a global solution is not guaranteed with those methods, making process insight or design decisions prone to error due to bad local solutions. In contrast, global optimization algorithms like branch-and-bound-methods are able to prove that solutions are globally optimal but require more computational effort, in some cases prohibitively so. In this work, capabilities for process analysis and process design using global optimization are extended for several applications. Suitable model formulations for solving the considered problems with standard software are provided, exploiting properties of according models. A method for evaluating computational effort of solving global optimization problems is proposed, providing comparability of results through statistical analysis. Multistage separation is covered in the first set of applications. While standard approaches focus on countercurrent designs, such restrictions are removed here to allow more general configurations. Melt crystallization for a binary mixture is studied as a benchmark process for multistage separation networks. The parameter dependence of globally optimal solutions is studied and used to derive simple generalized design rules for multistage separation. The initial results are extended to multistage solution crystallization and multistage filtration, demonstrating the generalization of results to different separation technologies. As the second application, globally optimal flowsheet selection for conceptual process design is studied with an exemplary process combining distillation and melt crystallization units.

Zusammenfassung

Mathematische Optimierung wird zunehmend für die Prozessentwicklung in der chemischen Verfahrenstechnik eingesetzt. Dabei führen kontinuierliche Entscheidungsvariablen wie Betriebsparameter und diskrete Entscheidungsvariablen wie strukturelle Freiheitsgrade oft zu nichtlinearen Optimierungsproblemen. Gemischt-ganzzahlige nichtlineare Optimierungsprobleme (MINLP) sind in der Regel sehr schwierig zu lösen. In den meisten Fällen werden heuristische oder lokale Optimierungsmethoden verwendet, um gute Lösungen für MINLP zu finden. Allerdings können solche Methoden nicht garantieren ein globales Optimum zu finden, wodurch Prozessverständnis und Entwicklungsentscheidungen fehleranfällig gegenüber schlechten lokalen Lösungen werden. Im Gegensatz dazu ermöglichen Algorithmen für globale Optimierung, beispielsweise sogenannte Branch-and-Bound-Methoden, den Nachweis, dass eine Lösung global optimal ist. Dies erfordert jedoch einen deutlich höheren, in manchen Fällen nicht vertretbaren, Rechenaufwand. In dieser Arbeit wird die Anwendbarkeit von globaler Optimierung für Prozessanalyse und Prozessentwicklung verschiedener verfahrenstechnischer Prozesse erweitert. Für die entsprechenden Anwendungen werden Modellformulierungen bereitgestellt, die durch Ausnutzung der jeweiligen Modelleigenschaften einen vertretbaren Rechenaufwand für globale Optimierung mittels Standardsoftware erlauben. Eine Methode zur Bewertung des Rechenaufwands für die globale Optimierung verschiedener Modellformulierungen wird vorgeschlagen. Vergleichbarkeit zwischen den Modellformulierungen wird durch statistische Analyse der Ergebnisse ermöglicht. Als erstes Anwendungsgebiet werden mehrstufige Trennprozesse betrachtet. Gegenstromkonfigurationen stellen den üblichen Ansatz für diese Aufgabe dar. Diese Beschränkung wird hier aufgehoben, um auch allgemeinere Konfigurationen zu ermöglichen. Als Benchmark-Prozess für mehrstufige Trennprozesse wird die Schmelzkristallisation von Zweistoffgemischen betrachtet. Die Parameterabhängigkeit von global optimalen Lösungen wird untersucht und genutzt, um einfache, allgemeine Entwurfsregeln für mehrstufige Trennprozesse abzuleiten. Die Ergebnisse des Benchmark-Prozesses werden auf mehrstufige Lösungskristallisation und mehrstufige Filtration erweitert. Das zweite Anwendungsgebiet ist die Fließbildauswahl für den konzeptionellen Prozessentwurf mittels globaler Optimierung anhand eines Beispielprozesses, in dem Destillation und Schmelzkristallisation verwendet werden.

Contents

1	Introduction -	
	Hierarchical Design Frameworks and Global Optimization	1
2	Evaluating Computational Effort of Global Optimization	9
2.1	Introduction	10
2.2	Reproducibility	10
2.2.1	Single Core Operation	11
2.2.2	Multi Core Operation	12
2.3	Influences of Solver Characteristics	13
2.3.1	BARON/CPLEX/CONOPT	14
2.3.2	Other Solvers	14
2.4	Conclusion	14
3	Analysis of Multistage Separation Networks	17
3.1	Introduction	18
3.2	Melt Crystallization	18
3.2.1	Process Model	19
3.2.2	Reformulation	25
3.2.3	Redundant Configurations	27
3.2.4	Computational Studies	30
3.2.5	Conclusion	48
3.3	Solution Crystallization	49
3.3.1	Process Model	50
3.3.2	Computational Studies	56
3.3.3	Conclusion	66
3.4	Filtration	68

3.4.1	Process Model	68
3.4.2	Computational Studies	74
3.4.3	Conclusion	80
4	Flowsheet Selection for Hybrid Distillation/Melt Crystallization Processes	81
4.1	Introduction	82
4.2	Process Model	82
4.2.1	Distillation Column	84
4.2.2	Properties of Distillation Model	87
4.2.3	Countercurrent Crystallizer Cascade	91
4.2.4	Flowsheet Options	93
4.2.5	Objective Function	95
4.3	Computational Results	96
4.3.1	Effect of Monotonicity Constraints on Computation Time	97
4.3.2	Comparison of Mixed-Integer Design Models	99
4.3.3	Comparison with Fenske-Underwood-Gilliland	100
4.3.4	Optimal Flowsheet Results	101
4.4	Conclusion	103
5	Conclusion and Future Perspectives	105
A	Integral Distribution Coefficient for Melt Crystallization	107
B	A Property of Multicomponent Distillation	109
C	Reference Distillation Model	111
D	Fenske-Underwood-Gilliland Method for Global Optimization	113
	Bibliography	117

Chapter 1

Introduction -

Hierarchical Design Frameworks
and Global Optimization

Mathematical optimization is increasingly used to solve chemical process synthesis and process design tasks. At the same time, complex process design and process intensification tasks typically lead to optimization problems that are very difficult to solve due to non-linearity as well as many continuous and discrete decision variables. Continuously increasing capabilities of both computers and algorithms have led to many new design methods based on mathematical programming beside the more traditional methods employing heuristics and shortcut evaluation. Careful consideration is required on which method to apply to a given task due to the specific strengths of each method. Heuristics and shortcut evaluation are computationally easy to solve but often require restrictive assumptions resulting in limited model validity. Mathematical programming methods generally require more computational effort but can be applied to more detailed problems. However, except for specific model classes, they do not provide a measure for the quality of solutions or guarantee to find the best solution to a given optimization problem.

Hierarchical Design Frameworks The engineering effort of complex design tasks may be addressed by combining methods with different degrees of accuracy and modeling detail [Douglas, 1985, Grossmann, 1985]. Solving design problems on a low level of detail for the most fundamental decisions allows for discarding poor designs on that level and significantly reducing the design space. The problem is then solved again in subsequent steps for successively smaller design spaces but with added layers of detail. Thereby, the effort of making needlessly detailed decisions for poor designs is avoided. This concept of a hierarchical decision procedure for process design was proposed in [Douglas, 1985, 1988], stating therein that it followed similar ideas from the artificial intelligence literature [e. g., Sacerdoti, 1974].

Various research groups later followed the hierarchical approach to process design [e. g., Sargent, 1998, Daichendt and Grossmann, 1998, Kravanja et al., 2005]. The advantages of using differently detailed variants of a model for their respective purposes within hierarchical design approaches are discussed in [Sargent, 2005], emphasizing that *“there is no such thing as a perfect model, and all that we can hope to do is predict the evolution of a limited set of properties of the system of interest with reasonable accuracy”*.

More recently, the focus shifted from a hierarchy of decisions to a hierarchy of modeling detail as the approach was formalized in a general process synthesis framework [Kossack et al., 2006, Marquardt et al., 2008, Kossack et al., 2008]. This is still matching previous work due to the appropriate modeling detail being determined by the purpose of a model and vice versa. Process alternatives are screened quickly based on low-detail models and poor designs are discarded. The remaining problem is much smaller allowing it to be solved with more detailed models to further reduce the search space for the best design. This work is summarized in the context of conceptual design of distillation-based hybrid separation processes in a recent review [Skiborowski et al., 2013]. A similar approach is used in [Franke et al., 2004, 2008] for the design of hybrid separation processes based on distillation and melt crystallization and in [Kaspereit et al., 2012] for the design of hybrid processes for the production of pure enantiomers.

Hierarchical design methods offer the potential of significantly reducing the effort of solving engineering problems. However, using models with different levels of detail may change the values of optimal design and operating parameters. In other words, decisions based on simple models in early steps of a hierarchical design framework may not be valid when moving to more detailed models. Strategies for model simplification that conserve optimal designs [e. g., Daichendt and Grossmann, 1998] and optimization under uncertainty are possible ways to consider model inaccuracies. A second way decisions in hierarchical design frameworks are adversely affected is by failing to identify the best solution of optimization problems with multiple local optima. Optimization algorithms terminating in poor local solutions may lead to good design options being discarded, also see [Nallasivam et al., 2013]. The problem of poor local optima is addressed in this thesis by making decisions based on globally optimal solutions. However, as outlined below, applying deterministic global optimization to process design tasks as demonstrated in this work requires additional consideration due to significant computational effort.

Deterministic Global Optimization Process design and process synthesis tasks typically correspond to optimization problems of the form

$$\begin{aligned} \min \quad & f(\mathbf{x}) \\ & \mathbf{g}(\mathbf{x}) \leq \mathbf{0} \\ & \mathbf{x} \in X \end{aligned} \tag{1.1}$$

with objective function $f : X \rightarrow \mathbb{R}$, constraints $\mathbf{g} : X \rightarrow \mathbb{R}^m$ and set $X \subset \mathbb{R}^n$ that often include integer restrictions. The aim is to find globally optimal solutions \mathbf{x}^* such that

$$f(\mathbf{x}^*) \leq f(\mathbf{x}) \text{ for all } \mathbf{x} \in S. \tag{1.2}$$

where $S = \{\mathbf{x} \in X : \mathbf{g}(\mathbf{x}) \leq \mathbf{0}\}$ is the feasible set.

It should be noted that Equation (1.1) includes problem classes in which any local solution $\bar{\mathbf{x}}$

$$f(\bar{\mathbf{x}}) \leq f(\mathbf{x}) \text{ for all } \mathbf{x} \in S : \|\bar{\mathbf{x}} - \mathbf{x}\|_2 < \varepsilon, \quad \varepsilon > 0, \tag{1.3}$$

also represent a global solution, e.g. linear or convex optimization. A simple example for a convex optimization problem is depicted in Figure 1.1. Efficient algorithms for solving optimization problems for local solutions are widely available [Biegler and Grossmann, 2004, Grossmann and Biegler, 2004].

In contrast to that, the scope of global optimization is solving problems with multiple local optima as sketched in Figure 1.2a, which typically is a difficult task. Methods for global optimization strongly depend on the structure of the problem. Specialized algorithms for finding solutions of various highly structured optimization problems are described in [Locatelli and Schoen, 2013,

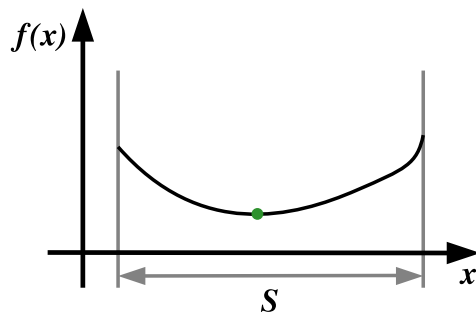
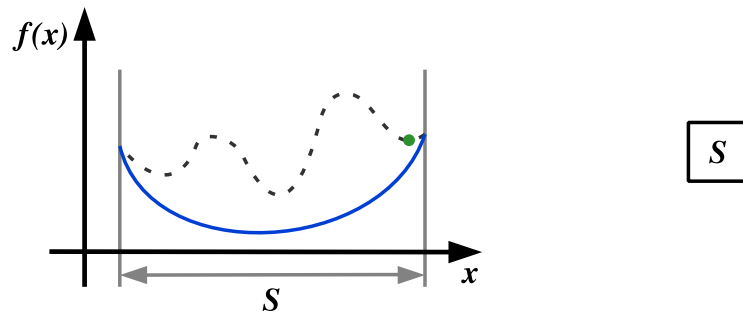
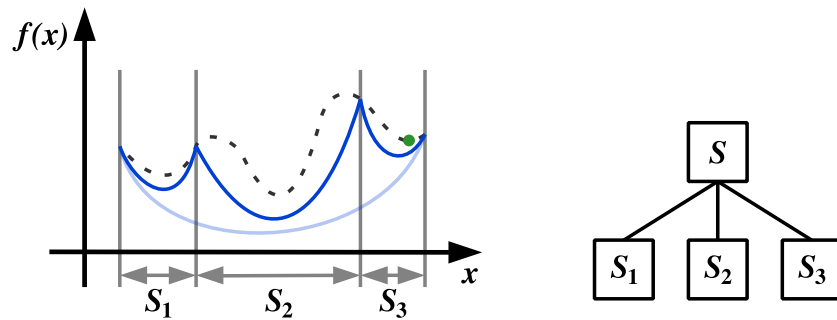


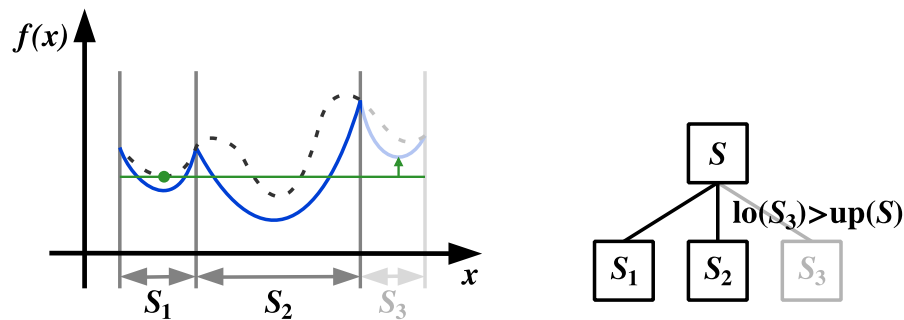
Figure 1.1: Convex function $f(x)$ on convex set S with global minimum (dot).



(a) Calculation of lower bound (solid line) of objective function $f(x)$ (dashed line) for original set S and a known feasible or locally optimal solution (dot). Objective function values are unknown except for selected points.



(b) Branching. Improved lower bounds for subsets resulting from subdivision of S .



(c) Updating best known feasible solution (dot). Discarding subsets not able to improve best known feasible solution further.

Figure 1.2: Illustration of selected branch-and-bound algorithm steps with tree-like representation for subdivisions of set S . Solid lines represent underestimators for objective function $f(x)$ (dashed line). Objective function values are unknown except for selected points.

Horst and Tuy, 1996]. A commonly applied method for solving more general optimization problems is given by branch-and-bound (BB) algorithms [Locatelli and Schoen, 2013], e.g. BARON [Tawarmalani and Sahinidis, 2005], ANTIGONE [Misener and Floudas, 2014] and SCIP [Achterberg, 2007]. A graphical representation of selected BB steps is given in Figure 1.2. In short, BB algorithms calculate feasible solutions and lower bounds of $f(\mathbf{x})$ for subsets of S (Figure 1.2a). Those subsets are successively subdivided in order to improve the quality of the bounds (Figure 1.2b). Subsets are discarded if their lower bound is equal to or larger than the best known feasible solution, i.e. if it is guaranteed that those subsets do not contain better solutions (Figure 1.2c). This is repeated until all subsets are discarded and the best feasible solution is returned as a global optimum. Note that function values are only evaluated and known at a limited number of points although fully depicted in Figure 1.2. Lower bound computation is an essential step and therefore an extensive topic in BB algorithms. For a detailed description, the reader is referred to [Locatelli and Schoen, 2013]. In general, an original problem that is hard to solve is replaced by a more simple problem to obtain a globally valid lower bound to the original optimal solution. A common method is to replace nonconvex objective functions by convex underestimators (e.g. solid line in Figure 1.2a) and nonconvex sets by convex relaxations. Resulting convex problems are then solved globally with available algorithms. Underestimators and relaxations are more accurate on smaller subsets, allowing to discard suboptimal or infeasible subsets sooner. Therefore, BB algorithms usually apply domain reduction strategies to reduce the size of subsets in addition to the subdivision strategy illustrated in Figure 1.2b. Choosing constraints that require less variables may also result in smaller subsets and thus less computational effort. A third option to reduce subset size is adding redundant constraints, i.e. constraints that do not change the original feasible set S but are easy to evaluate (e.g. adding $n \leq 2$ to $a^n + b^n = c^n$ with $a, b, c, n \in \mathbb{Z}^+$ according to Fermat's Last Theorem). General branch-and-bound software may not recognize the special structure or specific properties of a given optimization problem. Therefore, problem specific properties may be exploited to improve the computational performance of standard branch-and-bound algorithms.

It should be noted that high complexity, and consequently computational ef-

fort, prevents many problems from being solved with BB algorithms [Locatelli and Schoen, 2013]. In practice, such problems may be approached by searching for good local solutions with heuristic methods, e. g. multistart heuristics. Although these methods may find good solutions, they do not give global bounds to evaluate the quality of solutions or guarantee to find a global solution. A brief introduction of widely-used methods for such problems is given in [Biegler and Grossmann, 2004, Grossmann and Biegler, 2004]. Heuristic methods are not studied further here, since the scope of this work is to extend capabilities to globally solve engineering problems with deterministic methods.

Outline of the Thesis As discussed above, it is computationally expensive to solve complex design tasks directly for all necessary decisions. The direct approach is currently only tractable, at best, for local or stochastic algorithms. As an alternative strategy, hierarchical design frameworks allow utilizing deterministic global optimization whenever it is computationally feasible and switching to other methods when the computational effort becomes too excessive. With this approach, it is guaranteed that the most fundamental decisions for design tasks are not adversely affected by poor local optima. In particular, identifying global optima renders repeated optimization for the same problem obsolete since, by definition, no better solution exists.

In this thesis, the application of deterministic global optimization to conceptual, first principles process models within hierarchical design frameworks is proposed. By exploiting problem specific properties, model formulations are provided that allow analysis and design of selected processes based on globally optimal solutions with more detailed models than previously published. Chapter 2 covers the topic of evaluating model formulations with regard to suitability for branch-and-bound algorithms. The methods developed in that chapter are used in following chapters for model evaluation. In Chapter 3, multistage separation networks are analyzed based on globally optimal solutions. Usual restrictions to countercurrent configurations are removed to allow for alternative network designs. Suitable model formulations are provided and results are compared for three different separation processes. Chapter 4 comprises a case study for the process design task of flowsheet selection, again

based on globally optimal solutions. Conclusions and future perspectives follow in Chapter 5.

Parts of this work are published in the following contributions:

[Ballerstein et al., 2011, 2014, Kunde and Kienle, 2015, Kunde et al., 2016, Mertens et al., 2016].

Chapter 2

Evaluating Computational Effort of Global Optimization

2.1 Introduction

In the following chapters, model formulations suitable for global optimization will be provided and evaluated. A measure for computational performance is required for evaluating model formulations and may be given by the CPU time needed for an optimization task. The CPU time needed for a given task depends on many parameters, starting with the hardware and software configuration of a computer system. In context of branch-and-bound algorithms, the properties of an optimization problem are also important. The dimension and solution landscape of the optimization problem, the applied algorithm as well as desired numerical accuracy will influence the required CPU time. Keeping all other influences fixed still leaves random effects like memory access times. In this chapter, the suitability of the CPU time as a measure for computational performance is assessed. GAMS 24.6.1 (Linux, 64bit) is applied with the global solver BARON 15.9.22 utilizing CPLEX 12.6.3.0 and CONOPT 3.17A as sub-solvers on a standard desktop computer with an Intel(R) Core(TM) i7-3770 CPU @ 3.40GHz. The CPU time used in the following studies is the CPU time reported by BARON.

Note that quantitative results presented in this work are only expected to be comparable to results obtained with identical or very similar hardware and software configurations under equal conditions.

2.2 Reproducibility

The capability to reproduce results keeping the entire setup constant is checked by repeatedly solving the nonlinear problem “gsg_0001” from MINLPLib2 [MIN, Bussieck et al., 2003], a library providing benchmark problems for mixed-interger nonlinear programming and nonlinear programming. A global solution to the optimization problem is calculated beforehand and provided as an initial point. Solver options are kept at default values except for reserved memory (GAMS option “*m.workspace=2*1024*”), relative gap between primal and dual solution (GAMS option “*optcr=0.0001*”) and local search before branching (BARON option “*NumLoc 0*”).

Since prior information on the distribution of required CPU times is not avail-

able, information on percentiles of this distribution is evaluated. A short overview on this method is given in [Schmid and Huber, 2014]. The probability of some percentile P_p lying between two values of a sorted list of random samples x_i , $i = 1, \dots, N$ is described by a binomial distribution. The confidence P that a percentile P_p lies above (or below) a sample x_m for a number of measurements N is then calculated as

$$\begin{aligned} P\{x_m \leq P_p\} &= P\{x_{N-m+1} \geq P_{1-p}\} \\ &= 1 - \sum_{k=0}^{m-1} \binom{N}{k} p^k (1-p)^{N-k}. \end{aligned} \quad (2.1)$$

2.2.1 Single Core Operation

In Figure 2.1, the distribution of 500 samples for the CPU time required for solving “gsg_0001” [MIN, Bussieck et al., 2003] is plotted together with 99 % confidence intervals for the median $M = P_{0.50}$, $P_{0.02275}$ and $P_{0.97725}$ of the true CPU time distribution. This means, with 99 % confidence, less than 5 % of the distribution lies outside the range of 223.51 s to 225.3 s. These error bounds are small compared to the median value. CPU time measurements for a constant setup are therefore considered reproducible.

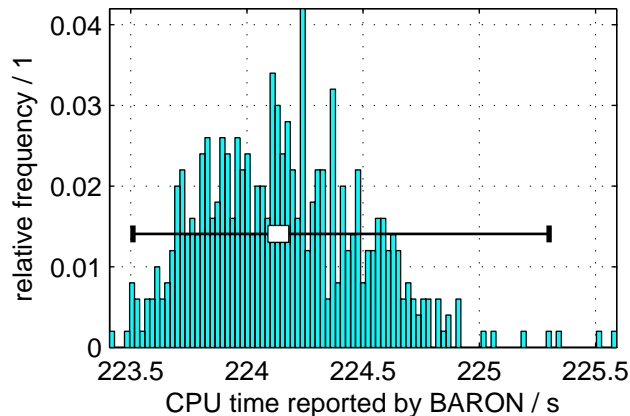


Figure 2.1: Sample distribution of CPU time reported by BARON for solving “gsg_0001” and 99 % confidence intervals for the median (white box), $P_{0.02275}$ and $P_{0.97725}$ (whiskers) of the true CPU time distribution.

Note that $P_{0.02275}$ and $P_{0.97725}$ correspond to $\mu - 2\sigma$ and $\mu + 2\sigma$ for a normal distribution, with mean value μ and standard deviation σ . However, the sample

distribution does not resemble a normal distribution and therefore calculations based on that assumption are not expected to be accurate. A larger sample size would be necessary to validate this observation.

2.2.2 Multi Core Operation

The CPU of the utilized computer has four processor cores. This can be facilitated to reduce computational effort by spreading calculations over different cores. To study the influence of multi core operation on the CPU time distribution, instances of “gsg_0001” [MIN, Bussieck et al., 2003] are solved repeatedly in four parallel queues. Only instances of the first queue are taken as samples, so no pair of samples is calculated at the same time.

In Figure 2.2, the distribution of 500 samples for the CPU time required for solving “gsg_0001” in parallel with three other instances of the same task is plotted together with 99 % confidence intervals for the median $M = P_{0.50}$, $P_{0.02275}$ and $P_{0.97725}$.

The median CPU time is higher for multi core operation than for single core

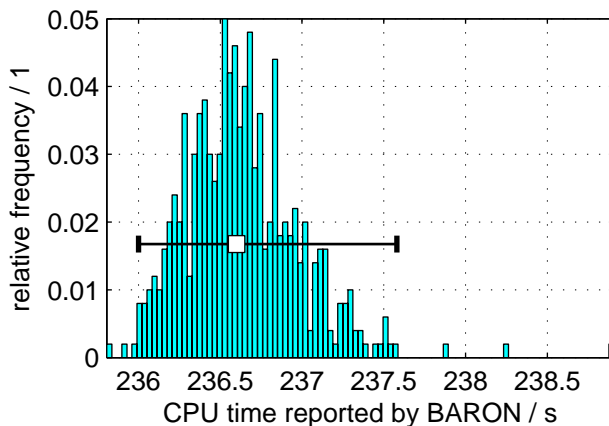


Figure 2.2: Sample distribution of CPU time reported by BARON for solving “gsg_0001” in parallel with three other tasks and 99 % confidence intervals for the median (white box), $P_{0.02275}$ and $P_{0.97725}$ (whiskers) of the true CPU time distribution.

operation. However, in both cases the range of values deviates little from the respective median. Therefore, solving optimization tasks in parallel is deemed suitable for comparing CPU times as long as the number of active queues is

constant.

It should be noted that there is a BARON option to utilize parallelization for solving linear subproblems, which is generally the step with the highest overall CPU time demand. This option is not further studied here, since only cases which allow running entirely parallel instances of GAMS are considered in this work.

2.3 Influences of Solver Characteristics

Beside obvious factors such as hardware, software, solver parameters, dimension of the problem and characteristics of the solution landscape, the computational performance of branch-and-bound algorithms also depends on seemingly performance neutral properties. For instance, branching requires prioritizing variables over others. Insufficient information for distinguishing possible choices may be resolved with information from the programming code. Thus the order in which variables are declared in the programming code may influence branching decisions and therefore computation time significantly although it does not change the optimization problem itself. So whenever some performance indicator like total number of iterations or CPU time is used to evaluate the computational effort for an optimization problem, the result is also influenced by those seemingly neutral properties. In [Koch et al., 2011], this behavior, called “performance variability”, is described for solving mixed-integer programs. An indicator for the performance variability is introduced in [Koch et al., 2011] by the standard deviation divided by the average. To take non-normal distributions into account, percentiles as defined above are used in this thesis also for characterization of performance variability. Performance variability is illustrated in the following for random permutations of the order of declaration for equality and inequality conditions of “gsg_0001”, solved in four parallel queues. Solver options are kept at default values except for reserved memory (GAMS option “*m.workspace=2*1024*”), relative gap between primal and dual solution (GAMS option “*optcr=0.0001*”) and, for BARON only, local search before branching (BARON option “*NumLoc 0*”). Initial solutions are global optima as calculated using the respective solver combination.

2.3.1 BARON/CPLEX/CONOPT

Figure 2.3 shows the distribution of 800 samples for solving “gsg_0001” with random permutations of the equation order using BARON with CPLEX and CONOPT as subsolvers. Based on the given samples, a normal distribution is unlikely. The interval including 95% of the true distribution with 99% confidence according to Equation (2.1) stretches from approximately 60 s to 850 s, over one order of magnitude.

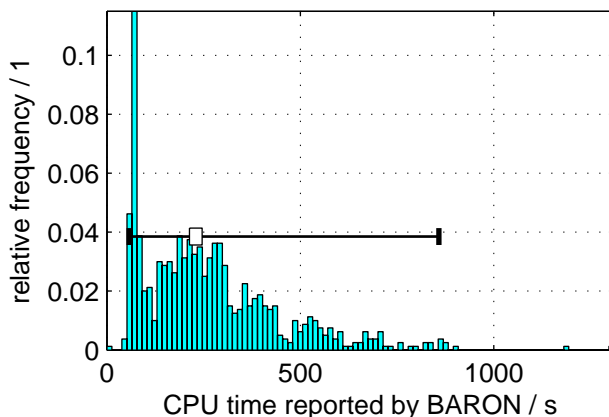


Figure 2.3: Distribution of CPU time reported by BARON for solving 800 instances of “gsg_0001” with random permutations of equation order and 99% confidence intervals for the median (white box), $P_{0.02275}$ and $P_{0.97725}$ (whiskers) of the true CPU time distribution.

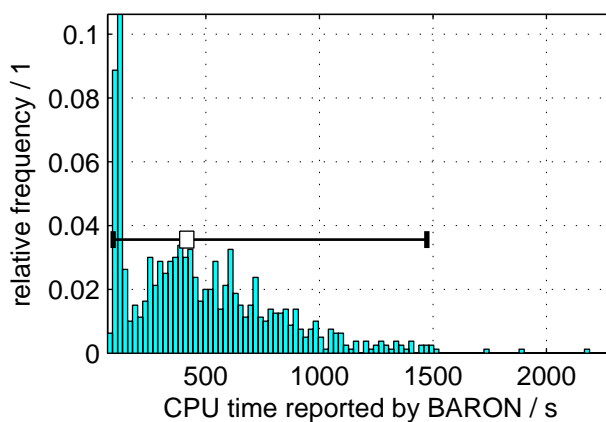
2.3.2 Other Solvers

Figure 2.4a shows the distribution of 800 samples for solving “gsg_0001” with random permutations of the equation order reported by BARON using CLP instead of CPLEX. SCIP 3.2 with CPLEX 12.6.3.0 and IPOPT 3.12 is used for Figure 2.4b. The results show that large variations of the CPU time for random permutations of the equation order also occur for those solver combinations.

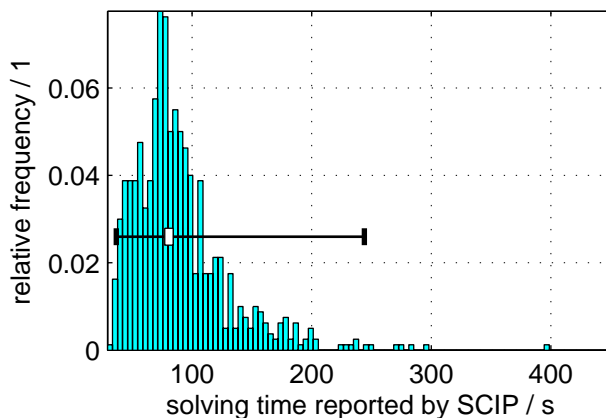
2.4 Conclusion

The computational effort for an optimization task strongly depends on parameters like equation order and order of variables. Those parameters can not be

kept constant when the computational performance of two different formulations of the same optimization problem is compared, e. g. for adding redundant equations or eliminating intermediate variables. Therefore, comparing single measurements gives only weak evidence on whether some problem formulation requires less computational effort or not. More reliable results are achieved by statistically evaluating influences on the computational performance, which is applied in subsequent chapters of this thesis. All tested solver combinations show the same behavior, thus only the combination of BARON with CPLEX



(a) BARON using CLP and CONOPT



(b) SCIP using CPLEX and IPOPT

Figure 2.4: Solver comparison. Distribution of CPU time and “solving time” for solving 800 instances of “gsg_0001” with random permutations of equation order and 99 % confidence intervals for the median ($P_{0.02275}$ and $P_{0.97725}$ (whiskers) of the true distribution.

and CONOPT will be applied throughout the rest of this work.

Chapter 3

Analysis of Multistage Separation Networks

3.1 Introduction

Process synthesis and design aims at reducing operational and investment costs of industrial processes. Product separation and purification is an essential step in chemical processes and responsible for a significant part of the overall costs. Multistage separation is applied if a single separation step does not fulfill yield or purity requirements. Standard approaches to multistage separation focus on countercurrent configurations. However, due to the restricted process topology, this process configuration may be suboptimal. Relaxing restrictions on process topology also allows new and possibly more efficient process configurations. Global deterministic optimization is used to identify novel process configurations that are guaranteed to achieve the best objective values and to analyze the behavior of globally optimal solutions of the model with regard to parameter values. Based on this insight, promising candidates or design strategies are provided for higher steps of hierarchical design frameworks with more detailed process models.

This chapter is structured as follows. First, melt crystallization for a binary mixture is studied as a benchmark process for multistage separation networks. The mathematical description of this process is chosen sufficiently simple to enable detailed parameter studies of globally optimal multistage separation designs. The results obtained for melt crystallization are then extended to multistage solution crystallization and multistage filtration, demonstrating the generalization of results to different separation technologies.

3.2 Melt Crystallization

Crystallization processes are based on generating supersaturation in a liquid phase as a driving force for crystal growth. Resulting crystals generally have a composition different from the original melt, enabling the separation of the components of a mixture. The solubility of components in a mixture and therefore supersaturation depends on factors such as composition, temperature and pressure. The process class of melt crystallization refers to crystallization in liquid mixtures without a dedicated solvent by means of a temperature decrease. Melt crystallization is used for product purification and separation

in chemical processes, with solid layer melt crystallization being a subclass of crystallization in which melt flows over cooled surfaces to generate crystal layers. This process often requires large equipment sizes for corresponding surface areas. However, product separation can be implemented just by draining remaining melt from the crystal layer before melting and collecting it separately. An overview on different processes using solid layer melt crystallization is given in [Ulrich et al., 1996].

3.2.1 Process Model

Single Units

The phase behavior of the mixture considered in the following model, see Figure 3.1, is that of a binary eutectic system. The crystal layer is assumed to incorporate impurities from the liquid melt, preventing the process from generating a pure crystal product in a single step. During solid layer melt crystallization, the melt is cooled down to the crystallization temperature (Figure 3.1: 1) at a surface and a solid layer starts to form. The solid layer has a different composition than the melt, resulting in selective removal of one of the components from the melt. As the crystal layer grows, the composition and therefore also the crystallization temperature of the melt successively change (Figure 3.1: 2). Due to increasing impurity concentration in the melt, newly formed crystal product has more impurity inclusions than previously formed layers (Figure 3.1: 3), resulting in a non-uniform composition of the overall crystal layer.

The model applied here is based on the distribution of impurities between crystals and remaining melt for constant process conditions, e. g. for very small amounts of crystal product, using the differential distribution coefficient k_{diff} [Lewis et al., 2015]. It is defined as

$$k_{\text{diff}} = \frac{w_{\text{impurity}}}{x_{\text{impurity}}}, \quad (3.1)$$

with the molar fraction of impurity in the crystal product w_{impurity} and in the melt x_{impurity} . The differential distribution coefficient k_{diff} needs to be less than one for a reduction of impurity in the crystal product compared to the melt.

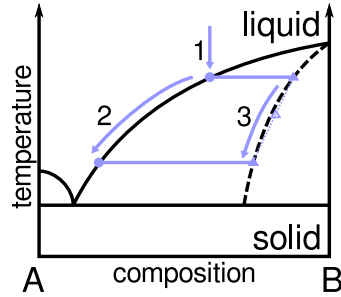


Figure 3.1: Exemplary phase diagram for an eutectic system with progression during crystallization due to cooling. The dashed line marks impurity inclusions in the solid phase instead of ideally pure component B.

Note that the distribution coefficient can also be defined using weight fractions, as in [Wellinghoff and Wintermantel, 1991].

Due to the non-uniform crystal layer composition, the overall distribution of impurities deviates from the differential distribution coefficient and is given by the integral distribution coefficient

$$k_{\text{int}} = \frac{w_{\text{impurity}}^{\text{mean}}}{x_{\text{impurity}}^{\text{feed}}}, \quad (3.2)$$

with the average molar fraction of impurity in the overall crystal product $w_{\text{impurity}}^{\text{mean}}$ and the mass fraction of impurity in the melt before crystallization $x_{\text{impurity}}^{\text{feed}}$. The integral distribution coefficient describes the separation efficiency of solid layer melt crystallization without explicitly calculating the transient behavior of the process.

In this thesis, the impurity distribution is described by a constant differential distribution coefficient as in [Wellinghoff and Wintermantel, 1991] and [Micovic et al., 2013]. For $k_{\text{diff}} = \text{const.}$, the integral distribution coefficient depends solely on the yield Y , i. e. the ratio of crystal product amount to amount of melt before crystallization, and is calculated as follows, see Appendix A.

$$k_{\text{int}} = \frac{1 - (1 - Y)^{k_{\text{diff}}}}{Y} \quad (3.3)$$

For a yield Y approaching zero, the integral distribution coefficient k_{int} approaches the differential distribution coefficient k_{diff} . The integral distribution coefficient increases with yield, up to $k_{\text{int}}(Y=1) = 1$. This means separation is most efficient for low yields and there is no separation if the entire feed is crystallized. Note that the integral distribution coefficient does not comprise any

temperature dependence and therefore restrictions due to the eutectic point are implemented separately as outlined further below.

The model equations describing the separation according to Wellinghoff and Wintermantel [1991] for each single stage $n = 1, \dots, n^{\text{Cr}}$ as in Figure 3.2 read

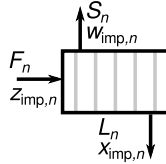


Figure 3.2: Single melt crystallization unit with feed molar flow F_n , crystal product molar flow S_n and liquid remainder molar flow L_n with corresponding impurity molar fractions.

$$\begin{aligned} S_n &= Y_n F_n, & w_{\text{imp},n} &= k_{\text{int},n} z_{\text{imp},n}, \\ L_n &= F_n - S_n, & x_{\text{imp},n} L_n &= z_{\text{imp},n} F_n - w_{\text{imp},n} S_n, \\ k_{\text{int},n} Y_n &= 1 - (1 - Y_n)^{k_{\text{diff}}} , \end{aligned} \quad (3.4)$$

with crystal yield $Y_n \in [0, 1]$ and integral distribution coefficient $k_{\text{int},n} \in [0, 1]$. The molar fraction of impurity in the feed is denoted by $z_{\text{imp},n}$, in the crystal product by $w_{\text{imp},n}$ and in the liquid remainder by $x_{\text{imp},n}$. Molar flows are denoted as F_n for unit feeds, S_n for crystal product and L_n for liquid remainder. Physical restrictions due to the eutectic point and technical restrictions due to a minimum cooling temperature pose additional model constraints. The minimum cooling temperature is equivalent to a maximum molar fraction of impurity based on the solid-liquid equilibrium. The more restrictive of both, eutectic composition and temperature-based maximum impurity concentration, gives an upper bound $x_{\text{imp}}^{\text{max}}$ for molar fractions of impurity in the melt $x_{\text{imp},n}$ on each single stage $n = 1, \dots, n^{\text{Cr}}$.

$$x_{\text{imp}}^{\text{max}} \geq x_{\text{imp},n}, \quad n = 1, \dots, n^{\text{Cr}} \quad (3.5)$$

The yield Y is further restricted for non-zero feed impurities. Rewriting Equation (3.4) gives

$$x_{\text{imp}} = (1 - Y)^{k_{\text{diff}} - 1} z_{\text{imp}}. \quad (3.6)$$

If the molar fraction of impurity in the liquid remainder x_{imp} is bounded from above, e.g. by the eutectic composition, the yield Y is also bounded from

above by a value less than one. However, $Y = 1$, i.e. total crystallization, is feasible for this model since $L=0$ in that case and therefore x_{imp} is not defined. The crystallization model comprises Equation (3.4). Equation (3.5) is implemented as bounds to the respective variables.

Network of Crystallizer Units

A crystallizer network with stages $n = 1, \dots, n^{\text{Cr}}$ numbered downwards as in Figure 3.3 is considered. Recall that each stage n separates a molar feed flow F_n into crystal product S_n and liquid remainder L_n with molar fractions of the impurity denoted as $z_{\text{imp},n}$, $w_{\text{imp},n}$ and $x_{\text{imp},n}$, respectively. The feed of each stage F_n is the sum of all crystal product flows S and liquid remainder flows L connected to that stage and, if applicable for that stage, the crystallizer feed flow F^{InCr} . The distribution of the feed flow and connections between stages are implemented using binary variables $\beta_n^{\text{InCr}} \in \{0, 1\}$, $\beta_{l,n}^{\text{S}} \in \{0, 1\}$ and $\beta_{l,n}^{\text{L}} \in \{0, 1\}$, $n = 1, \dots, n^{\text{Cr}}$, $l = 1, \dots, n^{\text{Cr}}$. The variables β_n^{InCr} , $\beta_{l,n}^{\text{S}}$ and $\beta_{l,n}^{\text{L}}$ attain a value of one if and only if the feed enters at stage n , the crystal product output of stage l is fed to stage n and the liquid remainder output of stage l is fed to stage n , respectively. The mass balance equations for the feed of each stage $n = 1, \dots, n^{\text{Cr}}$ then read

$$F_n = F^{\text{InCr}} \beta_n^{\text{InCr}} + \sum_{l=1}^{n^{\text{Cr}}} S_l \beta_{l,n}^{\text{S}} + \sum_{l=1}^{n^{\text{Cr}}} L_l \beta_{l,n}^{\text{L}}, \quad (3.7)$$

$$z_{\text{imp},n} F_n = z_{\text{imp}}^{\text{InCr}} F^{\text{InCr}} \beta_n^{\text{InCr}} + \sum_{l=1}^{n^{\text{Cr}}} w_{\text{imp},l} S_l \beta_{l,n}^{\text{S}} + \sum_{l=1}^{n^{\text{Cr}}} x_{\text{imp},l} L_l \beta_{l,n}^{\text{L}}. \quad (3.8)$$

It is ensured that the feed enters exactly one stage by

$$\sum_{n=1}^{n^{\text{Cr}}} \beta_n^{\text{InCr}} = 1. \quad (3.9)$$

The output flow of each stage is connected to exactly one stage input or one crystallizer product output by

$$\sum_{n=1}^{n^{\text{Cr}}} \beta_{l,n}^{\text{S}} + \beta_l^{\text{S,Out1Cr}} = 1, \quad l = 1, \dots, n^{\text{Cr}}, \quad (3.10)$$

$$\sum_{n=1}^{n^{\text{Cr}}} \beta_{l,n}^{\text{L}} + \beta_l^{\text{L,Out2Cr}} = 1, \quad l = 1, \dots, n^{\text{Cr}}, \quad (3.11)$$

with $\beta_l^{S, \text{Out}1_{\text{Cr}}} \in \{0, 1\}$ attaining a value of 1 if and only if the crystal product output of stage l is connected to output $\text{Out}1_{\text{Cr}}$ and with $\beta_l^{L, \text{Out}2_{\text{Cr}}} \in \{0, 1\}$ attaining a value of 1 if and only if the liquid remainder output of stage l is connected to output $\text{Out}2_{\text{Cr}}$. The product flows are then calculated as

$$F^{\text{Out}1_{\text{Cr}}} = \sum_{n=1}^{n^{\text{Cr}}} \beta_n^{S, \text{Out}1_{\text{Cr}}} S_n, \quad (3.12)$$

$$F^{\text{Out}2_{\text{Cr}}} = \sum_{n=1}^{n^{\text{Cr}}} \beta_n^{L, \text{Out}2_{\text{Cr}}} L_n,$$

$$z_{\text{imp}}^{\text{Out}1_{\text{Cr}}} F^{\text{Out}1_{\text{Cr}}} = \sum_{n=1}^{n^{\text{Cr}}} \beta_n^{S, \text{Out}1_{\text{Cr}}} w_{\text{imp}, n} S_n, \quad (3.13)$$

$$z_{\text{imp}}^{\text{Out}2_{\text{Cr}}} F^{\text{Out}2_{\text{Cr}}} = \sum_{n=1}^{n^{\text{Cr}}} \beta_n^{L, \text{Out}2_{\text{Cr}}} x_{\text{imp}, n} L_n.$$

It is required that each stage has at least one input.

$$\sum_{l=1}^{n^{\text{Cr}}} (\beta_{l,n}^S + \beta_{l,n}^L) + \beta_n^{\text{InCr}} \geq 1, \quad n = 1, \dots, n^{\text{Cr}} \quad (3.14)$$

By definition, the stages are ordered in terms of purity of the stage feed.

$$z_{\text{imp}, n} \leq z_{\text{imp}, n+1}, \quad n = 1, \dots, n^{\text{Cr}} - 1 \quad (3.15)$$

Recall that a process for separating mixture with two components is considered here. Therefore, the crystal output flow of each stage has a smaller impurity concentration compared to the respective feed flow and the liquid remainder an increased impurity concentration. Since remixing of already purified flows reduces efficiency, possible connections for crystal outputs are limited to stages closer to the respective overall product outlet by additional constraints.

$$\beta_{l,n}^S = 0 \quad \text{for all } 1 \leq l \leq n, \quad n = 1, \dots, n^{\text{Cr}} \quad (3.16)$$

$$\beta_{l,n}^L = 0 \quad \text{for all } n \leq l \leq n^{\text{Cr}}, \quad n = 1, \dots, n^{\text{Cr}} \quad (3.17)$$

All potential connections within the crystallizer network used in this work are illustrated in Figure 3.3 (a) for a fixed number of stages $n^{\text{Cr}} = 3$. The countercurrent cascade depicted in Figure 3.3 (b) will serve as the benchmark for any other configuration within this superstructure.

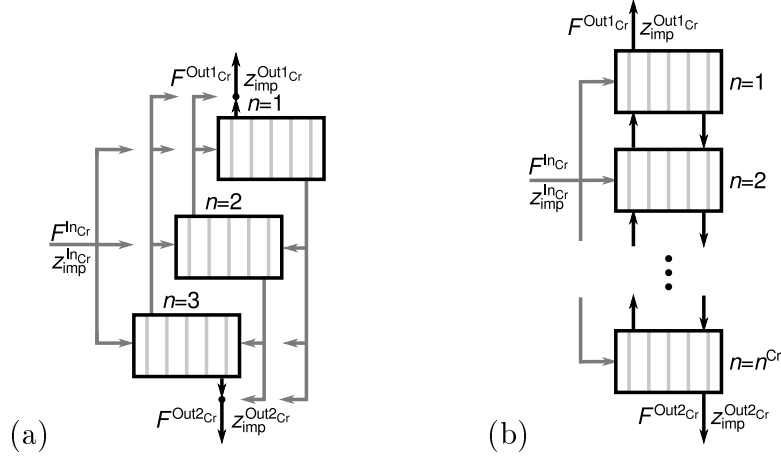


Figure 3.3: (a) Crystallizer network consisting of $n^{Cr} = 3$ stages with arbitrary configurations. (b) Countercurrent crystallizer cascade with n^{Cr} stages and arbitrary feed stage ($\beta_{l,l-1}^S = 1, l = 2, \dots, n^{Cr}, \beta_{l,l+1}^L = 1, l = 1, \dots, n^{Cr} - 1, \beta_1^{S,Out1Cr} = 1, \beta_{n^{Cr}}^{L,Out2Cr} = 1$). [Reprinted from Kunde et al., 2016, with permission from Elsevier]

Material balances for the overall separation network are included implicitly in all material balances for the single units and the connections between units. The overall material balances are added to the model as redundant equations to tighten the model description.

$$F^{InCr} = F^{Out1Cr} + F^{Out2Cr} \quad (3.18)$$

$$z_{imp}^{InCr} F^{InCr} = z_{imp}^{Out1Cr} F^{Out1Cr} + z_{imp}^{Out2Cr} F^{Out2Cr} \quad (3.19)$$

The separation network model comprises Equations (3.8)-(3.15) and (3.18)-(3.19). Equations (3.16)-(3.17) are implemented as bounds to the respective variables.

Objective Function

Process costs are determined according to correlations from [Towler and Sinnott, 2008]. The cost function accounts for annualized installed investment costs of the crystallizer vessel as a heat exchanger, a storage tank for each crystallization stage with the same capacity as the crystallizer and for the energy costs of the process. The capacity of the crystallizer is calculated as in [Franke et al., 2008] and the required cooling according to [Wellinghoff and Wintermantel, 1991, Franke et al., 2008]. The resulting total annualized cost

function is written in a condensed form as

$$J_{\text{TAC}} = (a_1 \sum_{n=1}^{n^{\text{Cr}}} S_n \text{ s mol}^{-1} + a_2 + n^{\text{Cr}}(a_3(\sum_{n=1}^{n^{\text{Cr}}} S_n \text{ s mol}^{-1})^{a_4} + a_5)) \text{ \$ a}^{-1}. \quad (3.20)$$

Note that economic cost functions in the conceptual phase of a hierarchical design framework describe the qualitative behavior of process costs with respect to model variables and give an estimate of the order of magnitude of the actual costs. More detailed process models in higher steps of such a framework allow for more detailed cost estimations.

The cost function J_{TAC} is monotonically increasing with $\sum_{n=1}^{n^{\text{Cr}}} S_n$. Therefore, for fixed values of stages n^{Cr} and feed flow F^{InCr} , economic cost is minimized by minimizing crystallization effort J_{S} [Mersmann, 2001].

$$J_{\text{S}} = \frac{\sum_{n=1}^{n^{\text{Cr}}} S_n}{F^{\text{InCr}}}. \quad (3.21)$$

The optimization problem is solved first with respect to the crystallization effort J_{S} for each total number of stages $n^{\text{Cr}} = 1, \dots, n^{\text{Cr,max}}$. Then the total number of stages with the lowest total annualized cost J_{TAC} is selected as a globally optimal solution for the original cost function.

3.2.2 Reformulation

Branch-and-bound algorithms rely on calculating globally valid bounds to the optimal objective value in each region of the search space. Such strong statements to optimality of solutions compared to local optimization coincide with increased computational effort. The computational effort for branch-and-bound algorithms scales with the number of variables and nonlinearities as well as the types of nonlinearities. Models written for specific purposes other than global optimization usually have different requirements, e.g. variables are chosen for readability or explicit equations are preferred for simulation tools. Model formulations efficient for simulation may be inefficient for global optimization, which offers potential for model reformulations. A reformulation of the crystallization model with simpler and less nonlinear terms than in the original version is supplied in this section.

The main idea for this reformulation is using molar flows of impurities defined by

$$S_{\text{imp},n} = w_{\text{imp},n} S_n, \quad L_{\text{imp},n} = x_{\text{imp},n} L_n, \quad F_{\text{imp},n} = z_{\text{imp},n} F_n, \quad (3.22)$$

instead of molar fractions.

Single Unit

Using Equation (3.22), the distribution of impurities is given by

$$S_{\text{imp},n} = k_{\text{int},n} Y_n F_{\text{imp},n} = (1 - (1 - Y_n)^{k_{\text{diff}}}) F_{\text{imp},n}. \quad (3.23)$$

A new variable $\tilde{Y}_n \in [0, 1]$ is introduced as

$$\tilde{Y}_n = 1 - Y_n \quad (3.24)$$

to write the set of equations for the crystallizer that replaces Equation (3.4). For each stage $n = 1, \dots, n^{\text{Cr}}$, we have

$$\begin{aligned} L_{\text{imp},n} &= \tilde{Y}_n^{k_{\text{diff}}} F_{\text{imp},n}, & S_{\text{imp},n} &= F_{\text{imp},n} - L_{\text{imp},n}, \\ L_n &= \tilde{Y}_n F_n, & S_n &= F_n - L_n. \end{aligned} \quad (3.25)$$

Note that these definitions correspond to a yield for liquid remainder \tilde{Y} and the distribution of impurities to the liquid remainder. So for a yield $\tilde{Y} = 1$ we have no crystal product and all impurity stays in the liquid. Corresponding to the crystal yield in the original model formulation, the yield for liquid remainder is restricted by upper bounds to the molar fraction of impurity in the liquid. However, the case of $\tilde{Y} = 0$, i. e. total crystallization with no liquid remainder, is feasible for this model although it is not reasonable for a real process.

Equation (3.5) is rewritten in terms of molar flows as

$$x_{\text{imp}}^{\text{max}} L_n \geq L_{\text{imp},n}, \quad n = 1, \dots, n^{\text{Cr}}. \quad (3.26)$$

Network of Crystallizer Units

Molar fractions in Equation (3.8) are substituted using Equation (3.22) to obtain

$$F_{\text{imp},n} = F_{\text{imp}}^{\text{InCr}} \beta_n^{\text{InCr}} + \sum_{l=1}^{n^{\text{Cr}}} S_{\text{imp},l} \beta_{l,n}^{\text{S}} + \sum_{l=1}^{n^{\text{Cr}}} L_{\text{imp},l} \beta_{l,n}^{\text{L}} \quad (3.27)$$

for each $n = 1, \dots, n^{\text{Cr}}$, and in Equation (3.13) to obtain

$$F_{\text{imp}}^{\text{Out1Cr}} = \sum_{n=1}^{n^{\text{Cr}}} \beta_n^{\text{S,Out1Cr}} S_{\text{imp},n}, \quad (3.28)$$

$$F_{\text{imp}}^{\text{Out2Cr}} = \sum_{n=1}^{n^{\text{Cr}}} \beta_n^{\text{L,Out2Cr}} L_{\text{imp},n}. \quad (3.29)$$

Molar fractions are still used for the inlet composition $z_{\text{imp}}^{\text{InCr}}$ and the product specifications for $z_{\text{imp}}^{\text{Out1Cr}}$ and $z_{\text{imp}}^{\text{Out2Cr}}$. Quantities at the inlet of the separation network are constant parameters. The impurity molar flow at the inlet is calculated by

$$F_{\text{imp}}^{\text{InCr}} = z_{\text{imp}}^{\text{InCr}} F^{\text{InCr}}. \quad (3.30)$$

Additional equations for the outlet compositions are introduced as

$$F_{\text{imp}}^{\text{Out1Cr}} = z_{\text{imp}}^{\text{Out1Cr}} F^{\text{Out1Cr}}, \quad (3.31)$$

$$F_{\text{imp}}^{\text{Out2Cr}} = z_{\text{imp}}^{\text{Out2Cr}} F^{\text{Out2Cr}}. \quad (3.32)$$

Equation (3.15) is rewritten in terms of molar flows as

$$F_{\text{imp},n} F_{n+1} \leq F_{\text{imp},n+1} F_n, \quad n = 1, \dots, n^{\text{Cr}} - 1. \quad (3.33)$$

3.2.3 Redundant Configurations

The melt crystallization model used in this work allows that different network configurations have the same optimal objective value. This includes redundant configurations not meaningful for process design as well as sets of meaningful configurations that can not be discerned using the given level of modeling detail. Some of the most simple cases of redundancies are excluded from the search space by additional constraints, e. g. Equation (3.14) prevents isolated stages without any incoming connections. For larger separation networks, redundant structures become more complex, e. g. isolated groups of stages without connections to the feed or the product outlets of the separation network. Complex constraints to address such structures increase the model size and thus may increase the computational effort for global optimization. In this work, instead of removing all redundant configurations from the search space, possible sources of redundancy are discussed and according solutions

are removed from optimization results.

One source of redundancy considered are inactive stages, i. e. stages with zero crystal yield. Adding inactive stages to a configuration does not change flows between the original stages. Therefore, the crystallization effort is the same as without additional inactive stages, creating redundant globally optimal solutions when using the crystallization effort as objective function. This type of redundancy is treated by solving the problem for each possible number of stages and selecting the globally optimal solution with the lowest number of stages.

Economic cost of the process according to Equation (3.20) increases with increasing stage number. Therefore, adding inactive stages does not introduce redundant globally optimal solutions when minimizing economic cost.

A second source of redundant solutions are groups of stages isolated from the overall feed or overall product outlets, e. g. Figure 3.4. If isolated stages have nonzero crystal product flows, according solutions are suboptimal due to increased economic cost as well as crystallization effort and therefore are not included in the set of globally optimal solutions. If isolated stages have zero crystal product flow they are treated the same as inactive stages.

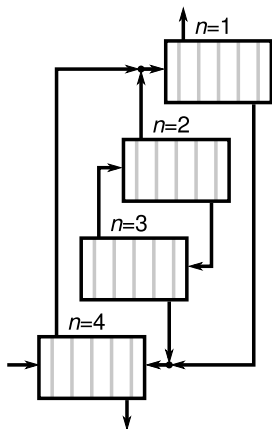


Figure 3.4: Example for redundant configurations. Group of stages $n = \{2, 3\}$ does not have an overall feed.

Another source of redundancy is that a single crystallizer stage can be replaced by two stages with the same overall product flows and crystallization effort as shown in Figure 3.5. Both configurations are equivalent with regard

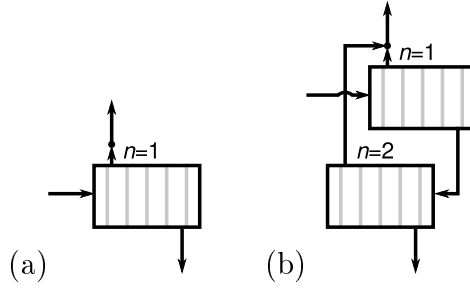


Figure 3.5: Equivalent (sub-)configurations when optimizing crystallization effort: (a) Single crystallizer stage. (b) Two-stage crystallizer cascade.

to crystallization effort and product flows for

$$\tilde{Y}_1 \tilde{Y}_2 = \tilde{Y}_{\text{single}} \quad (3.34)$$

with the liquid yield of the single crystallizer $\tilde{Y}_{\text{single}}$ and the liquid yields of the two crystallizer stages $\tilde{Y}_{1,2}$. This is verified for equal overall feed flows $F_1 = F_{\text{single}}$ as follows.

The liquid product flows L_2 and L_{single} are equal according to

$$L_2 = \tilde{Y}_2 F_2 = \tilde{Y}_2 L_1 = \tilde{Y}_1 \tilde{Y}_2 F_1 = \tilde{Y}_{\text{single}} F_{\text{single}} = L_{\text{single}} \quad (3.35)$$

Correspondingly, equality is shown for the liquid impurity flows $L_{\text{imp},2}$ and $L_{\text{imp},\text{single}}$.

$$L_{\text{imp},2} = \tilde{Y}_2^{k_{\text{diff}}} F_{\text{imp},2} = \tilde{Y}_1^{k_{\text{diff}}} \tilde{Y}_2^{k_{\text{diff}}} F_{\text{imp},1} = \tilde{Y}_{\text{single}}^{k_{\text{diff}}} F_{\text{imp},\text{single}} = L_{\text{imp},\text{single}} \quad (3.36)$$

The crystal product flows then have to be equal due to mass conservation. Finally, crystallization efforts $S_1 + S_2$ and S_{single} are equal according to

$$S_1 + S_2 = F_1 - L_2 = (1 - \tilde{Y}_1 \tilde{Y}_2) F_1 = (1 - \tilde{Y}_{\text{single}}) F_{\text{single}} = S_{\text{single}}. \quad (3.37)$$

This type of redundancy is also treated by identifying the globally optimal solution with the lowest number of stages and does not occur when minimizing economic cost.

The redundancies discussed above only create multiple globally optimal solutions if the crystallization effort J_S is used as the objective function, since the number of stages increases for those redundant configurations. In contrast, multiple globally optimal solutions with regard to economic cost J_{TAC} require that the crystallization effort as well as the number of stages are equal. Multiple solutions of this type are discussed together with the results of the following computational studies.

3.2.4 Computational Studies

This section deals with computational results based on the model formulations for multistage melt crystallization given above. In the first part, the computational effort for solving the original model formulation and the reformulated model is evaluated. The more efficient of both model formulations is used in the second part for a comprehensive analysis of model behavior based on parameter studies of globally optimal solutions.

Computational Effort

The CPU time required using the original formulation and the postulated reformulation for fixed n^{Cr} is evaluated by minimizing the crystallization effort J_S for 800 model instances with random permutations of equation order, binary variable order and positive variable order, similar to Chapter 2. Parameters used for this test are given in Table 3.1. Solver options are kept at default values except for reserved memory (GAMS option “*m.workspace=2*1024*”), relative gap between primal and dual solution (GAMS option “*optcr=0.0001*”) and local search before branching (BARON option “*NumLoc 0*”). A globally optimal solution for each formulation is calculated beforehand with the same solver and options and provided as an initial point. Doing this reduces the optimization task to calculating lower bounds to prove global optimality of the provided solution. Finding good local solutions as upper bounds to the objective function is thereby removed as an influence on the computational effort.

Table 3.1: Parameter and domain specifications for comparison of computational effort between original model formulation and reformulation.

parameter	value	variable	domain
k_{diff}	0.3	$z_{\text{imp}}^{\text{Out1Cr}}$	[0, 0.01]
$z_{\text{imp}}^{\text{InCr}}$	0.7	$z_{\text{imp}}^{\text{Out2Cr}}$	[0.89, 1]
F^{InCr}	1 mol s ⁻¹	z, Y, k	[0, 1]
$x_{\text{imp}}^{\text{max}}$	0.9	S, L, F	[0 mol s ⁻¹ , 20 mol s ⁻¹]
n^{Cr}	4	β	{0, 1}

As depicted in Figure 3.6, the median CPU time required for solving the

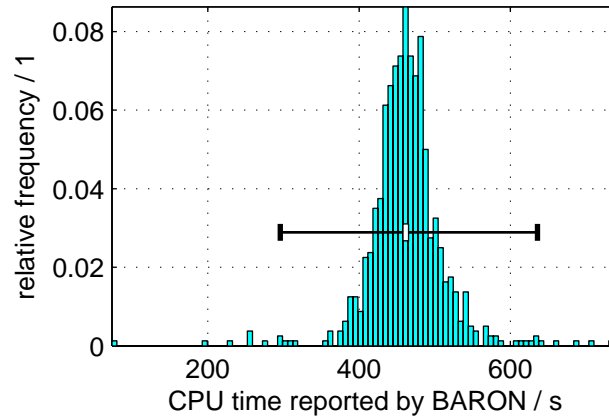
reference case is reduced by one order of magnitude by using the reformulation. Thus, the reformulated model is used in the following parameter studies.

Parameter Studies

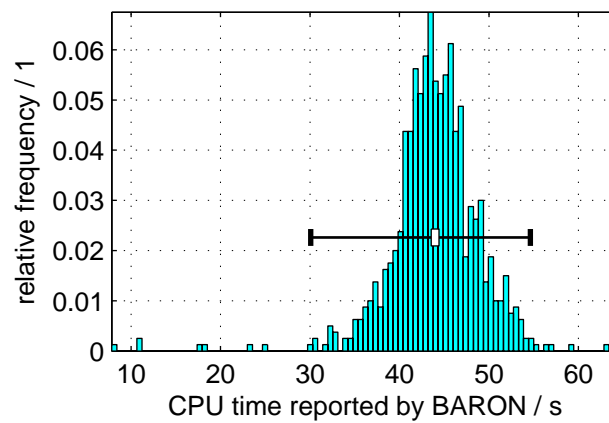
Model parameters affecting the optimal configuration of a crystallizer network are the differential distribution coefficient k_{diff} , the feed concentration of impurity z^{InCr} , the product specifications z^{Out1Cr} , z^{Out2Cr} and, if applicable, the parameters of an economic cost function. The eutectic composition is implicitly included in this set of parameters by limiting feasible values for the feed composition and product specifications. A comprehensive characterization of optimal solutions for the considered melt crystallization model is given in this section using parameter studies for the differential distribution coefficient and the feed composition for both low and high product yield and purity. For each case, the optimal design of countercurrent cascades is discussed as a reference for potentially better alternative designs. Then, alternative designs with better objective values than the countercurrent design are analyzed. Based on the results, simplified criteria for optimal design of multistage melt crystallization processes are given.

In Case 1 and Case 2, optimal configurations with regard to economic cost are presented for mixtures of isomers 2-methylundecanal and n-dodecanal. Physical data of this mixture and some analysis of modeling approaches and model behavior based on local optimization is available in [Beierling and Ruether, 2012, Micovic et al., 2013, Beierling et al., 2014]. Weight fractions used in these publications are equivalent to molar fractions used here since mixtures of isomers are considered. Economic cost parameters comprise information about specific physical parameter values of a mixture and equipment restrictions. Here, it is assumed that the same set of parameters, given in Table 3.2, can be applied to the whole range of feed and product specifications as well as separation efficiencies.

Determination of accurate economic cost is highly dependent on many, probably uncertain, problem-specific parameters. For instance, the ratio of operating cost to investment cost in Case 1 and Case 2 depends on energy prices, which are not related to any process variables but depend on the country a plant is operated in. Therefore, more general performance indicators are needed



(a) Original model formulation.



(b) Reformulated model.

Figure 3.6: Distribution of CPU time reported by BARON for solving 800 instances of the crystallizer model with random permutations of equation and variable order and 99 % confidence intervals for the median (white box), $P_{0.02275}$ and $P_{0.97725}$ (whiskers) of the true CPU time distribution.

Table 3.2: Parameter specifications for economic cost function.

parameter	value	parameter	value
a_1	86849	a_4	0.7
a_2	5215	a_5	2123.2
a_3	1605.7		

to compare optimization results for different processes. The total amount of crystal product required to separate a given feed according to yield and purity specification is a suitable measure of the required processing effort for this task. The crystallization effort influences both operational cost and equipment size, and it has comparable counterparts in other separation technologies. Thus, in Case 3, multistage crystallizer networks that are optimal with regard to the crystallization effort are analyzed.

Case 1: Low Product Yield and Purity The optimal multistage crystallizer configuration is determined by minimizing crystallization effort J_S for each number of stages $n^{\text{Cr}} = 1, 2, 3, 4$ and selecting the number of stages with lowest economical cost J_{TAC} , see Section 3.2.1. This is repeated for each considered pair of differential distribution coefficient and feed composition. Parameter specifications and domain specifications for variables are given in Table 3.3. The configuration with the lowest objective value is chosen from each set of optimal configurations with different numbers of stages and otherwise identical parameter values. If configurations with equal objective values are encountered, the configuration with the lowest number of stages is chosen. Objective values within 1 % of the value of the chosen configuration are considered equal to account for numerical imprecision. Solver options are kept at default values except for reserved memory (GAMS option “*m.workspace=2*1024*”) and relative gap between primal and dual solution (GAMS option “*optcr=0.0001*”). Feasible initial solutions are not provided.

In the following figures, each differently colored region represents a different globally optimal configuration of a crystallizer cascade or some property value of such a configuration, e.g. feed stage or number of stages. Each white dot represents a set of parameters for which a global optimum is determined. The

Table 3.3: Case 1. Parameter and domain specifications for influence of parameters on globally optimal configuration.

parameter	value	variable	domain
k_{diff}	$\{0.01, 0.02, \dots, 0.5\}$	$z_{\text{imp}}^{\text{Out1Cr}}$	$[0, 0.05]$
$z_{\text{imp}}^{\text{InCr}}$	$\{0.06, 0.08, \dots, 0.84\}$	$z_{\text{imp}}^{\text{Out2Cr}}$	$[0.85, 1]$
F^{InCr}	1 mol s^{-1}	z, Y, k	$[0, 1]$
$x_{\text{imp}}^{\text{max}}$	0.9	S, L, F	$[0 \text{ mol s}^{-1}, 20 \text{ mol s}^{-1}]$
n^{Cr}	$\{1, 2, 3, 4\}$	β	$\{0, 1\}$

feed composition is normalized to the product specifications according to

$$z_{\text{norm}}^{\text{InCr}} = \frac{z_{\text{imp}}^{\text{InCr}} - \text{up}(z_{\text{imp}}^{\text{Out1Cr}})}{\text{lo}(z_{\text{imp}}^{\text{Out2Cr}}) - \text{up}(z_{\text{imp}}^{\text{Out1Cr}})}. \quad (3.38)$$

The molar fraction of impurity in the feed flow $z_{\text{imp}}^{\text{InCr}}$ is limited by the normalized feed impurity $z_{\text{norm}}^{\text{InCr}} \in [0, 1]$. Outside of that interval the feed already fulfills product specifications and crystallization is not necessary.

First, the optimal design of countercurrent crystallizer cascades is discussed. Values of binary variables are restricted according to Equations (3.39)-(3.42) to limit the search space to countercurrent cascades.

$$\beta_{l,l-1}^{\text{S}} = 1, \quad l = 2, \dots, n^{\text{Cr}}, \quad (3.39)$$

$$\beta_{l,l+1}^{\text{L}} = 1, \quad l = 1, \dots, n^{\text{Cr}} - 1, \quad (3.40)$$

$$\beta_1^{\text{S,Out1Cr}} = 1, \quad (3.41)$$

$$\beta_{n^{\text{Cr}}}^{\text{L,Out2Cr}} = 1 \quad (3.42)$$

The configuration of a countercurrent cascade is fully characterized by the number of stages and the feed stage position.

In Figure 3.7, parameter regions with different optimal numbers of stages are depicted. Sufficiently low product purity requirements (i. e. crystal product specification close to the feed composition) and high separation efficiency (i. e. small values for the differential distribution coefficient) allows separation of a mixture with one crystallization step. This case is represented by the lower left region of Figure 3.7. With increasing purity requirements and decreasing separation efficiency, more stages are necessary for a separation task. The optimal number of stages increases accordingly with increasing normalized

feed impurity and distribution coefficient, up to four stages in the upper right region of Figure 3.7. As an example, the optimal number of stages for a normalized feed impurity $z_{\text{norm}}^{\text{InCr}} = 0.4$ is described. One stage is optimal up to a distribution coefficient k_{diff} of approximately 0.1. Two stages are optimal for approximately $0.1 < k_{\text{diff}} < 0.3$, and three stages for $0.3 < k_{\text{diff}} < 0.4$.

The optimal position of the feed stage is treated in the same way as the

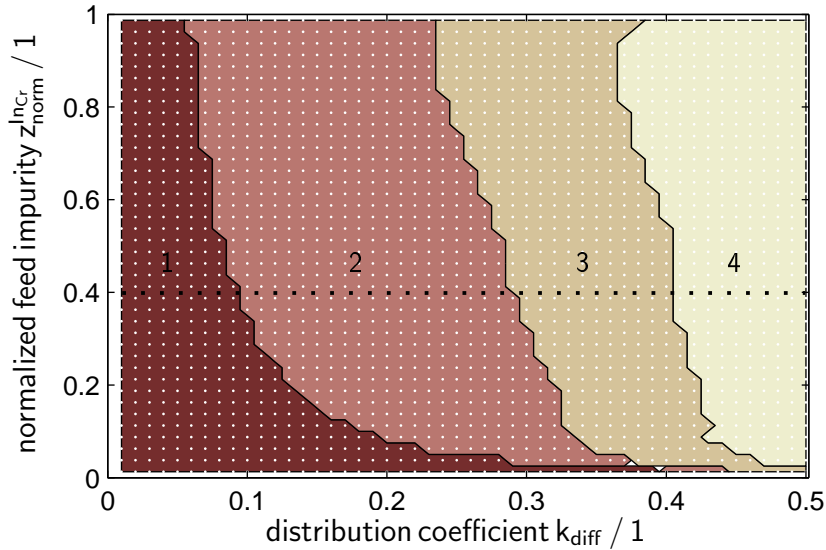


Figure 3.7: Case 1. Globally optimal number of stages of countercurrent crystallizer cascades. The dotted line shows the optimal number of stages for fixed feed concentrations and varied distribution coefficient values.

optimal number of stages. In Figure 3.8, regions with different optimal feed stages are depicted. The cost of multistage crystallization processes according to the model used in this work can be minimized by minimizing the sum of crystal product flows over all stages. If the feed enters the first stage counted from the top, i.e. the stage connected to the overall crystal product outlet, the amount of overall crystal product has to be crystallized at least once. If the feed enters the second stage of a countercurrent cascade the product amount has to be crystallized at least twice, and so on, potentially increasing process costs. However, larger differences of impurity concentration between feed and feed stage necessitate larger recycle flows, making higher feed stage numbers more favorable for higher purity requirements and lower separation efficiency. The resulting optimal feed position is on the first stage counted

from the top for low purity requirements and high separation efficiency. The optimal feed stage number increases with increasing normalized feed impurity and distribution coefficient, up to the fourth stage in the upper right region of Figure 3.8. For a fixed value of the normalized feed impurity $z_{\text{norm}}^{\text{InCr}} = 0.4$, the first stage is the optimal feed position for a distribution coefficient k_{diff} of up to approximately 0.16. The second stage is the optimal feed position for approximately $0.16 < k_{\text{diff}} < 0.31$ and the third stage for $0.31 < k_{\text{diff}} < 0.45$. Globally optimal configurations of a countercurrent crystallizer cascade,

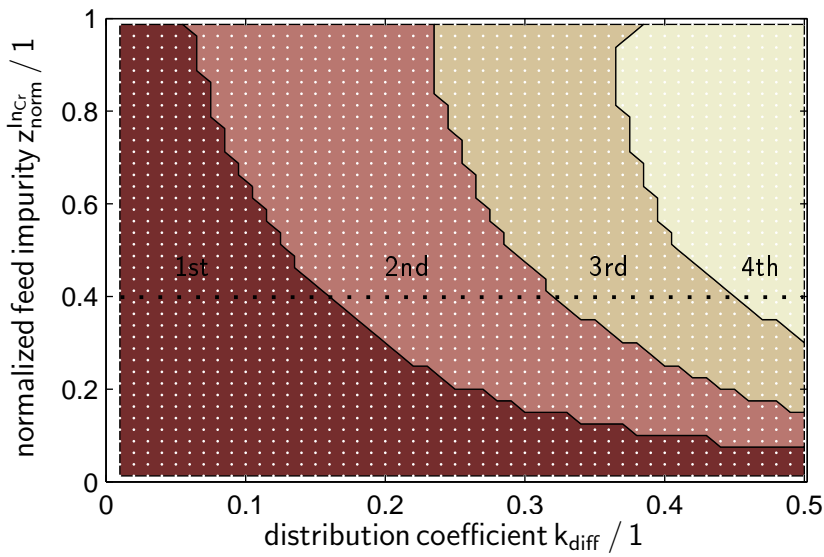


Figure 3.8: Case 1. Globally optimal feed stage position of countercurrent crystallizer cascade, counted from top. The dotted line shows the optimal feed position for fixed feed concentrations and varied distribution coefficient values.

characterized by number of stages and feed position, are depicted in Figure 3.9. It is a combination of Figure 3.7 and Figure 3.8, with each differently colored region representing a unique combination of number of stages and feed position. For example, for a distribution coefficient of $k_{\text{diff}} = 0.2$ a single crystallizer stage is optimal for a normalized feed impurity $z_{\text{norm}}^{\text{InCr}}$ below approximately 0.05, a crystallizer cascade with two stages and the feed on the first stage is optimal for approximately $0.1 < z_{\text{norm}}^{\text{InCr}} < 0.3$ and a crystallizer cascade with two stages and the feed on the second stage is optimal for $z_{\text{norm}}^{\text{InCr}}$ above approximately 0.35.

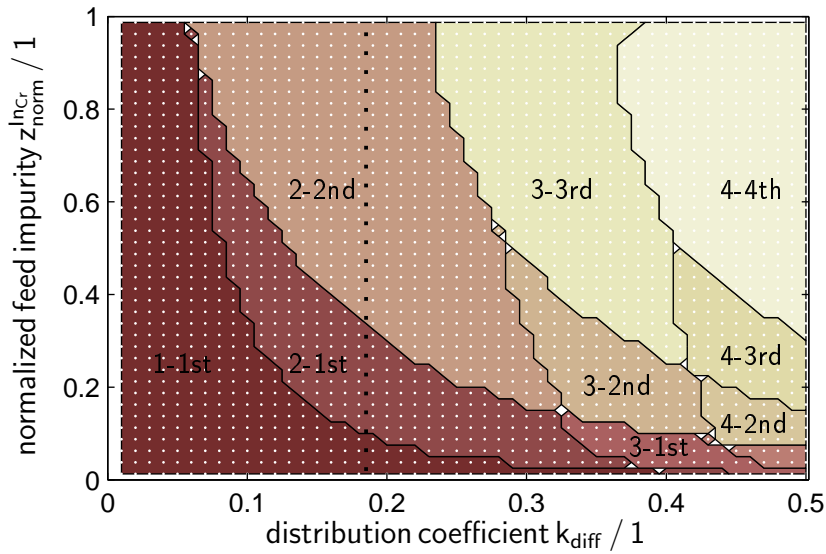
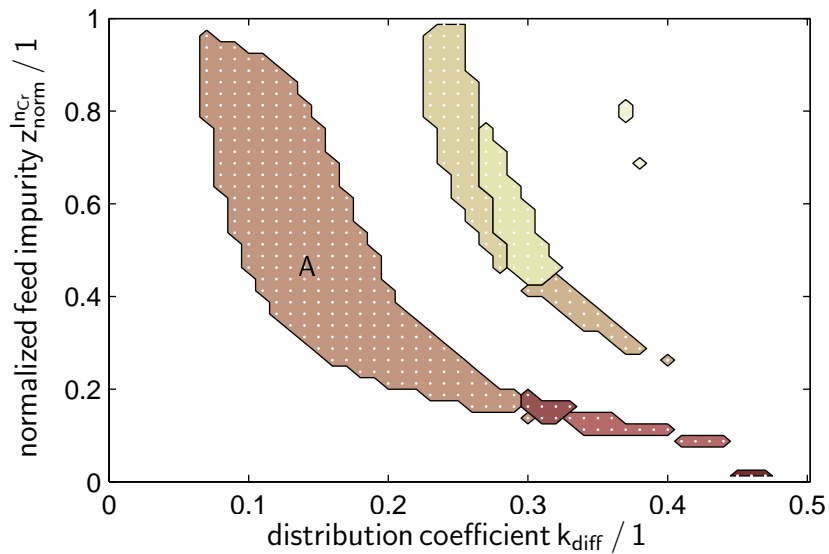


Figure 3.9: Case 1. Globally optimal configuration of countercurrent crystallizer cascade defined by number of stages and feed stage. Each patch represents a configuration with a different combination of number of stages and feed stage according to Figure 3.7 and Figure 3.8. The dotted line shows optimal configurations for fixed distribution coefficient values and varied feed concentrations.

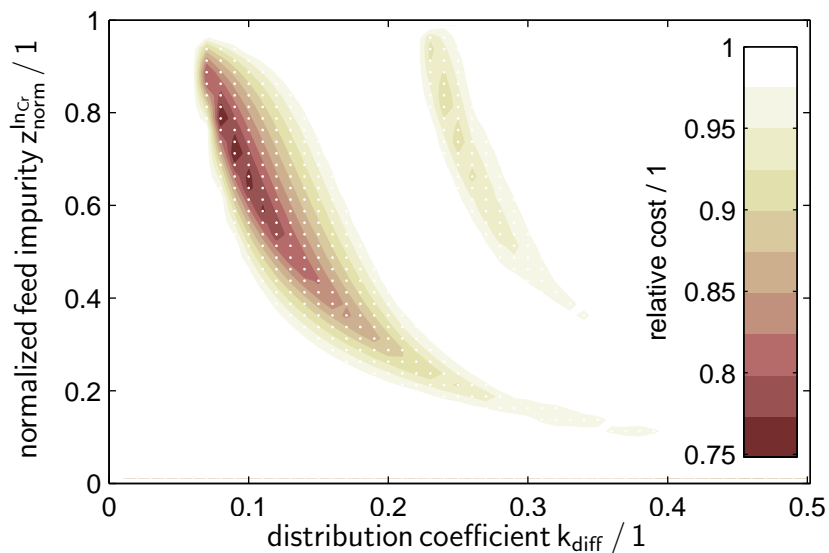
Next, optimal alternative configurations are discussed with regard to the results for countercurrent cascades. General configurations are characterized by the number of stages, the feed stage position and the transport of crystal product and of liquid remainder between stages. Recall that for countercurrent cascades the crystal product is always transported to the stage with the next lower number, and liquid remainder is transported to the stage with the next higher number. For general configurations, connections between stages are not limited to neighboring stages.

Parameter regions with optimal configurations different from the countercurrent cascade are shown in Figure 3.10a. Regions with identical configurations except for liquid remainder connections β^L are represented as single patches in that figure. Regions where the countercurrent cascade is the optimal configuration are not drawn for the sake of clarity. In Figure 3.10b, the objective value J_{TAC} of optimal alternative configurations relative to the countercurrent cascade is given.

The results show large parameter regions with alternative configurations better



(a) Parameter regions with optimal alternative configurations.



(b) Relative cost of alternative configurations.

Figure 3.10: Case 1. (a) Globally optimal configuration of general crystallizer network determined by stage number, feed stage and crystal product transport. Only regions with optimal solutions that are different from the countercurrent cascade are shown. The region with the largest differences is marked with A. (b) Relative cost of alternative configurations compared to the countercurrent cascade.

than the countercurrent cascade. Those regions are located around boundaries between the regions depicted in Figure 3.8, i. e. regions with different optimal feed stage positions for the countercurrent cascade. This is valid regardless of the optimal number of stages. The largest improvements, with over 20 % less cost for alternative configurations, are achieved in region A, which is also the parameter region where the optimal feed position of a two-stage countercurrent cascade switches from first to second stage, see Figure 3.9. Differences between optimal alternative configurations and optimal countercurrent cascades are less pronounced for larger numbers of stages and feed stage numbers.

Region A, the parameter region with the largest possible improvements, is now considered in more detail. Located where the optimal countercurrent cascade has two stages and the feed position switches from first to second stage, this region represents three different globally optimal alternative configurations. All optimal configurations, depicted in Figure 3.11, have three stages, the same feed position and the same crystal product connections. However, the liquid remainder from the first stage is transported to a different stage for each configuration.

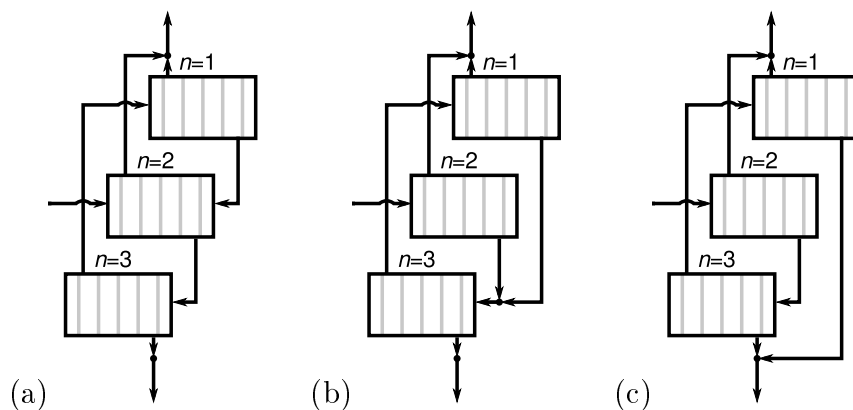


Figure 3.11: Case 1. Equivalent globally optimal configurations for region A in Figure 3.10.

Repeating the parameter study for each fixed configuration verifies that the same objective function values are reached within region A. Only configuration (c) is infeasible in a part of region A and has different optimal objective values if the configuration is close to being infeasible.

Optimization results for a selected set of parameters are given in Figure 3.12 as an example for the interpretation of the entire parameter region A. Config-

uration (b) is used for this example due to being a direct extension of countercurrent design (see Figure 3.12c).

For all three optimal configurations in parameter region A, the second stage is used as the feed stage. This feed stage generates crystal product with purity below specification. The liquid remainder of the feed stage is then purified to above specification by the remaining two stages. The crystal product with purity above specification is mixed with the crystal product of the feed stage to exactly meet the product specification. Using this structure avoids crystallizing the whole product amount twice, as is the case for countercurrent configurations with two stages and the second stage as feed position (Figure 3.12b). It also avoids large recycles from a stripping stage in the case of the first stage being the feed position and the feed composition being far from the product specification (Figure 3.12a). Instead, there is a “pre-treatment” stage that removes as much product as possible below the purity specification so that the specification is still met by mixing with product from a two-stage crystallizer.

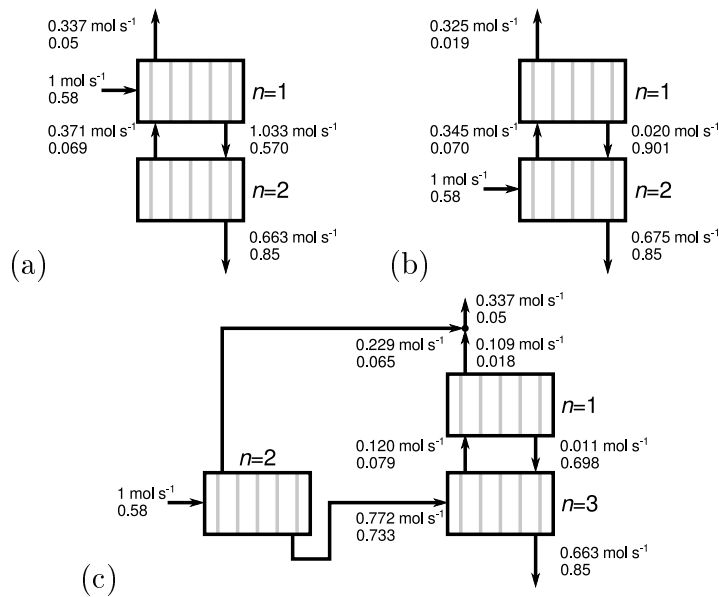


Figure 3.12: Case 1. Optimal operating parameters for selected configurations with $k_{\text{eff}} = 0.1$ and $z_{\text{norm}}^{\text{InCr}} = 0.6625$, corresponding to region A in Figure 3.10. Pairs of numbers represent molar flows and molar fractions of impurity. Configuration (c), equal to configuration (b) in Figure 3.11, is rearranged for better readability.

The computational effort for characterizing globally optimal designs for sepa-

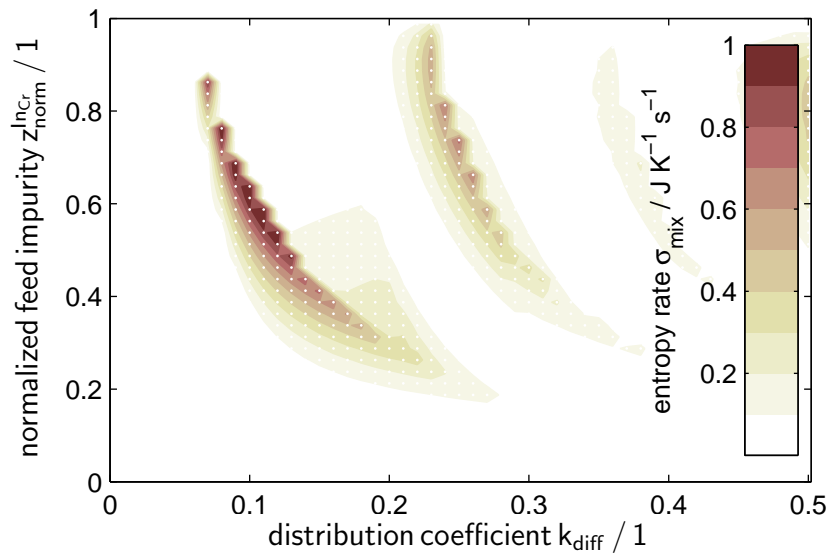
ration networks using parameter studies is significant. If a suitable measure for inefficiency is available, alternative configurations only have to be determined for inefficient countercurrent cascades, thus reducing computational effort. In the following, re-mixing of purified intermediate products is studied as a possible measure of inefficiency in crystallizer networks.

The production rate of entropy of mixing σ_{mix} is a measure for mixing inefficiencies. The entropy of mixing in crystallizer networks is determined by the entropy difference between all molar flows connected to each mixing point and the resulting mixed flows. The total entropy production rate σ_{mix} of a crystallizer network, assuming mixing of ideal liquids [Stephan et al., 2010], is then calculated as

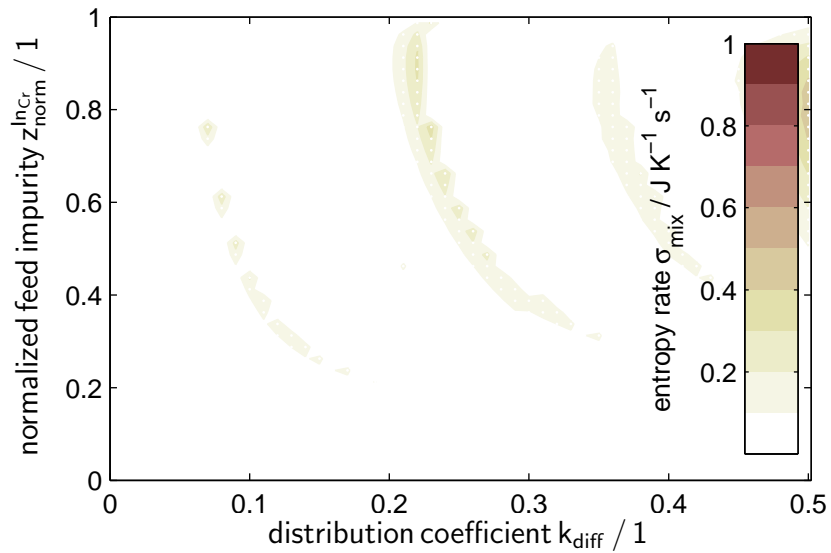
$$\begin{aligned}
\sigma_{\text{mix}} = & \text{R} \sum_{n=1}^{n^{\text{Cr}}} L_n (x_{\text{imp},n} \ln(x_{\text{imp},n}) + (1 - x_{\text{imp},n}) \ln(1 - x_{\text{imp},n})) \\
& + \text{R} \sum_{n=1}^{n^{\text{Cr}}} S_n (w_{\text{imp},n} \ln(w_{\text{imp},n}) + (1 - w_{\text{imp},n}) \ln(1 - w_{\text{imp},n})) \\
& + \text{R} F^{\text{InCr}} (z_{\text{imp}}^{\text{InCr}} \ln(z_{\text{imp}}^{\text{InCr}}) + (1 - z_{\text{imp}}^{\text{InCr}}) \ln(1 - z_{\text{imp}}^{\text{InCr}})) \\
& - \text{R} \sum_{n=1}^{n^{\text{Cr}}} F_n (z_{\text{imp},n} \ln(z_{\text{imp},n}) + (1 - z_{\text{imp},n}) \ln(1 - z_{\text{imp},n})) \\
& - \text{R} F^{\text{Out1Cr}} (z_{\text{imp}}^{\text{Out1Cr}} \ln(z_{\text{imp}}^{\text{Out1Cr}}) + (1 - z_{\text{imp}}^{\text{Out1Cr}}) \ln(1 - z_{\text{imp}}^{\text{Out1Cr}})) \\
& - \text{R} F^{\text{Out2Cr}} (z_{\text{imp}}^{\text{Out2Cr}} \ln(z_{\text{imp}}^{\text{Out2Cr}}) + (1 - z_{\text{imp}}^{\text{Out2Cr}}) \ln(1 - z_{\text{imp}}^{\text{Out2Cr}})) .
\end{aligned} \tag{3.43}$$

The results in Figure 3.13 show increased entropy production for countercurrent cascades at boundaries of regions with constant optimal feed position according to Figure 3.8, indicating that increased re-mixing reduces the efficiency of one configuration up to the point where another configuration becomes more efficient. In contrast to countercurrent cascades, entropy production for optimal alternative configurations is significantly lower. According to Figure 3.10a, increased entropy production for countercurrent cascades is only encountered where alternative configurations are globally optimal. Large values of entropy production are found close to boundaries of regions with constant optimal feed stage position, on the side of smaller feed position values. Re-mixing is suitable to identify these inefficient countercurrent configurations, allowing for faster screening for improved alternative configurations. However, there are also parameter regions where both the globally optimal alternative configuration and

the countercurrent cascade have low entropy production. Thus, identifying the whole region of optimal alternative configurations still requires according parameter studies.



(a) Countercurrent cascade.



(b) Alternative configurations.

Figure 3.13: Case 1. Entropy production rate for cost-optimal configuration as a measure for inefficiency caused by re-mixing.

Case 2: High Product Yield and Purity In the previous parameter study, all model parameters except for purity requirements and cost coefficients in the objective function are varied. In this parameter study, increased purity requirements are considered. Results are generated in the same way as for low product yield and purity and compared to that case. Parameter and domain specifications for this case are given in Table 3.4. The parameter study is done for countercurrent cascades according to Equations (3.39)-(3.42) and for general configurations.

Table 3.4: Case 2. Parameter and domain specifications for influence of parameters on globally optimal configuration.

parameter	value	variable	domain
k_{diff}	$\{0.01, 0.02, \dots, 0.5\}$	$z_{\text{imp}}^{\text{Out1Cr}}$	$[0, 0.01]$
$z_{\text{imp}}^{\text{InCr}}$	$\{0.02, 0.04, \dots, 0.88\}$	$z_{\text{imp}}^{\text{Out2Cr}}$	$[0.89, 1]$
$F_{\text{imp}}^{\text{InCr}}$	1 mol s^{-1}	z, Y, k	$[0, 1]$
$x_{\text{imp}}^{\text{max}}$	0.9	S, L, F	$[0 \text{ mol s}^{-1}, 20 \text{ mol s}^{-1}]$
n^{Cr}	$\{1, 2, 3, 4\}$	β	$\{0, 1\}$

Optimal number of stages and feed stage positions for countercurrent cascades, depicted in Figure 3.14 and Figure 3.15, are qualitatively the same as for low product yield and purity. Increased purity requirements lead to a larger number of required stages and a larger feed stage number for the same separation efficiency. Accordingly, regions representing certain numbers of stages in Figure 3.14 are shifted to lower distribution coefficient values compared to Figure 3.7. Regions representing certain feed stage positions in Figure 3.15 are also shifted to lower distribution coefficient values compared to Figure 3.8.

Globally optimal configurations different from the countercurrent cascade are found at the boundary of regions with constant countercurrent feed position, compare Figure 3.15 and Figure 3.16. The number of regions with different optimal configurations and their relative position to each other is identical to Case 1. Similar to Case 1, the largest improvements are found in region A, where the optimal feed position for two-stage countercurrent cascades switches from first to second stage. The region of interest is shifted to lower distribution coefficient values due to increased purity requirements and the cost reduction compared to countercurrent cascades is slightly higher than in Case 1.

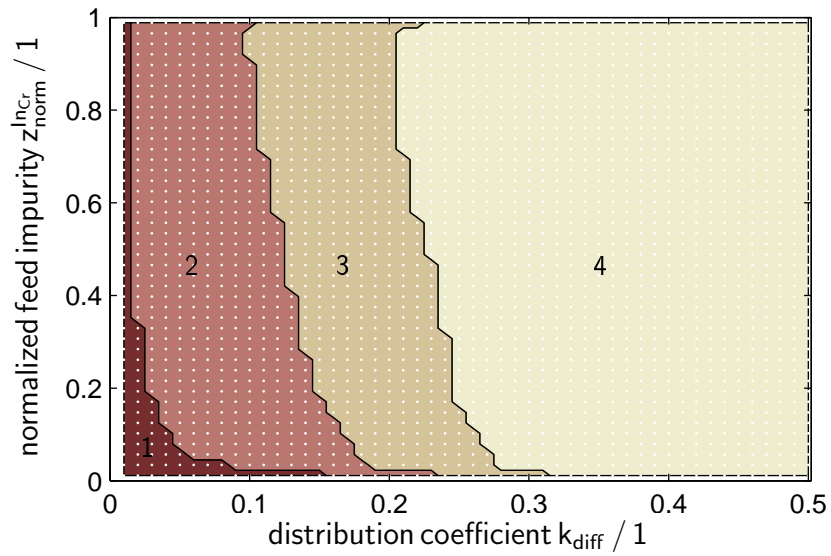


Figure 3.14: Case 2. Globally optimal number of stages of countercurrent crystallizer cascade, from one stage in the lower left region to four stages in the upper right region.

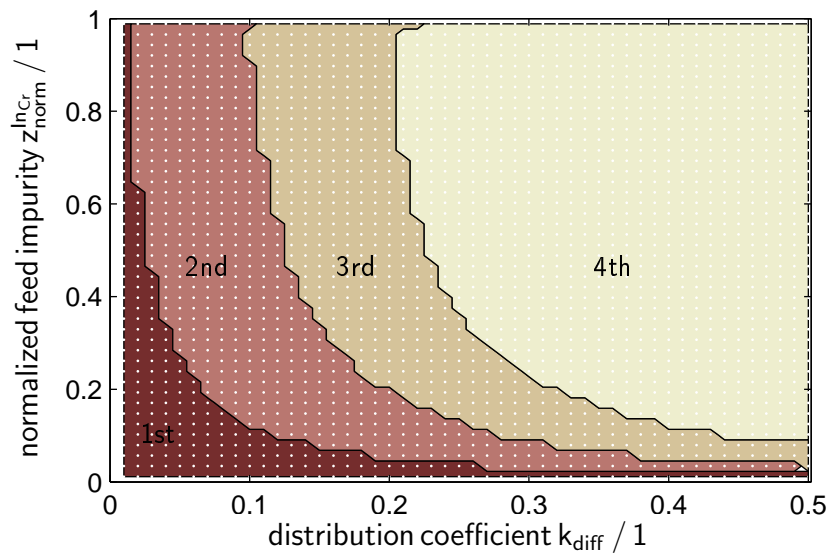
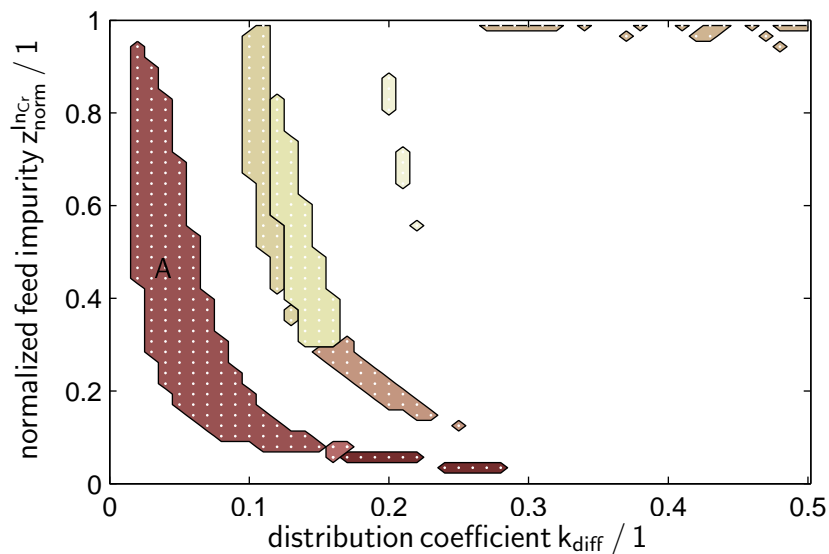
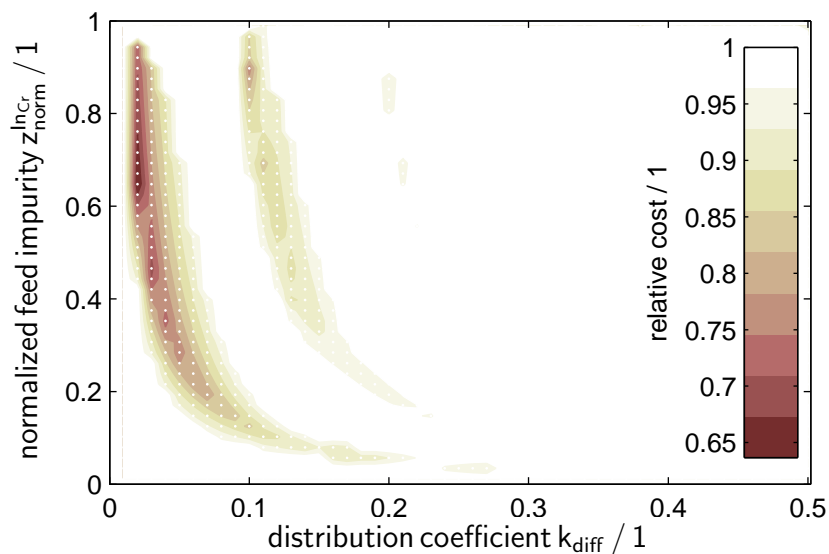


Figure 3.15: Case 2. Globally optimal feed stage of countercurrent crystallizer cascade, from first stage in the lower left region to fourth stage in the upper right region.



(a) Parameter regions with optimal alternative configurations.



(b) Relative cost of alternative configurations.

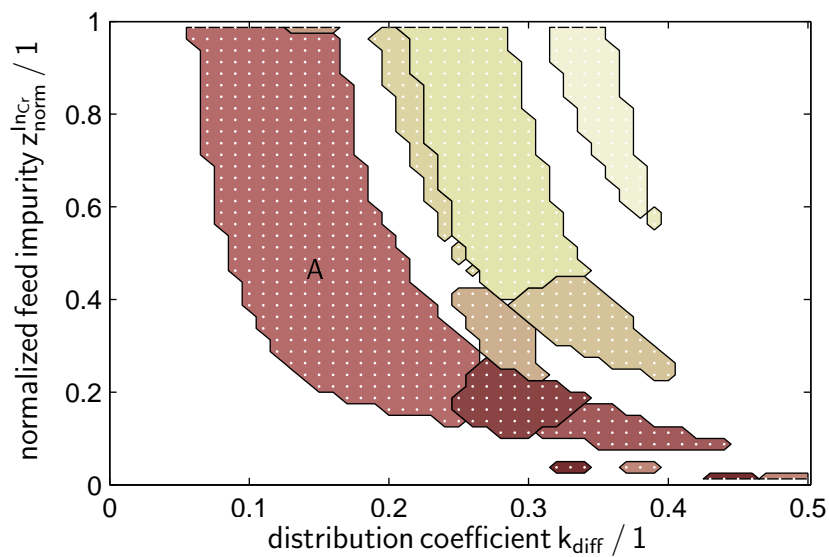
Figure 3.16: Case 2. (a) Globally optimal configurations of general crystallizer separation network determined by stage number, feed stage and crystal product transport between stages. Only regions with optimal configurations that are different from the countercurrent cascade are shown. The region with the largest differences is marked with A. (b) Relative cost of alternative configurations compared to the countercurrent cascade.

Case 3: Crystallization Effort as Objective Function In melt crystallization, the amount of crystal produced by a single stage determines the energy consumption and equipment size of that stage and thus the cost. Consequently, process costs for multistage crystallization networks are determined by the crystallization effort, i. e. the amount of crystal produced on all single stages, see Equation (3.20). In general, lower crystallization effort for a given separation task indicates more energy efficiency and less equipment size. Therefore, the crystallization effort allows for rating multistage melt crystallization processes and comparing them with other multistage separation processes using equivalent objective functions. Results for optimal melt crystallization networks with the crystallization effort as the objective function are given below.

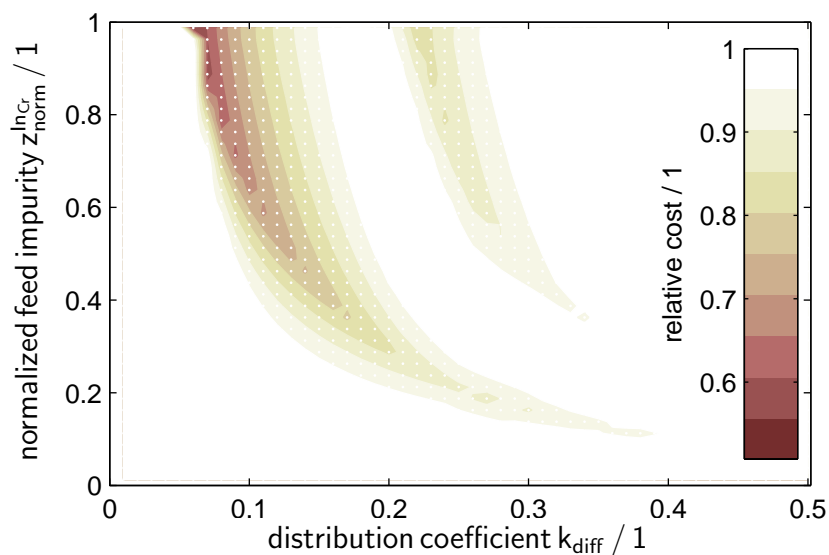
Note that the previous cases are already generated by minimizing the crystallization effort for fixed numbers of stages and then selecting the number of stages with the lowest economic cost. Results for the present case are generated by re-evaluating the optimization results of Case 1 for the crystallization effort as the objective function, i. e. from optimization results with fixed numbers of stages $n^{\text{Cr}} = 1, 2, 3, 4$ the result with the lowest crystallization effort is chosen. Recall, if the same objective value is achieved within 1% tolerance with different numbers of stages, the lowest number of stages is reported. Parameters for Case 3 are given in Table 3.3.

The resulting regions with globally optimal alternative configurations and their relative objective values compared to countercurrent cascades is given in Figure 3.17.

Optimal configurations found for Case 1 are also the optimal configurations for Case 3 and vice versa in corresponding parameter regions, e. g. region A in Figure 3.17 has the same optimal configurations as region A in Figure 3.10. This means, the crystallization effort is a suitable objective function for characterizing optimal multistage configurations on this level of modeling detail. However, the boundaries of optimal parameter regions are shifted. There are also some additional regions with alternative configurations that show only negligible improvements compared to countercurrent cascades.



(a) Parameter regions with optimal alternative configurations.



(b) Relative crystallization effort of alternative configurations.

Figure 3.17: Case 3. (a) Globally optimal configurations of general crystallizer separation network determined by stage number, feed stage and crystal product transport. Only regions with optimal configurations that are different from the countercurrent cascade are shown. The region with the largest differences is marked with A. (b) Relative crystallization effort of alternative configurations compared to the countercurrent cascade.

3.2.5 Conclusion

All results are generated using deterministic global optimization ruling out non-optimal local solutions as a possible source for misinterpretations. Parameter studies on melt crystallization networks reveal that alternative configurations are significantly more efficient than countercurrent cascades in certain regions of process parameters, with up to 35% economical cost reduction observed for considered cases. Process cost is reduced by decreasing the overall crystallization effort through introduction of an additional stage. The cost of this additional stage is compensated by reduced crystallizer sizes due to reduced re-mixing of purified intermediate product and by avoiding to crystallize a part of the final product twice.

The parameter regions of interest are easily found by investigating countercurrent configurations, which require low computational effort to solve. The search for alternative configurations should be considered at boundaries of regions with constant optimal feed position for countercurrent cascades. A quick screening for inefficient countercurrent cascades is also possible by testing for increased re-mixing. This will not identify configurations that are inefficient in some other way.

Possible cost savings for alternative configurations are largest where optimal countercurrent cascades have two stages and the feed position switches from first to second stage. For that case it is sufficient to consider one alternative configuration beside countercurrent cascades. This lowers computational or experimental effort for finding the optimal configuration even further.

3.3 Solution Crystallization

Solution crystallization is used to separate components of a mixture dissolved in a solvent. Supersaturation of the solution and thus crystallization is induced by solvent removal. Theoretically, pure crystals can be achieved in one crystallization step for eutectic mixtures. However, as discussed in the previous section, impurity inclusions may require repeated crystallization to achieve desired product purity or yield. The same is valid for mixtures forming solid solutions, i. e. solids in which components form a single homogeneous phase. A phase diagram for components A and B forming a solid solution without additional solvent is depicted in Figure 3.18. Each composition in the liquid phase corresponds to a unique equilibrium composition in the solid phase. Therefore, it is not possible to produce pure crystals from a mixture in one crystallization step.

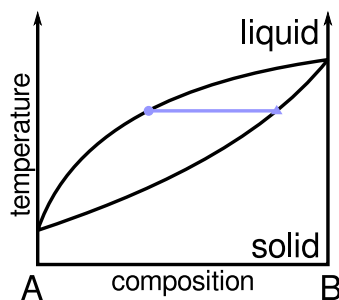


Figure 3.18: Exemplary phase diagram for solid solutions without an additional solvent. The horizontal line represents corresponding equilibrium compositions in the solid and liquid phase.

Dissolving the mixture of A and B in an additional solvent leads to a phase diagram with three components, e. g. potassium sulfate and ammonium sulfate in water in Figure 3.19. Corresponding equilibrium compositions in the liquid and solid phase are different from each other, allowing for separation of the binary mixture by repeated crystallization and dissolving.

In a recent study [Münzberg et al., 2016], a countercurrent stage-wise crystallization process was found to be an efficient means to separate a solid solution. The considerations in that study are extended here to include configurations different from the countercurrent cascade. The influence of parameters on optimal design of multistage solution crystallization processes is shown in com-

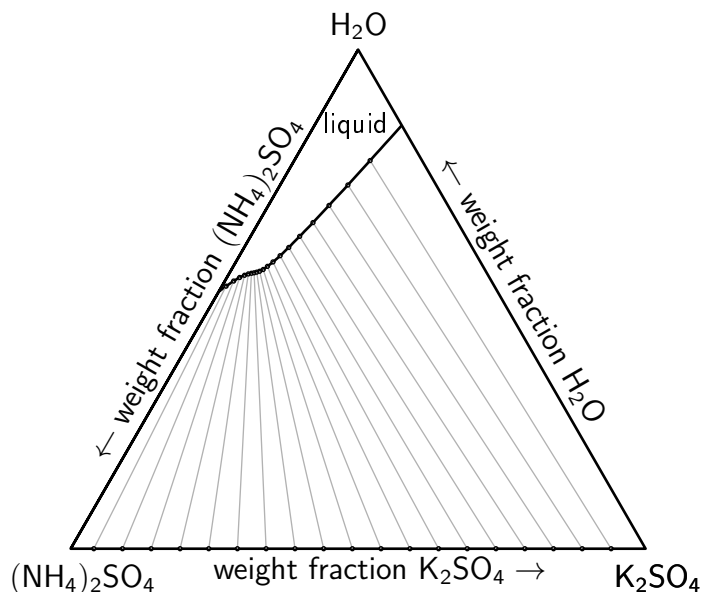


Figure 3.19: Phase diagram of potassium sulfate, ammonium sulfate and water at 65 °C, with potassium sulfate and ammonium sulfate forming solid solutions. Corners represent pure components and edges binary mixtures. Gray lines depict corresponding equilibrium compositions in the solid and liquid phase. Model from [Münzberg et al., 2016], based on experimental data.

parison to the results for melt crystallization in Section 3.2.4.

3.3.1 Process Model

Single Units

The following crystallization model is taken from [Münzberg et al., 2016]. The model describes batch-wise operated crystallization units. Each crystallization unit performs the steps depicted in Figure 3.20. The feed to a unit consists of a liquid mixture potentially also including crystals. Solvent is added to the mixture to dissolve any crystals. In the actual crystallization step, solvent is removed to induce crystallization. Finally, crystals and mother liquor are separated and transferred to other units.

In [Münzberg et al., 2016], the production cycle is repeated to allow for semi-continuous production and thus the compositions of feed and product mass in each unit change from cycle to cycle. The original model is adapted here for the limiting case of steady state operation of the process, i. e. compositions in

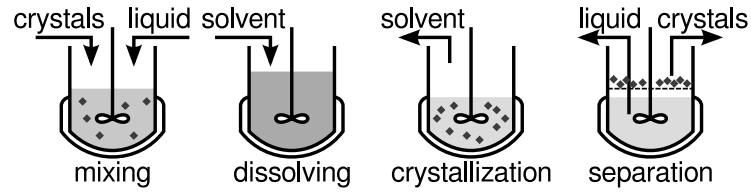


Figure 3.20: Steps in each crystallization unit.

each unit are constant between cycles. In steady state, averaged mass flows are defined as ratios of feed or product masses and a given production cycle time. The following model is given in terms of averaged mass flows for better comparability with the results in Section 3.2. Mass flows of component “A” enriched in the solid phase and cumulated mass flows of both components “AB” are used as variables. Mass flows for solvent “S” are calculated when required. The original model is further adapted to reduce the number of variables and nonlinearities.

Crystallization units as in Figure 3.21 are numbered by $n = 1, \dots, n^{\text{Cr}}$, with feed mass flow $F_{i,n}$, crystal product mass flow $S_{i,n}$ and liquid remainder mass flow $L_{i,n}$ for components $i = \text{A, AB, S}$. Calculating the feed flow for each unit by

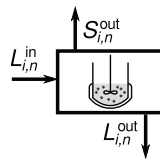


Figure 3.21: Single solution crystallization unit with feed mass flow $F_{i,n}$, crystal product mass flow $S_{i,n}$ and liquid remainder mass flow $L_{i,n}$ for components $i = \text{A, AB, S}$.

mixing product flows from other units is covered by the network model given further below. The solvent content of the overall feed is adjusted to dissolve any crystals and keep the solution in a saturated state. Since, by definition, there are no crystals, the required solvent mass is calculated by assuming that the solution is in equilibrium with a virtual solid phase. The phase equilibrium is given by polynomial fits to experimental data using mass fractions $x_{i,n}$ in the feed mass flow $L_{i,n}^{\text{in}}$ and in the virtual solid phase $w_{i,n}$ with according index

of components i . Resulting equations for the dissolution step are given below.

$$L_{A,n}^{\text{in}} = x_{A,n}^{\text{in}} (L_{AB,n}^{\text{in}} + L_{S,n}^{\text{in}}) \quad (3.44)$$

$$L_{S,n}^{\text{in}} = x_{S,n}^{\text{in}} (L_{AB,n}^{\text{in}} + L_{S,n}^{\text{in}}) \quad (3.45)$$

$$x_{A,n}^{\text{in}} = \sum_{k=0}^3 a_{A,k} (w_{A,n}^{\text{in}})^k \quad (3.46)$$

$$x_{S,n}^{\text{in}} = \sum_{k=0}^3 a_{S,k} (w_{A,n}^{\text{in}})^k \quad (3.47)$$

Solvent is removed to induce crystallization. Crystallization proceeds until the solution is in equilibrium with the solid phase, i.e. the crystals. Solvent content after the crystallization step is determined in the same way as for the dissolution step. The superscript “cryst” denotes the state at the end of the crystallization step.

$$L_{A,n}^{\text{cryst}} = x_{A,n}^{\text{cryst}} (L_{AB,n}^{\text{cryst}} + L_{S,n}^{\text{cryst}}) \quad (3.48)$$

$$L_{S,n}^{\text{cryst}} = x_{S,n}^{\text{cryst}} (L_{AB,n}^{\text{cryst}} + L_{S,n}^{\text{cryst}}) \quad (3.49)$$

$$x_{A,n}^{\text{cryst}} = \sum_{k=0}^3 a_{A,k} (w_{A,n}^{\text{cryst}})^k \quad (3.50)$$

$$x_{S,n}^{\text{cryst}} = \sum_{k=0}^3 a_{S,k} (w_{A,n}^{\text{cryst}})^k \quad (3.51)$$

Filtration is used to separate crystals from mother liquor. However, some mother liquor may stick to the crystals. With zero solvent content in the crystals themselves $S_{S,n}^{\text{cryst}} = 0$, the crystal product including adherent mother liquor proportional to the crystal mass $S_{AB,n}^{\text{cryst}}$ is calculated as follows, with ratio parameter κ and superscript “out” denoting the state after filtration. Note that the composition of the mother liquor does not change in this step.

$$S_{i,n}^{\text{out}} = S_{i,n}^{\text{cryst}} + \kappa S_{AB,n}^{\text{cryst}} x_{i,n}^{\text{cryst}}, \quad i = A, AB, S \quad (3.52)$$

$$x_{i,n}^{\text{out}} = x_{i,n}^{\text{cryst}}, \quad i = A, AB, S \quad (3.53)$$

Product mass flows and compositions directly after crystallization are not required for evaluation of the objective function. The desired outputs after filtration are calculated directly by using Equations (3.52)-(3.53). The phase

equilibrium after crystallization, i. e. Equations (3.50)-(3.51), still applies.

$$S_{S,n}^{\text{out}} = \frac{\kappa}{1 + \kappa} x_{S,n}^{\text{cryst}} (S_{AB,n}^{\text{out}} + S_{S,n}^{\text{out}}) \quad (3.54)$$

$$S_{A,n}^{\text{out}} = \left(\frac{1}{1 + \kappa} w_{A,n}^{\text{cryst}} + \frac{\kappa}{1 + \kappa} x_{A,n}^{\text{cryst}} \right) (S_{AB,n}^{\text{out}} + S_{S,n}^{\text{out}}) \quad (3.55)$$

$$L_{A,n}^{\text{out}} = x_{A,n}^{\text{cryst}} (L_{AB,n}^{\text{out}} + L_{S,n}^{\text{out}}) \quad (3.56)$$

$$L_{S,n}^{\text{out}} = x_{S,n}^{\text{cryst}} (L_{AB,n}^{\text{out}} + L_{S,n}^{\text{out}}) \quad (3.57)$$

In addition, the mass balance equations for the whole crystallization unit read

$$L_{i,n}^{\text{in}} = L_{i,n}^{\text{out}} + S_{i,n}^{\text{out}}, \quad i = A, AB. \quad (3.58)$$

Note that the mass balance of solvent is not used here due to addition and removal of solvent in intermediate steps.

The implicit equation system for calculating a single crystallization unit has one remaining degree of freedom. The amount of solvent removed during crystallization determines purity and yield of the product of a unit, enabling optimization of the process.

The crystallization model comprises Equations (3.44)-(3.47), Equations (3.50)-(3.51) and Equations (3.54)-(3.58). Note that a version of the crystallization model adapted for scalable separation efficiency is introduced for the parameter studies in subsequent Section 3.3.2.

Network of Crystallizer Units

In [Münzberg et al., 2016], crystallization units are interconnected to form a separation network. In particular, countercurrent operation is studied, i. e. mother liquor and crystals of each unit are transferred to neighboring units to be further processed. Here, a network for separating a mixture of two components equivalent to that in Section 3.2, with crystallization stages $n = 1, \dots, n^{\text{Cr}}$ numbered downwards, is considered. Adjustments are made to the model of the separation network to account for using solution crystallization instead of melt crystallization, particularly adding a solvent component to the model. Each stage n separates a feed flow into crystal product and liquid remainder. The feed of each stage $L_{i,n}^{\text{in}}$ is the sum of all crystal flows $S_{i,l}^{\text{out}}$ and mother liquor flows $L_{i,l}^{\text{out}}$ connected to that stage and, if applicable for that stage, the crystallization network feed flow F_i^{InCr} with $i = A, AB, S$. The distribution of the feed

flow and connections between stages are implemented using binary variables $\beta_n^{\text{InCr}} \in \{0, 1\}$, $\beta_{l,n}^{\text{S}} \in \{0, 1\}$ and $\beta_{l,n}^{\text{L}} \in \{0, 1\}$, $n = 1, \dots, n^{\text{Cr}}$, $l = 1, \dots, n^{\text{Cr}}$. The variables β_n^{InCr} , $\beta_{l,n}^{\text{S}}$ and $\beta_{l,n}^{\text{L}}$ attain a value of one if and only if the feed enters at stage n , the crystal flow of stage l is fed to stage n and the liquid remainder flow of stage l is fed to stage n , respectively. Feed mass balance equations for each stage $n = 1, \dots, n^{\text{Cr}}$ then read

$$L_{i,n}^{\text{in}} = F_i^{\text{InCr}} \beta_n^{\text{InCr}} + \sum_{l=1}^{n^{\text{Cr}}} L_{i,l}^{\text{out}} \beta_{l,n}^{\text{L}} + \sum_{l=1}^{n^{\text{Cr}}} S_{i,l}^{\text{out}} \beta_{l,n}^{\text{S}}, \quad i = \text{A, AB}. \quad (3.59)$$

The solvent mass after mixing for each stage $n = 1, \dots, n^{\text{Cr}}$ is calculated as

$$L_{\text{S},n}^{\text{mix}} = \sum_{l=1}^{n^{\text{Cr}}} L_{\text{S},l}^{\text{out}} \beta_{l,n}^{\text{L}} + \sum_{l=1}^{n^{\text{Cr}}} S_{\text{S},l}^{\text{out}} \beta_{l,n}^{\text{S}}. \quad (3.60)$$

It is ensured that the feed enters exactly one stage by

$$\sum_{n=1}^{n^{\text{Cr}}} \beta_n^{\text{InCr}} = 1. \quad (3.61)$$

The output flow of each stage is connected to exactly one stage input or one crystallizer product output by

$$\sum_{n=1}^{n^{\text{Cr}}} \beta_{l,n}^{\text{S}} + \beta_l^{\text{S,Out1Cr}} = 1, \quad l = 1, \dots, n^{\text{Cr}}, \quad (3.62)$$

$$\sum_{n=1}^{n^{\text{Cr}}} \beta_{l,n}^{\text{L}} + \beta_l^{\text{L,Out2Cr}} = 1, \quad l = 1, \dots, n^{\text{Cr}}, \quad (3.63)$$

with $\beta_l^{\text{S,Out1Cr}} \in \{0, 1\}$ attaining value 1 if and only if the crystal product output of stage l is connected to output Out1_{Cr} and with $\beta_l^{\text{L,Out2Cr}} \in \{0, 1\}$ attaining value 1 if and only if the liquid remainder output of stage l is connected to output Out2_{Cr} . The product flows are then calculated as

$$F_i^{\text{Out1Cr}} = \sum_{n=1}^{n^{\text{Cr}}} \beta_n^{\text{S,Out1Cr}} S_{i,n}, \quad i = \text{A, AB}, \quad (3.64)$$

$$F_i^{\text{Out2Cr}} = \sum_{n=1}^{n^{\text{Cr}}} \beta_n^{\text{L,Out2Cr}} L_{i,n}, \quad i = \text{A, AB}. \quad (3.65)$$

Solvent is completely removed from the products. Product specifications are given as bounds to mass fractions of component A at both outlets, $z_{\text{A}}^{\text{Out1Cr}}$ and

z_A^{Out2Cr} :

$$z_{A,\min}^{\text{Out1Cr}} F_{AB}^{\text{Out1Cr}} \leq F_A^{\text{Out1Cr}}, \quad (3.66)$$

$$z_{A,\max}^{\text{Out2Cr}} F_{AB}^{\text{Out2Cr}} \geq F_A^{\text{Out2Cr}}. \quad (3.67)$$

It is assumed that the stages are ordered in terms of feed composition. The solid mass fraction of component A, enriched in the solid phase, is denoted as w_A .

$$w_{A,n}^{\text{in}} \geq w_{A,n+1}^{\text{in}}, \quad n = 1, \dots, n^{\text{Cr}} - 1 \quad (3.68)$$

Crystals are enriched in component A and mother liquor in component B. Therefore, crystals are always transported in one direction of the crystallizer cascade and mother liquor in the opposite direction.

$$\beta_{l,n}^{\text{S}} = 0 \quad \text{for all } 1 \leq l \leq n, \quad n = 1, \dots, n^{\text{Cr}} \quad (3.69)$$

$$\beta_{l,n}^{\text{L}} = 0 \quad \text{for all } n \leq l \leq n^{\text{Cr}}, \quad n = 1, \dots, n^{\text{Cr}} \quad (3.70)$$

All potential connections within the crystallizer network used in this work are illustrated in Figure 3.22a for a fixed number of stages $n^{\text{Cr}} = 3$. The countercurrent cascade depicted in Figure 3.22b serves as the benchmark for any other configuration within this superstructure.

The overall mass balances for the whole process are added to the model to improve computational performance.

$$F_i^{\text{InCr}} = F_i^{\text{Out1Cr}} + F_i^{\text{Out2Cr}}, \quad i = A, AB. \quad (3.71)$$

Mass flows at the outlet are bounded by inlet mass flows according to

$$\text{up}(F_i^{\text{Out1Cr}}) = F_i^{\text{InCr}}, \quad \text{up}(F_i^{\text{Out2Cr}}) = F_i^{\text{InCr}}, \quad i = A, AB. \quad (3.72)$$

The separation network comprises Equations (3.59)-(3.68) and Equation (3.71). Equations (3.69)-(3.70) and Equation (3.72) are implemented as bounds to respective variables.

Objective Function

Both equipment size and energy consumption of solution crystallization processes scale with the amount of solvent that needs to be evaporated. The

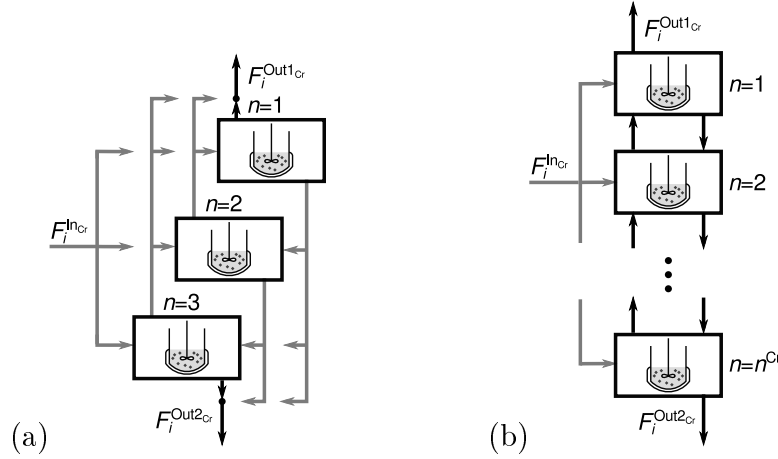


Figure 3.22: (a) Crystallizer network consisting of $n^{Cr} = 3$ stages with arbitrary configuration. (b) Countercurrent crystallizer cascade with n^{Cr} stages and arbitrary feed stage ($\beta_{l,l-1}^S = 1, l = 2, \dots, n^{Cr}, \beta_{l,l+1}^L = 1, l = 1, \dots, n^{Cr} - 1, \beta_1^{S,Out1_{Cr}} = 1, \beta_{n^{Cr}}^{L,Out2_{Cr}} = 1$).

evaporation effort J_{evap} is defined in [Münzberg et al., 2016] as the ratio of total evaporated solvent to total feed without solvent. The objective function accounts for solvent evaporated on each crystallization stage $V_{S,n}$ as well as solvent that needs to be removed from the products.

$$J_{evap} = \frac{\sum_{n=1}^{n^{Cr}} V_{S,n} + \beta_n^{Out1} S_{S,n}^{out} + \beta_n^{Out2} L_{S,n}^{out}}{F_{AB}^{In_{Cr}}} \quad (3.73)$$

The mass of evaporated solvent is determined by the solvent content before and after crystallization. The solvent content before crystallization is the maximum of the solvent content directly after mixing and after the dissolution step. This covers the case that, after mixing, there is already enough solvent to dissolve all crystals. Since the evaporation effort J_{evap} is to be minimized, the evaporated solvent $V_{S,n}$ for each stage $n = 1, \dots, n^{Cr}$ is implemented as

$$V_{S,n} \geq L_{S,n}^{mix} - L_{S,n}^{out} - S_{S,n}^{out}, \quad (3.74)$$

$$V_{S,n} \geq L_{S,n}^{in} - L_{S,n}^{out} - S_{S,n}^{out}. \quad (3.75)$$

The objective function model comprises Equations (3.73)-(3.75).

3.3.2 Computational Studies

This section deals with computational results based on the model for multistage solution crystallization given above. The model behavior is analyzed below

based on parameter studies of globally optimal solutions.

Selectivity Scaling

The following parameter studies include variation of the separation efficiency of the process. The original model from [Münzberg et al., 2016] does not contain this option in a straight-forward way. An analogy between separation efficiency of distillation and solution crystallization drawn in [Münzberg et al., 2016] is used here to enable scaling of separation efficiency. The separation of species A and B is characterized regardless of solvent content by using dry mass fractions in the liquid phase x_i^{dry} and in the solid phase w_i^{dry} defined as

$$w_i^{\text{dry}} := w_i, \quad i = A, B \quad (3.76)$$

$$x_i^{\text{dry}} := \frac{x_i}{x_A + x_B}, \quad i = A, B. \quad (3.77)$$

Similar to phase equilibrium diagrams used in binary distillation, an equilibrium diagram for solution crystallization is depicted in Figure 3.23. The figure shows how the composition of a solid phase in equilibrium with a liquid phase depends on the composition of that liquid phase. Phase equilibrium

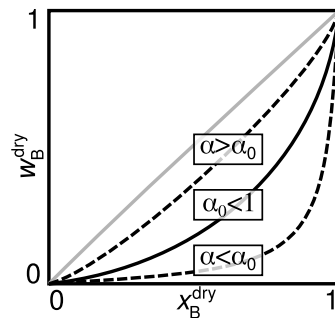


Figure 3.23: Influence of relative selectivity α on the solid-liquid phase equilibrium. Increasing α increases the equilibrium concentration of B in the solid phase.

lines farther from the diagonal mean larger differences between crystal and liquid composition and therefore better separation efficiency. In ideal binary distillation, the equilibrium line is determined by the relative volatility of both components. A measure for separation efficiency analogous to the relative volatility is defined for crystallization as

$$w_B^{\text{dry}} = \frac{\alpha_B x_B^{\text{dry}}}{\alpha_A x_A^{\text{dry}} + \alpha_B x_B^{\text{dry}}}, \quad (3.78)$$

with relative selectivity for the component enriched in the solid phase $\alpha_A := 1$ and relative selectivity for the component depleted in the solid phase α_B . According to Equation (3.76) and Equation (3.77), dry mass fractions are substituted to obtain

$$w_B = \frac{\alpha_B x_B}{x_A + \alpha_B x_B}. \quad (3.79)$$

Rewriting Equation (3.79) allows for calculating α_B from actual solid-liquid phase equilibrium data.

$$\alpha_B = \frac{w_B x_A}{(1 - w_B) x_B} \quad (3.80)$$

Small values of α_B imply an equilibrium line close to the lower right corner of the phase diagram and correspondingly strong separation. Values close to one indicate that there is little or no separation. Values above one mean that B is enriched in the solid phase instead of A. Scaling of separation efficiency for solution crystallization is therefore possible through scaling of the relative selectivity α_B .

$$\tilde{\alpha}_B := k_\alpha \alpha_B \quad (3.81)$$

The equilibrium solvent fraction in the liquid is not supposed to change with scaling for a given crystal composition. Therefore,

$$\tilde{x}_A + \tilde{x}_B := x_A + x_B \quad (3.82)$$

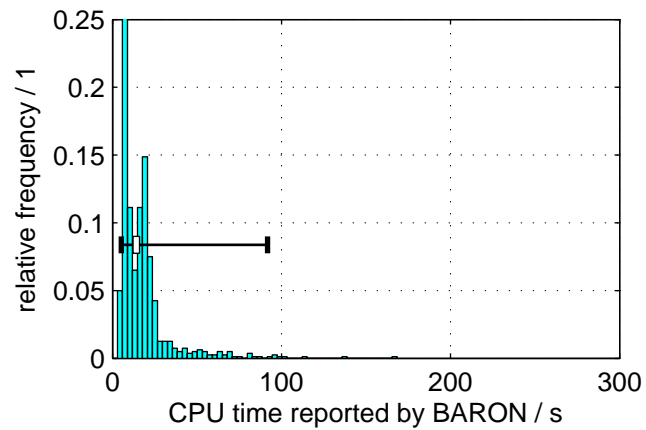
holds for the new mass fractions in the liquid \tilde{x}_A and \tilde{x}_B .

Combining definitions in Equations (3.80)-(3.82), the new equilibrium liquid mass fraction of component A for a given composition of the solid phase is calculated as

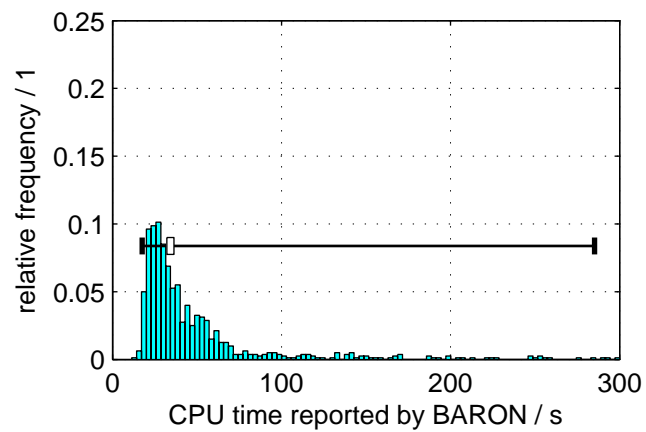
$$\tilde{x}_A \left(\frac{1}{k_\alpha} (1 - x_A - x_S) + x_A \right) = (1 - x_S) x_A. \quad (3.83)$$

The unscaled x_A is substituted by \tilde{x}_A in Equation (3.44) and Equation (3.56). Two according instances of Equation (3.83) are added to the model.

The additional variables and equations required for selectivity scaling may adversely influence computation time. For a scaling factor $k_\alpha = 1$, solutions found by optimizing models with and without scaling are identical, allowing



(a) Model without selectivity scaling.



(b) Model with selectivity scaling.

Figure 3.24: Distribution of CPU time reported by BARON for solving 800 instances of the solution crystallization model with random permutations of equation and variable order and 99% confidence intervals for the median (white box), $P_{0.02275}$ and $P_{0.97725}$ (whiskers) of the true CPU time distribution. Four samples with CPU time more than 300s are outside the axes in (b).

Table 3.5: Parameter values and domain specifications for Figure 3.24.

parameter	value	parameter	value
$(a_{A,0}, a_{A,1})$	(0, 0.1949)	$(a_{A,2}, a_{A,3})$	(-0.2905, 0.2474)
$(a_{S,0}, a_{S,1})$	(0.5149, 0.3131)	$(a_{S,2}, a_{S,3})$	(-0.9066, 0.9268)
F^{InCr}	1 kg s ⁻¹	$z_{\text{A}}^{\text{InCr}}$	0.85
κ	0.01	k_{α}	1
$z_{\text{A,min}}^{\text{Out1Cr}}$	0.99	$z_{\text{A,max}}^{\text{Out2Cr}}$	0.3
n^{Cr}	3		
variable	domain	variable	domain
w	[0, 1]	β	{0, 1}
S, L, V	[0 kg s ⁻¹ , 20 kg s ⁻¹]	\tilde{x}_{A}	[0, 0.1518]
x_{S}	[0.5149, 0.8482]	x_{A}	[0, 0.1518]

direct comparison of different model formulations. Parameters and domain specifications for the computations are given in Table 3.5. The evaporation effort of a countercurrent cascade with three stages is minimized for the original model and the model including selectivity scaling. The according effect on the computational effort for global optimization is shown in Figure 3.24. The computation time for the model with scaling approximately doubles compared to the model without scaling. This is a significant increase but still feasible for parameter studies.

Parameter Studies

Parameter studies are conducted to analyze the influence of key model parameters on globally optimal separation network configurations. Model parameters affecting the optimal configuration of the crystallizer network are the phase equilibrium coefficients, selectivity scaling k_{α} , the proportion of mother liquor adhering to crystals κ , the inlet composition $z_{\text{A}}^{\text{InCr}}$ and the product purity requirements $z_{\text{A,min}}^{\text{Out1Cr}}$ and $z_{\text{A,max}}^{\text{Out2Cr}}$. The focus here is on selectivity scaling and feed composition for comparison with corresponding studies in Section 3.2.4. Mother liquor adhering to crystals and purity requirements are chosen such that low numbers of stages are sufficient for the separation. Physical data for the considered mixture of potassium sulfate (“A”) and ammonium sulfate (“B”)

in water (“S”) at 65 °C is taken from [Münzberg et al., 2016]. The according polynomial coefficients are given in Table 3.6.

Table 3.6: Polynomial fit coefficients for potassium sulfate (“A”) and ammonium sulfate (“B”) in water (“S”) at 65 °C [Münzberg et al., 2016].

parameter	value
$(a_{A,0}, a_{A,1}, a_{A,2}, a_{A,3})$	$(0, 0.1949, -0.2905, 0.2474)$
$(a_{S,0}, a_{S,1}, a_{S,2}, a_{S,3})$	$(0.5149, 0.3131, -0.9066, 0.9268)$

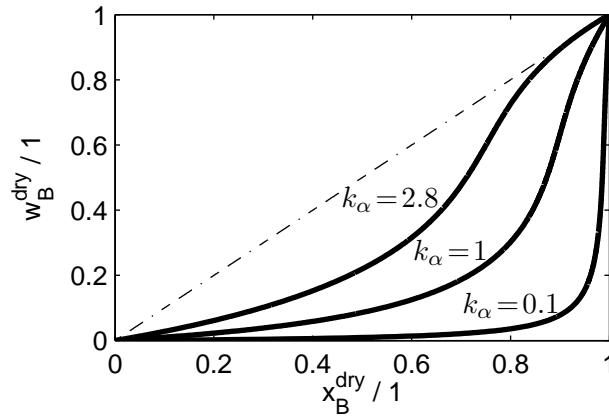


Figure 3.25: Range of scaled selectivity used in parameter study.

The phase equilibrium and its range of variation for the following parameter study is depicted in Figure 3.25. Selectivity varies strongly over the whole concentration range. Note that the equilibrium line crosses the diagonal for selectivity scaling $k_\alpha = 2.8$ and values above, i. e. selectivity reverses for large concentrations of B. In the following parameter studies, appropriate purity requirements are chosen to avoid the region of selectivity reversal and account for the reduced range of feasible compositions.

Parameter values and domain specifications for the parameter studies are given in Table 3.7. Computational effort for solving the solution crystallization model is very high for general configurations with more than three stages, so the number of stages is limited to $n^{\text{Cr}} \leq 3$.

The feed composition is normalized to the product specifications for the fol-

Table 3.7: Parameter values and domain specifications for solution crystallization parameter study.

parameter	value	parameter	value
F^{InCr}	1 kg s^{-1}	$z_{\text{A}}^{\text{InCr}}$	$\{0.35, 0.4, \dots, 0.85\}$
κ	0.01	k_{α}	$\{0.1, 0.2, \dots, 2.8\}$
$z_{\text{A,min}}^{\text{Out1Cr}}$	0.9	$z_{\text{A,max}}^{\text{Out2Cr}}$	0.3
n^{Cr}	$\{1, 2, 3\}$		
variable	domain	variable	domain
w	$[0, 1]$	β	$\{0, 1\}$
S, L, V	$[0 \text{ kg s}^{-1}, 20 \text{ kg s}^{-1}]$	\tilde{x}_{A}	$[0, 0.19]$
x_{S}	$[0.5149, 0.8482]$	x_{A}	$[0, 0.1518]$

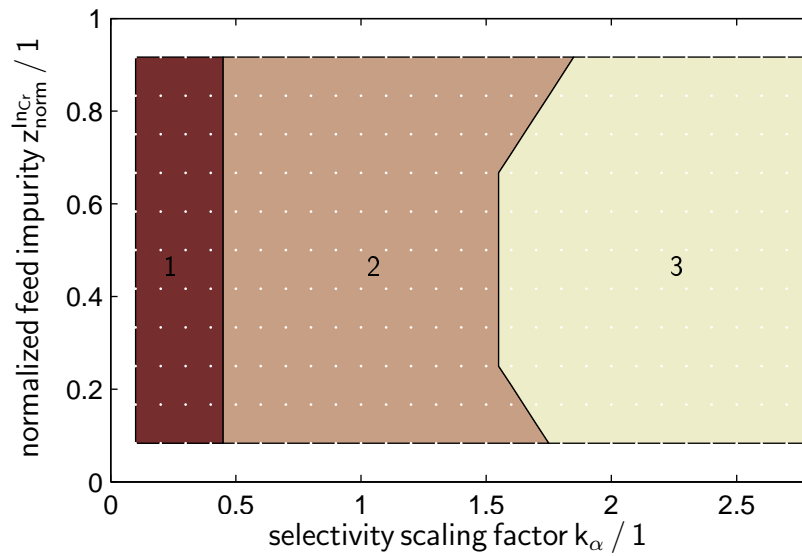
lowing figures according to

$$z_{\text{norm}}^{\text{InCr}} = \frac{z_{\text{A,min}}^{\text{Out1Cr}} - z_{\text{A}}^{\text{InCr}}}{z_{\text{A,min}}^{\text{Out1Cr}} - z_{\text{A,max}}^{\text{Out2Cr}}}. \quad (3.84)$$

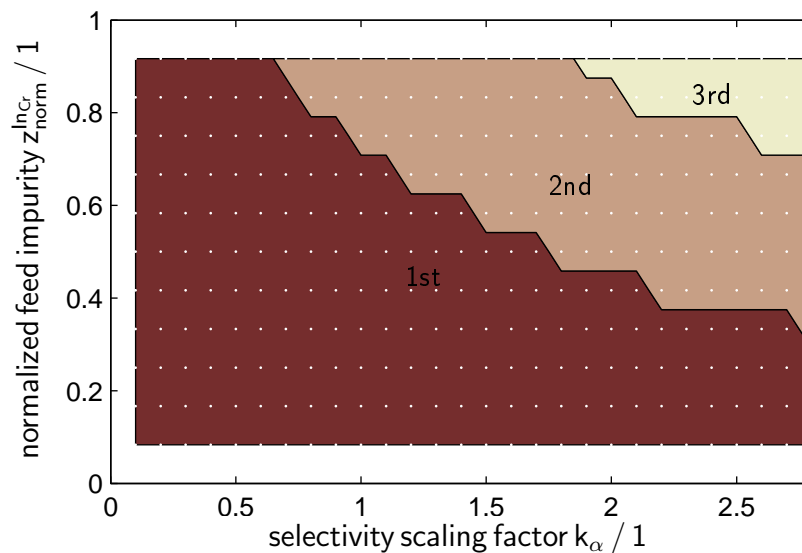
The normalized feed composition is higher for higher concentrations of component B, depleted in the solid phase. The definition of $z_{\text{norm}}^{\text{InCr}}$ is equivalent to the respective definition in Section 3.2.4.

Countercurrent configurations are generated by fixing variables $\beta_{l,l-1}^{\text{S}} = 1$, $l = 2, \dots, n^{\text{Cr}}$, $\beta_{l,l+1}^{\text{L}} = 1$, $l = 1, \dots, n^{\text{Cr}} - 1$, $\beta_1^{\text{S,Out1Cr}} = 1$, $\beta_{n^{\text{Cr}}}^{\text{L,Out2Cr}} = 1$. Figure 3.26 shows parameter regions for globally optimal configurations of countercurrent crystallizer cascades. Increasing the value of k_{α} increases the equilibrium concentration of B in the solid, thus reducing selectivity. Consequently, more stages are needed for the given separation task for higher values of k_{α} . More crystallization steps are required to achieve a given purity if the selectivity is low or the feed impurity is high. Therefore, the optimal feed position is further away from the crystal product for increased values of k_{α} and increased normalized feed impurity. Consequently, the feed stage number is larger in the upper right corner in Figure 3.26b. These results are in accordance with results for multistage melt crystallization in Section 3.2.4.

Results for general crystallizer configurations are depicted in Figure 3.27. Based on results in the previous Section 3.2.4, improved alternative configurations are expected in parameter regions where the optimal feed position



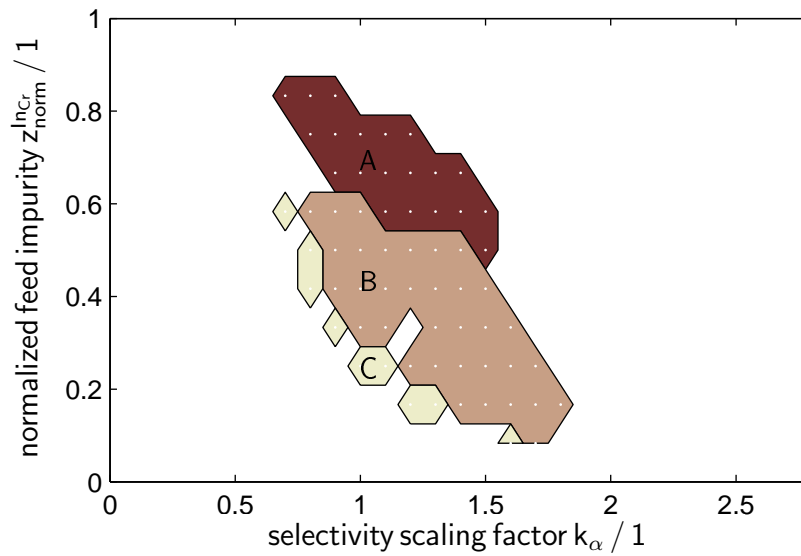
(a) Optimal number of stages.



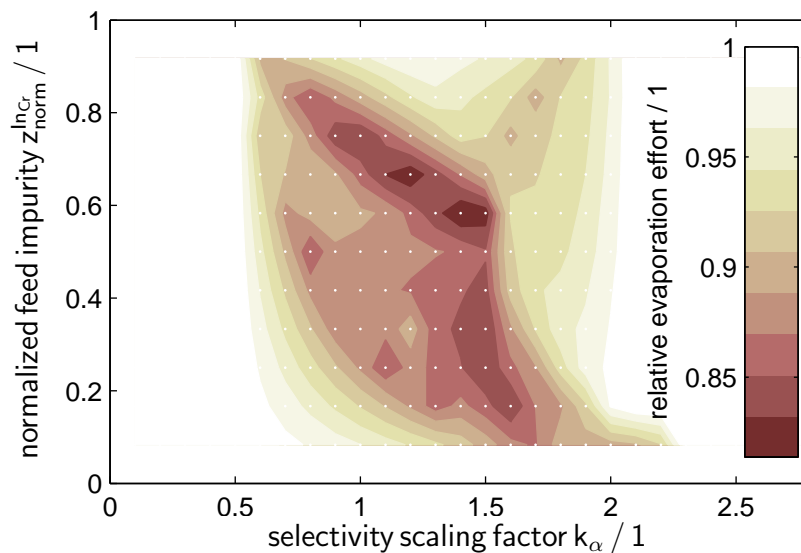
(b) Optimal feed stage position counted from top.

Figure 3.26: Globally optimal countercurrent crystallizer cascade configurations.

switches. This region is also found for the solution crystallization model considered here and marked as region A in Figure 3.27a. Alternative configurations of the type found in region A require one more crystallizer stage than the corresponding optimal countercurrent cascade. Due to alternative configurations being limited to a number of stages $n^{\text{Cr}} \leq 3$ in this study, there is only one



(a) Optimal alternative configurations.



(b) Relative evaporation effort of alternative configurations.

Figure 3.27: (a) Globally optimal configuration of general crystallizer network determined by stage number, feed stage and crystal product transport. Only regions with optimal solutions that have at least 10 % less evaporation effort than the countercurrent cascade are shown. (b) Relative evaporation effort of alternative configurations compared to the countercurrent cascade.

such region, associated with two-stage countercurrent cascades. Parameter regions where optimal countercurrent cascades have three stages are therefore excluded from more detailed considerations.

Region A offers the most improvement of alternative configurations compared to countercurrent cascades. Alternative configurations in region A require as low as 82% of the evaporated solvent that is used by optimal countercurrent cascades. The optimal configurations in region A are depicted in Figure 3.28.

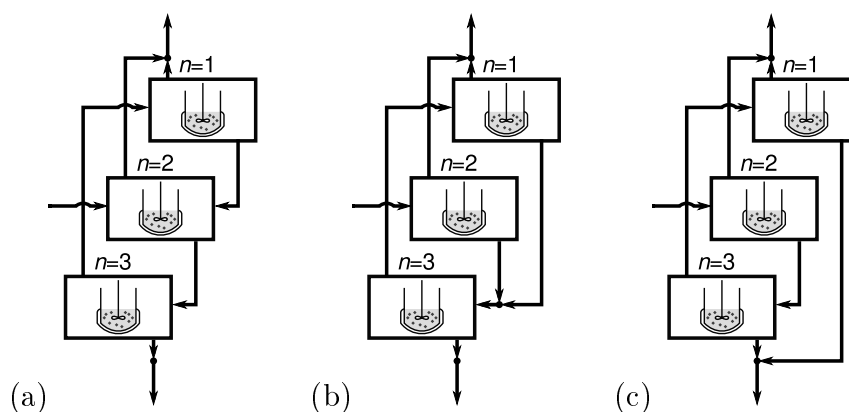


Figure 3.28: Equivalent globally optimal configurations for region A in Figure 3.27.

These are the same configurations as in the corresponding parameter regions discussed in Section 3.2.4. This allows for applying the same strategies to find optimal configurations for melt crystallization also to solution crystallization processes. Configuration (a) in Figure 3.28 is optimal in the entire region A. Configurations (b) and (c) are only equivalent to configuration (a) in parts of region A. Additionally to region A, there are two other parameter regions with significant advantages of alternative configurations over countercurrent cascades. The optimal configurations found in region B and C are depicted in Figure 3.29. Figure 3.29b represents repeated partial solvent evaporation and subsequent removal of crystals from the vessel. That structure is also formed by stages $n = \{1, 2\}$ in configuration Figure 3.29 (a). This type of structure is discussed for melt crystallization in Section 3.2.3 as a redundant configuration equivalent to a single stage. However, for solution crystallization, equilibrium concentrations and therefore separation characteristics in subsequent crystallization steps are shifted by intermediate removal of crystals. In fact, this improves separation efficiency for the mixture considered in this section, as

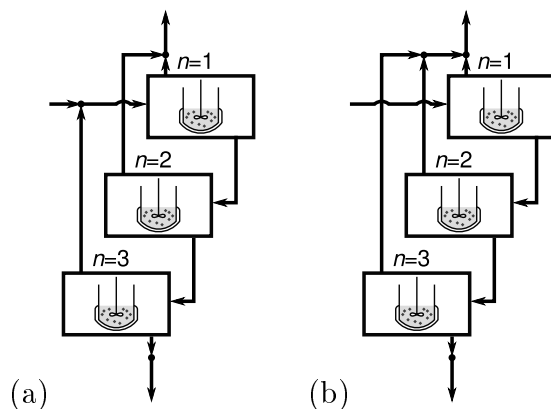


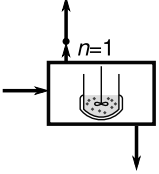
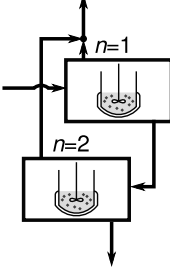
Figure 3.29: Globally optimal configurations for (a) region B and (b) region C in Figure 3.27.

illustrated for a small example in Table 3.8. Table 3.8 compares a single crystallization stage with two stages connected such that the mother liquor of the first stage is the feed of the second stage. For equal overall crystal mass flow and evaporation effort, the two-stage configuration has higher purity products, i. e. the fraction of impurity component B in the overall crystal product is less for the configuration with two stages. Distributing the crystal yield over several stages actually allows separation without recycles in parameter regions where a single stage is not feasible. Given a suitable technique to remove crystals from the solution, this configuration can be implemented as a batch process in a single vessel with continuous evaporation and intermittent crystal removal.

3.3.3 Conclusion

Deterministic global optimization is applied to find the best configuration for multistage solution crystallization. Reductions of evaporation effort over 20 % were observed when using alternative configurations instead of countercurrent cascades. This is lower than the crystallization effort reduction observed for multistage melt crystallization processes in the previous section. However, potential evaporation effort reductions strongly depend on the phase equilibrium and larger reductions are expected when considering different mixtures. The same configurations found for melt crystallization in the previous section are also encountered for solution crystallization in the same parameter

Table 3.8: Comparison of single crystallization unit with two connected units.

single crystallization unit		two connected crystallization units	
			
$S = 0.6 \text{ kg s}^{-1}$		$S_1 = 0.3 \text{ kg s}^{-1}, \quad S_2 = 0.3 \text{ kg s}^{-1}$	
$z_B^{\text{Out1Cr}} = 0.6482$		$z_B^{\text{Out1Cr}} = 0.6297$	
$J_{\text{evap}} = 1.7744$		$J_{\text{evap}} = 1.7744$	
shared parameters			
parameter	value	parameter	value
F^{InCr}	1 kg s^{-1}	z_B^{InCr}	0.75
κ	0.01	k_α	1

regions, allowing for generalization of corresponding design rules. Additionally, repeated crystallization and crystal removal without recycle was found to be an efficient structure in large parameter regions. This structure generates higher purity products than a single crystallization step for solution crystallization, whereas in melt crystallization a single crystallizer stage and repeated crystallization are equivalent. Based on these results, it is recommended to test for both types of configurations in addition to the countercurrent cascade for finding optimal multistage separation networks.

3.4 Filtration

Separating components of a mixture using a semi-permeable membrane is called filtration. A driving force, e.g. a pressure difference between both sides of a membrane, causes permeation through the membrane. The flow of substances with high permeability with regard to that membrane is higher than that of substances with low permeability. Consequently, components with high permeability are concentrated in the permeate and components with low permeability are concentrated in the retentate, see Figure 3.30. Different physical properties can be used to separate or purify products via filtration, e.g. solubility or molecule size. Filtration does not require phase changes to separate components of a mixture and is therefore potentially more efficient than e.g. distillation. Membrane fouling poses a possible disadvantage for filtration processes. An overview on filtration processes is given in [Wijmans and Baker, 1995].

3.4.1 Process Model

Single Units

The model describes permeation through a dense membrane based on the solution-diffusion model described in [Wijmans and Baker, 1995] and used more recently in [Micovic et al., 2014]. The driving force for permeation is a chemical potential difference between both sides of a membrane, which is induced by a pressure difference. The resulting diffusive flow is determined by the permeability of participating substances. Substances with high permeability are enriched in the permeate flow. Large permeabilities result in large permeate flows, while large differences between permeabilities of different species imply high selectivity.

The specific permeate flow j_i according to the solution-diffusion model [Wijmans and Baker, 1995] is

$$j_i = k_{P,i} \left(x_{i,\text{feed}} - x_{i,\text{perm}} \exp\left(-\frac{\nu_i \Delta P}{R T}\right) \right) \quad (3.85)$$

with the molar fraction of component i on the feed side $x_{i,\text{feed}}$ and on the permeate side $x_{i,\text{perm}}$, pressure difference ΔP and temperature T . The parameter

$k_{P,i}$ specifies the permeability of the membrane with regard to component i . It is dependent on the considered species, membrane type, membrane geometry and temperature. The molar volume of a species is denoted as ν_i . For binary mixtures $i=A, B$ as studied in this thesis, component A is considered to have a better permeability compared to B and thus is enriched in the permeate. Component B is considered to be an impurity being enriched in the retentate. In this work, the membrane is assumed to be in contact with a one-dimensional plug-flow feed side according to Figure 3.30. The feed side is assumed to be ideally mixed in directions other than the flow direction. Note that this neglects additional concentration polarization due to a boundary layer at the membrane. The retentate is collected on the feed side at the end of the unit

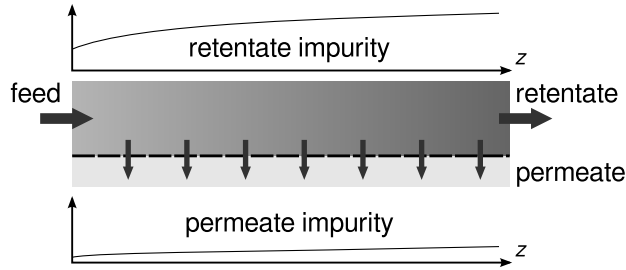


Figure 3.30: Purified permeate flows through a membrane due to a pressure difference, increasing the impurity concentration in the retentate.

and the permeate over the whole length of the membrane. Permeate is removed from the feed stream, so the impurity concentration on the feed side increases from inlet to outlet. Consequently, the permeate impurity concentration also varies over the length of the unit. The overall permeate flow for a filtration unit is calculated by integrating the specific permeate flow j_i over the membrane area A_M in flow direction z .

$$P_i = \int_{A_M} j_i dA = \int_0^{z_M} j_i \frac{\partial A}{\partial z} dz = \frac{\partial A}{\partial z} \int_0^{z_M} j_i dz \quad (3.86)$$

The integral is solved approximately by assuming a linear profile for j_i :

$$\int_0^{z_M} j_i dz \approx (0.5 j_i|^{z=0} + 0.5 j_i|^{z=z_M}) z_M. \quad (3.87)$$

With $A_M = \frac{\partial A}{\partial z} z_M$, the integral permeate flow for each membrane unit $n =$

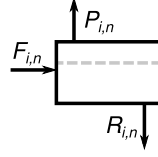


Figure 3.31: Single membrane unit with feed molar flow $F_{i,n}$, permeate molar flow $P_{i,n}$ and retentate molar flow $R_{i,n}$ for components $i = A, B$.

$1, \dots, n^M$ separating a feed molar flow $F_{i,n}$ into a permeate molar flow $P_{i,n}$ and a retentate molar flow $R_{i,n}$ for components $i = A, B$ as in Figure 3.31 is then calculated as

$$P_{i,n} = A_M (0.5 j_{i,n}|^{z=0} + 0.5 j_{i,n}|^{z=z_M}), \quad (3.88)$$

$$j_{i,n}|^{z=0} = k_{P,i} \left(x_{i,n,\text{feed}}|^{z=0} - x_{i,n,\text{perm}}|^{z=0} \exp\left(-\frac{\nu_i \Delta P}{RT}\right) \right), \quad (3.89)$$

$$j_{i,n}|^{z=z_M} = k_{P,i} \left(x_{i,n,\text{feed}}|^{z=z_M} - x_{i,n,\text{perm}}|^{z=z_M} \exp\left(-\frac{\nu_i \Delta P}{RT}\right) \right), \quad (3.90)$$

with the molar fraction of component $i = A, B$ on the feed side $x_{i,\text{feed}}$ and on the permeate side $x_{i,\text{perm}}$ defined by

$$x_{i,n,\text{feed}}|^{z=0} \sum_i F_{i,n} = F_{i,n}, \quad x_{i,n,\text{feed}}|^{z=z_M} \sum_i R_{i,n} = R_{i,n}, \quad (3.91)$$

$$x_{i,n,\text{perm}}|^{z=0} \sum_i j_{i,n}|^{z=0} = j_{i,n}|^{z=0}, \quad x_{i,n,\text{perm}}|^{z=z_M} \sum_i j_{i,n}|^{z=z_M} = j_{i,n}|^{z=z_M}. \quad (3.92)$$

The composition on the feed side at the inlet is equal to that of the overall feed of the membrane unit, and at the outlet it is equal to that of the retentate. Concentration polarization due to a boundary layer at the membrane surface is neglected for this level of modeling detail. The composition at the membrane surface on the permeate side is equal to the permeate composition due to the flow direction being strictly from feed side to permeate side.

The mass balance equation for the whole membrane unit reads

$$R_{i,n} = F_{i,n} - P_{i,n}, \quad i = A, B, \quad n = 1, \dots, n^M. \quad (3.93)$$

The permeation model comprises Equations (3.88)-(3.93). Note that the resulting equation system for calculating the permeate flow is implicit.

Network of Filtration Units

A filtration network with stages $n = 1, \dots, n^M$ numbered downwards is considered. Note that the structure of this network is equivalent to that in Section 3.2. Recall that each stage n separates a feed flow into permeate and retentate. Molar flows of all species $i = A, B$ for feed $F_{i,n}$, permeate $P_{i,n}$ and retentate $R_{i,n}$ are used as variables. According to Section 3.2.4 using molar flows is suitable for global optimization of separation networks. Additionally, $P_{i,n}$ occurs in the following permeation model. Also using it in the separation network model reduces the number of required variables. The feed of each stage $F_{i,n}$ is the sum of all permeate flows P_i and retentate flows R_i connected to that stage and, if applicable for that stage, the membrane network feed flow F^{InM} . The distribution of the feed flow and connections between stages are implemented using binary variables $\beta_n^{\text{InM}} \in \{0, 1\}$, $\beta_{l,n}^{\text{P}} \in \{0, 1\}$ and $\beta_{l,n}^{\text{R}} \in \{0, 1\}$, $n = 1, \dots, n^M$, $l = 1, \dots, n^M$. The variables β_n^{InM} , $\beta_{l,n}^{\text{P}}$ and $\beta_{l,n}^{\text{R}}$ attain a value of one if and only if the feed enters at stage n , the permeate flow of stage l is fed to stage n and the retentate flow of stage l is fed to stage n , respectively. The mass balance equations for each stage $n = 1, \dots, n^M$ then read

$$F_{i,n} = z_i^{\text{InM}} F^{\text{InM}} \beta_n^{\text{InM}} + \sum_{l=1}^{n^M} P_{i,l} \beta_{l,n}^{\text{P}} + \sum_{l=1}^{n^M} R_{i,l} \beta_{l,n}^{\text{R}}, \quad i = A, B \quad (3.94)$$

It is ensured that the feed enters exactly one stage by

$$\sum_{n=1}^{n^M} \beta_n^{\text{InM}} = 1. \quad (3.95)$$

The output flow of each stage is connected to exactly one stage input or one network output by

$$\sum_{n=1}^{n^M} \beta_{l,n}^{\text{P}} + \beta_l^{\text{P,Out1M}} = 1, \quad l = 1, \dots, n^M, \quad (3.96)$$

$$\sum_{n=1}^{n^M} \beta_{l,n}^{\text{R}} + \beta_l^{\text{R,Out2M}} = 1, \quad l = 1, \dots, n^M, \quad (3.97)$$

with $\beta_l^{\text{P,Out1M}} \in \{0, 1\}$ attaining value 1 if and only if the permeate of stage l is connected to output Out1_M and with $\beta_l^{\text{R,Out2M}} \in \{0, 1\}$ attaining value 1 if

and only if the retentate of stage l is connected to output Out2_M .

The product flows are calculated as

$$F_i^{\text{Out1}_M} = \sum_{n=1}^{n^M} \beta_n^{\text{P,Out1}_M} P_{i,n}, \quad i = \text{A, B}, \quad (3.98)$$

$$F_i^{\text{Out2}_M} = \sum_{n=1}^{n^M} \beta_n^{\text{R,Out2}_M} R_{i,n}, \quad i = \text{A, B}. \quad (3.99)$$

The mass balance for the whole separation network reads

$$z_i^{\text{In}_M} F^{\text{In}_M} = F_i^{\text{Out1}_M} + F_i^{\text{Out2}_M}, \quad i = \text{A, B}, \quad (3.100)$$

with total molar flow F^{In_M} and molar fractions $z_i^{\text{In}_M}$ at the inlet and molar flows at the outlets $F_i^{\text{Out1}_M}$ and $F_i^{\text{Out2}_M}$.

The product specifications are given as bounds to molar fractions $z_B^{\text{Out1}_M}$ and $z_B^{\text{Out2}_M}$:

$$\text{up}(z_B^{\text{Out1}_M}) \geq z_B^{\text{Out1}_M} = \frac{F_B^{\text{Out1}_M}}{F_A^{\text{Out1}_M} + F_B^{\text{Out1}_M}}, \quad (3.101)$$

$$\text{lo}(z_B^{\text{Out2}_M}) \leq z_B^{\text{Out2}_M} = \frac{F_B^{\text{Out2}_M}}{F_A^{\text{Out2}_M} + F_B^{\text{Out2}_M}}. \quad (3.102)$$

This is written as linear inequalities

$$(1 - \text{up}(z_B^{\text{Out1}_M})) F_B^{\text{Out1}_M} \leq \text{up}(z_B^{\text{Out1}_M}) F_A^{\text{Out1}_M}, \quad (3.103)$$

$$(1 - \text{lo}(z_B^{\text{Out2}_M})) F_B^{\text{Out2}_M} \geq \text{lo}(z_B^{\text{Out2}_M}) F_A^{\text{Out2}_M}. \quad (3.104)$$

It is assumed that the stages are ordered in terms of feed composition.

$$z_{\text{A},n} \geq z_{\text{A},n+1}, \quad n = 1, \dots, n^M - 1 \quad (3.105)$$

$$z_{\text{B},n} \leq z_{\text{B},n+1}, \quad n = 1, \dots, n^M - 1 \quad (3.106)$$

Permeate gets enriched in one component of a binary mixture and retentate in the other. Therefore, permeate is always transported in one direction of the membrane cascade and retentate in the opposite direction.

$$\beta_{l,n}^{\text{P}} = 0 \quad \text{for all } 1 \leq l \leq n, \quad n = 1, \dots, n^M \quad (3.107)$$

$$\beta_{l,n}^{\text{R}} = 0 \quad \text{for all } n \leq l \leq n^M, \quad n = 1, \dots, n^M \quad (3.108)$$

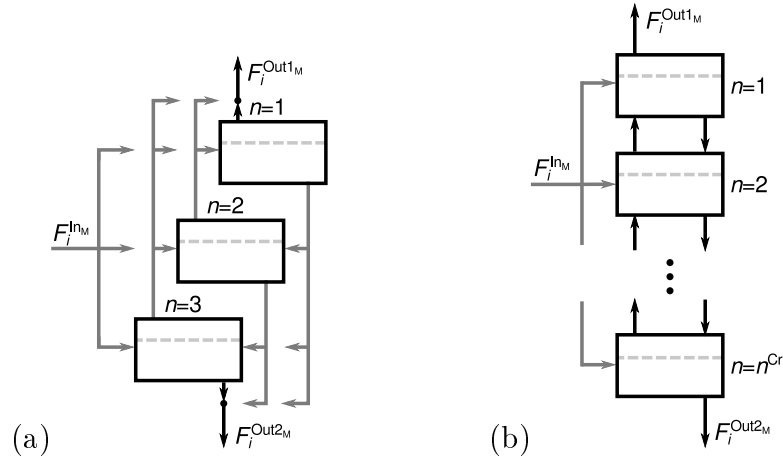


Figure 3.32: (a) Membrane network consisting of $n^M = 3$ stages with arbitrary configuration. (b) Countercurrent membrane cascade with n^M stages and arbitrary feed stage ($\beta_{l,l-1}^P = 1$, $l = 2, \dots, n^M$, $\beta_{l,l+1}^R = 1$, $l = 1, \dots, n^M - 1$, $\beta_1^{P,Out1M} = 1$, $\beta_{n^M}^{R,Out2M} = 1$).

All potential connections within the membrane network used in this work are illustrated in Figure 3.32a for a fixed number of stages $n^M = 3$. The countercurrent cascade depicted in Figure 3.32b will serve as the benchmark for any other configuration within this superstructure.

Following restrictions for molar fractions at the outlets are known.

$$z_B^{InM} < \text{lo}(z_B^{Out2M}) \leq z_B^{Out2M} \leq 1 \quad (3.109)$$

$$0 \leq z_B^{Out1M} \leq \text{up}(z_B^{Out1M}) < z_B^{InM} \quad (3.110)$$

This is used to calculate additional bounds for the molar flows at the outlets based on Equations (3.100)-(3.102).

$$F_A^{Out1M} \geq z_A^{InM} F_A^{InM} - \frac{1 - \text{lo}(z_B^{Out2M})}{\text{lo}(z_B^{Out2M})} F_B^{InM}, \quad (3.111)$$

$$F_A^{Out2M} \leq \frac{1 - \text{lo}(z_B^{Out2M})}{\text{lo}(z_B^{Out2M})} F_B^{InM}, \quad (3.112)$$

$$F_B^{Out2M} \geq z_B^{InM} F_B^{InM} - \frac{\text{up}(z_B^{Out1M})}{1 - \text{up}(z_B^{Out1M})} F_A^{InM}, \quad (3.113)$$

$$F_B^{Out1M} \leq \frac{\text{up}(z_B^{Out1M})}{1 - \text{up}(z_B^{Out1M})} F_A^{InM}. \quad (3.114)$$

The separation network model comprises Equations (3.94)-(3.100) and (3.103)-(3.106). Equations (3.107)-(3.108) and (3.111)-(3.114) are implemented as

bounds to the respective variables.

Objective Function

Both dimension of the unit and energy consumption required for a separation task scale with overall permeate flow. Therefore, the permeation effort, i. e. the ratio of overall permeate flow to feed flow, is used as the objective function that is minimized.

$$J_P = \frac{\sum_{n=1}^{n^M} P_n}{F^{\text{InM}}} \quad (3.115)$$

The permeation effort J_P is analogous to the crystallization effort J_S in Section 3.2, both penalizing the required amount to be processed for a given feed mass. In the following parameter studies, optimization results with regard to these objective functions will be compared.

3.4.2 Computational Studies

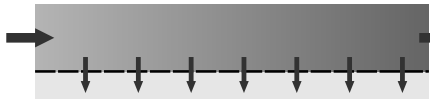
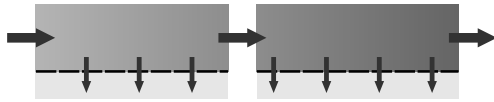
This section deals with computational results based on the multistage filtration model given above.

Redundant configurations

The separation networks considered in this section are analogous to those in Section 3.2 for crystallization. Consequently, the same kinds of redundancies are expected. Additionally, simplifications in Equation 3.87 introduce some unrealistic model behavior. Approximation of the actual concentration profile along the length of the membrane unit leads to the results shown in Table 3.9. A membrane unit operated at a given pressure difference and temperature is arbitrarily split in two units with the same overall area. The retentate of the first unit is fed to the second unit and the permeate of both units is collected as the overall product. If operated at the same pressure difference and temperature, the setup of two units generates the same amount of permeate with the same composition as the single membrane unit does. However, Table 3.9 shows that the numerical results for both setups are different, favoring two membrane units. The single unit has less permeate flow and a higher permeate impurity concentration than two connected units. Approximating the

concentration profile along the membrane underestimates the effective driving force for the separation of the mixture. Implementing the same membrane area with two units allows a closer approximation of the concentration profile and thus a more efficient separation. This undesired numerical effect is treated by defining an offset for rating alternative configurations as better than countercurrent cascades. Alternative configurations with only minor improvements compared to countercurrent cascades are thus removed from the results.

Table 3.9: Comparison of single membrane unit with two connected units.

single membrane unit	two connected membrane units
	
$\Delta P = 35 \cdot 10^5 \text{ Pa}$	
$T = 313.15 \text{ K}$	
$F^{\text{InM}} = 1 \text{ mol s}^{-1}$	
$z_{\text{B}}^{\text{InM}} = 0.05$	
$k_{\text{P,A}} = 0.5411 \text{ mol s}^{-1} \text{ m}^{-2}$, $k_{\text{P,B}} = 0.02104 \text{ mol s}^{-1} \text{ m}^{-2}$	
$\nu_{\text{A}} = 1.95446 \cdot 10^{-4} \text{ m}^3 \text{ mol}^{-1}$, $\nu_{\text{B}} = 4.69981 \cdot 10^{-4} \text{ m}^3 \text{ mol}^{-1}$	
$A = 6 \text{ m}^2$	$A_1 = 3 \text{ m}^2$, $A_2 = 3 \text{ m}^2$
$z_{\text{B}}^{\text{Out1M}} = 0.01454$	$z_{\text{B}}^{\text{Out1M}} = 0.01392$
$F^{\text{Out1M}} = 0.56039 \text{ mol s}^{-1}$	$F^{\text{Out1M}} = 0.56629 \text{ mol s}^{-1}$

Parameter Studies

Parameter studies analogous to those in Section 3.2 are carried out to allow for comparing globally optimal multistage separation processes based on different technologies. A mixture of decane (species A) and hexacosane (species B) is considered with parameter values taken from [Micovic et al., 2014]. Concentrations of hexacosane in the parameter studies below are limited to the same range as in the experiments carried out in [Micovic et al., 2014]. The feed composition and the permeability coefficient of component B are varied for following parameter studies. The feed composition is normalized to the

product specifications according to

$$z_{\text{B,norm}}^{\text{InM}} = \frac{z_{\text{B}}^{\text{InM}} - \text{up}(z_{\text{B}}^{\text{Out1M}})}{\text{lo}(z_{\text{B}}^{\text{Out2M}}) - \text{up}(z_{\text{B}}^{\text{Out1M}})}. \quad (3.116)$$

The permeability coefficient of component B is normalized to a reference value as

$$k_{\text{P,B,norm}} = \frac{k_{\text{P,B}}}{k_{\text{P,B,ref}}}. \quad (3.117)$$

Decreasing this value decreases permeation of component B, thereby increasing selectivity of the desired permeation product A.

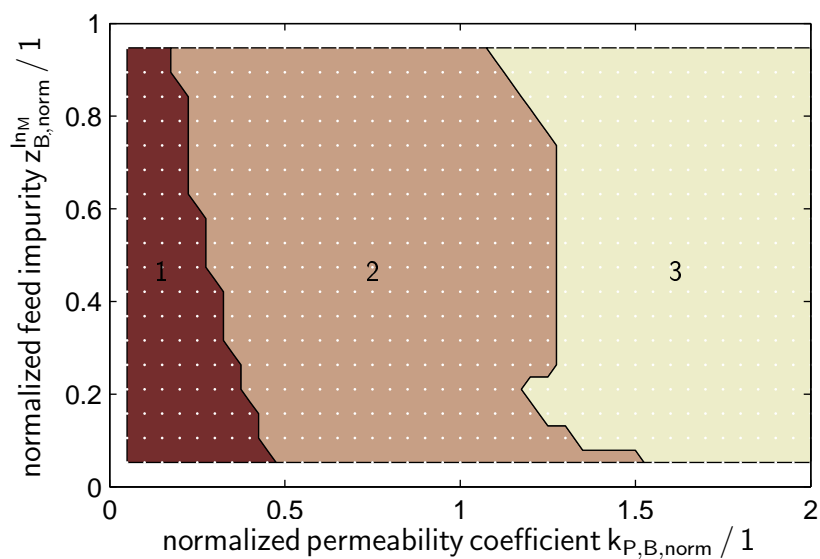
Parameter and domain specifications are given in Table 3.10. Pressure and temperature are fixed to constant values. The membrane area $A_{\text{M},n}$ for each stage n is a decision variable that determines the permeate yield. The remaining decision variables are the binary variables β determining the configuration of the multistage separation network.

Table 3.10: Parameter and domain specifications for multistage membrane parameter studies.

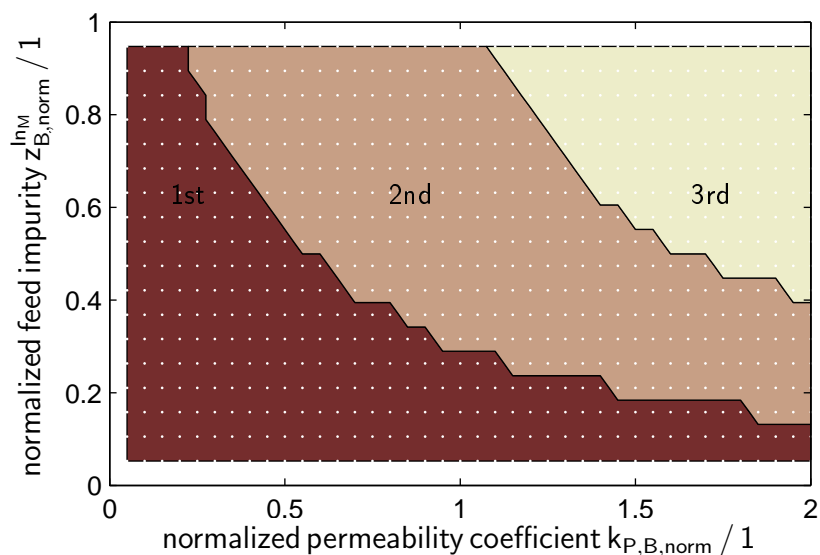
parameter	value	variable	domain
$k_{\text{P,B,norm}}$	$\{0.05, 0.1, \dots, 2\}$	$z_{\text{B}}^{\text{Out1M}}$	$[0, 0.005]$
$z_{\text{B}}^{\text{InM}}$	$\{0.01, 0.015, \dots, 0.095\}$	$z_{\text{B}}^{\text{Out2M}}$	$[0.1, 1]$
n^{M}	$\{1, 2, 3, 4\}$	z	$[0, 1]$
ΔP	$35 \cdot 10^5 \text{ Pa}$	P, R, F	$[0 \text{ mol s}^{-1}, 10 \text{ mol s}^{-1}]$
T	313.15 K	β	$\{0, 1\}$
F^{InM}	1 mol s^{-1}	A_{M}	$[0 \text{ m}^2, 100 \text{ m}^2]$
$k_{\text{P,A}}$	$0.5411 \text{ mol s}^{-1} \text{ m}^{-2*}$	j_i	$[0 \text{ mol s}^{-1} \text{ m}^{-2}, k_{\text{P},i}]$
$k_{\text{P,B,ref}}$	$0.02104 \text{ mol s}^{-1} \text{ m}^{-2*}$		
ν_{A}	$1.95446 \cdot 10^{-4} \text{ m}^3 \text{ mol}^{-1*}$		
ν_{B}	$4.69981 \cdot 10^{-4} \text{ m}^3 \text{ mol}^{-1*}$		

* [Micovic et al., 2014]

Figure 3.33 shows the results for globally optimal countercurrent membrane cascades. The optimal number of stages is depicted in Figure 3.33a and the optimal feed stage position in Figure 3.33b. The optimal number of stages decreases for lower permeability of the impurity component and, to a smaller



(a) Optimal number of stages.



(b) Optimal feed stage position counted from top.

Figure 3.33: Globally optimal countercurrent membrane cascade configurations.

degree, lower feed concentration of impurity. In particular, if the permeability of component B is reduced by 50% - 80% compared to the reference value, one stage instead of two is sufficient for the given separation. The optimal feed stage position is further away from the permeate product outlet Out1 if the impurity concentration in the feed or the impurity permeability is high. Thus,

for impure feed and low desired product selectivity, the feed stage number, counted from top, is higher.

Qualitatively, these are the same results as in Section 3.2 for varying feed composition and selectivity for a melt crystallization process. However, possible generalization of design rules proposed in that section requires the results for general multistage configurations to also be comparable. Figure 3.35 depicts parameter ranges where alternative configurations are better than countercurrent cascades and their relative optimal objective function value. Note that only regions with at least 10% improvement are shown in Figure 3.35a to exclude solutions that are predominantly based on numerical effects as discussed in Section 3.4.2. Regions with improved alternative configurations are located where the optimal feed position for countercurrent cascades switches from one stage to the next. Largest improvements are found where the optimal countercurrent feed position switches from the first stage to the second. In region A in Figure 3.35a, the region with the largest improvements, there are three equivalent optimal configurations. These configurations, depicted in Figure 3.34, are the same as in the corresponding parameter region for multistage crystallization. In summary, this leads to the same design rules as for multistage crystallization. It is sufficient to analyze optimal countercurrent membrane cascades and only search for alternative configurations close to where the optimal feed position changes.

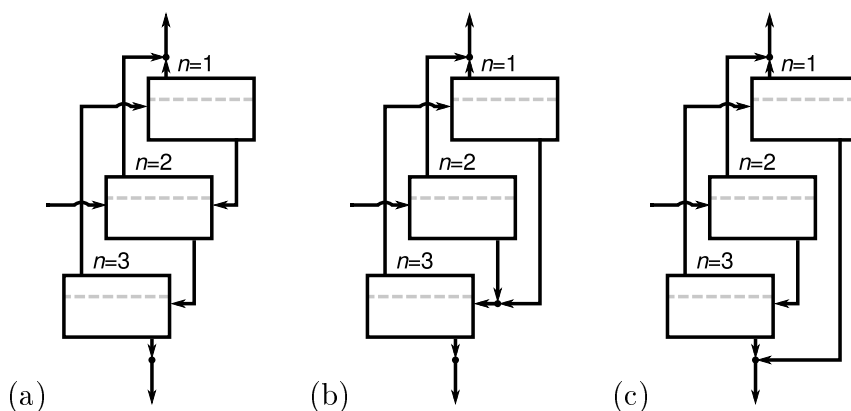
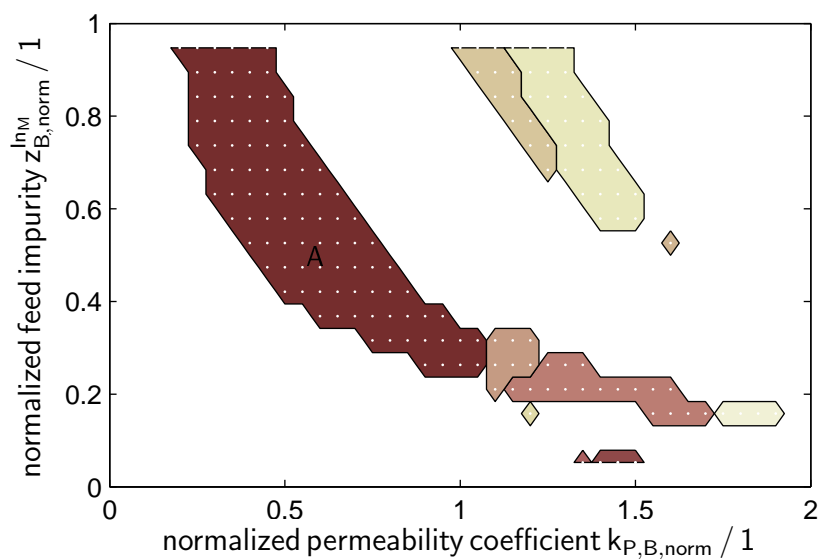
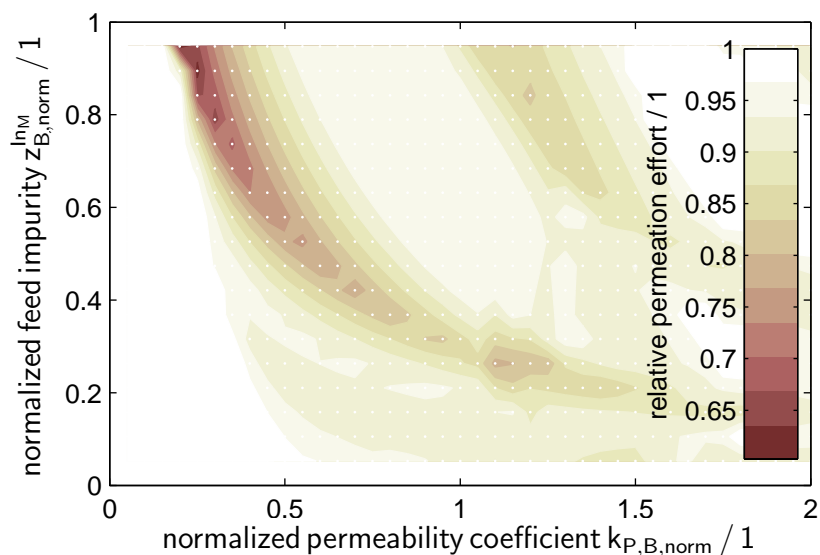


Figure 3.34: Equivalent globally optimal configurations for region A in Figure 3.35.



(a) Parameter regions with optimal alternative configurations.



(b) Relative permeation effort of alternative configurations.

Figure 3.35: (a) Globally optimal configurations of general filtration network determined by stage number, feed stage and permeate transport. Only regions with optimal configurations that use at least 10% less permeate than the countercurrent cascade are shown. (b) Relative permeation effort for alternative configurations compared to the countercurrent cascade.

3.4.3 Conclusion

Deterministic global optimization is applied to find the best configuration for multistage filtration processes. Reductions of evaporation effort over 35% were observed when using alternative configurations instead of countercurrent cascades similar to corresponding values for multistage melt crystallization. The same configurations found for melt crystallization and solution crystallization in the previous sections are also encountered for filtration in the same parameter regions. This allows for generalizing corresponding design rules also to a separation process different from crystallization. Repeated partial filtration, analogous to repeated partial melt crystallization, is supposed to be equivalent to a single filtration step but behaves differently due to model simplifications. According configurations are removed from optimization results. The findings in this and the previous sections shows that only a small set of configurations needs to be tested to determine optimal separation network configurations if the cost is proportional to the amount being processed.

Chapter 4

Flowsheet Selection for Hybrid Distillation/Melt Crystallization Processes

4.1 Introduction

Distillation is the most widely applied unit operation for separation, but it is an inherently energy-intensive process due to the heat required for vaporizing liquid streams [Górak and Sorensen, 2014]. A possible way to reduce energy consumption and cost is by combining distillation with other separation processes such as melt crystallization or filtration, exploiting advantages of each process. One such application is combining high capacity of distillation and high selectivity of melt crystallization for separating close boiling mixtures and azeotropes. These processes already have various industrial applications, see [Franke et al., 2008].

In this chapter, the computational feasibility of globally optimal flowsheet selection for conceptual process design is studied with an exemplary process combining distillation and melt crystallization units. For that goal, suitable models for both unit operations as well as flowsheet and objective function are established. Furthermore, certain properties of the distillation model are discussed and used to further reduce the computational effort for global optimization.

Deterministic global optimization of separating a binary mixture with distillation and melt crystallization was first considered with a simplified model version in [Ballerstein et al., 2014] and extended in [Kunde et al., 2016] to include multistage nonideal crystallization, an improved model formulation for distillation and a more detailed objective function. The discussion is extended here with an analysis of model properties and comparisons with related distillation models from the literature. With respect to [Kunde et al., 2016], process models are updated to better comply with Section 3.2. Although changes are minuscule, according numerical results were recalculated.

4.2 Process Model

In [Müller et al., 2011, Schäfer et al., 2012], a new type of process utilizing thermomorphic solvent systems for the hydroformylation of long-chain olefines based on renewable resources is presented. Among other measures, the reaction product of the process considered there requires the separation of a mixture of

the closely boiling isomers n-dodecanal and 2-methylundecanal, which is exemplary also for a large class of other binary isomeric mixtures. The mixture of n-dodecanal and 2-methylundecanal is zeotropic and close to ideal in the liquid phase and the vapor phase. Due to a relatively low separation factor for closely boiling components, stand-alone distillation may not be economical for this separation task. Therefore, this case study evaluates flowsheet options combining a distillation unit with a second separation process: melt crystallization. The solid-liquid phase diagram of n-dodecanal and 2-methylundecanal resembles the simple eutectic type. Due to the eutectic composition being close to pure 2-methylundecanal, only crystallization of n-dodecanal is practicable. Liquid inclusions and liquid adherent to crystal layers reduce the maximum possible purity achieved in one crystallization step. For more details on the properties of mixtures of n-dodecanal and 2-methylundecanal, see [Beierling and Ruether, 2012, Micovic et al., 2013, Beierling et al., 2013, 2014]. In this chapter, flowsheet selection using a level of modeling detail corresponding to early stages in hierarchical design frameworks is considered. Results obtained by analyzing those models based on mathematical optimization may be adversely affected by poor local solutions. Stochastic or local optimization does not provide a measure to evaluate the quality of local optima and generally can not guarantee to find globally optimal solutions. Therefore, globally optimal solutions obtained with deterministic global optimization software are used for flowsheet selection in this case study. Computational feasibility is achieved by providing suitable model formulations for distillation and melt crystallization. Globally optimal objective function values are used to rate available flowsheet options. In context of hierarchical design frameworks, the flowsheet options with the best rankings are deemed most promising for further study with more detailed process models in subsequent design steps. The following model employs total molar flows and molar flows or molar fractions of 2-methylundecanal as variables. 2-methylundecanal represents the low-boiling component in distillation and the impurity component in crystallization.

It should be noted that in a recent publication [Nallasivam et al., 2016], deterministic global optimization of multicomponent distillation networks is considered for minimum reflux conditions. This restriction to minimum reflux allows using the much less complex Underwood equations for ideal or near-ideal mix-

tures instead of a full tray-to-tray model. Using a tray-to-tray model allows any reflux rate and potentially enables the extension of methods to nonideal separation.

4.2.1 Distillation Column

The separation of isomers n-dodecanal and 2-methylundecanal by distillation is considered. The steady-state distillation model employs the assumption of constant molar overflow due to similar enthalpies of vaporization for n-dodecanal and 2-methylundecanal. This assumption is used instead of implementing a full enthalpy balance. Each stage of the distillation column is assumed to be in thermodynamic equilibrium, which is described sufficiently accurate with constant relative volatilities.

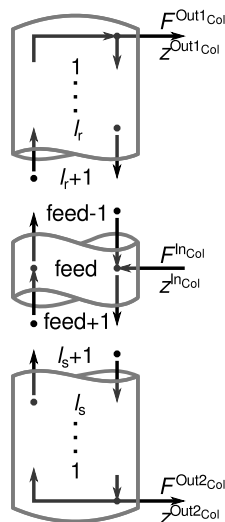


Figure 4.1: Balance envelopes for the distillation column model with rectifying section (top), feed section (middle), and stripping section (bottom). [Reprinted from Kunde et al., 2016, with permission from Elsevier]

The distillation column comprises three sections as illustrated in Figure 4.1. The stages of the stripping section including a total reboiler are labeled downwards by $l_r \in \{1, \dots, l_r^{\max}\}$. The stages of the rectifying section including a total condenser are labeled upwards by $l_s \in \{1, \dots, l_s^{\max}\}$. The distillation column superstructure allows for varying lengths of rectifying and stripping section. The maximum number of stages in the rectifying and stripping section are given by l_r^{\max} and l_s^{\max} , respectively. As explained further below, actual re-

alizations of the superstructure generally have less stages than the maximum number. The feed stage with saturated liquid feed flow is labeled with “feed”. The vapor flow entering the feed stage from the stripping section is labeled with “feed+1” and the liquid flow entering the feed stage from the rectifying section is labeled “feed−1”. The molar fraction of the low-boiling component in internal liquid molar flows is denoted as $x \in [0, 1]$, in internal vapor molar flows V as $y \in [0, 1]$ and in external molar flows F as $z \in [0, 1]$, with molar flows being nonnegative. The distillate is labeled “Out1_{Col}”, the bottoms as “Out2_{Col}” and the feed as “In_{Col}”. The overall material balances for the column then read

$$F^{\text{InCol}} = F^{\text{Out1Col}} + F^{\text{Out2Col}}, \quad \text{and} \quad (4.1)$$

$$F^{\text{InCol}} z^{\text{InCol}} = F^{\text{Out1Col}} z^{\text{Out1Col}} + F^{\text{Out2Col}} z^{\text{Out2Col}}. \quad (4.2)$$

Internal flow ratios $\nu_r = \frac{V - F^{\text{Out1Col}}}{F^{\text{Out1Col}}} \in [0, 1]$ and $\nu_s = \frac{V}{V + F^{\text{Out2Col}}} \in [0, 1]$ are used as variables for internal material balances and implemented as

$$0 = (1 - \nu_r)V - F^{\text{Out1Col}}, \quad 0 = -\nu_s(V + F^{\text{Out2Col}}) + V. \quad (4.3)$$

This allows writing internal material balances entirely without molar flows as

$$y_{l_r+1}^{\text{rect}} = \nu_r x_{l_r}^{\text{rect}} + (1 - \nu_r) z^{\text{Out1Col}}, \quad l_r = 1, \dots, l_r^{\text{max}} - 1, \quad (4.4)$$

$$0 = \nu_s y^{\text{feed+1}} - \nu_s y^{\text{feed}} + \nu_r \nu_s x^{\text{feed-1}} - x^{\text{feed}} + (1 - \nu_r \nu_s) z^{\text{InCol}}, \quad (4.5)$$

$$x_{l_s+1}^{\text{strip}} = \nu_s y_{l_s}^{\text{strip}} + (1 - \nu_s) z^{\text{Out2Col}}, \quad l_s = 1, \dots, l_s^{\text{max}} - 1. \quad (4.6)$$

Note that each set of values for ν_r and ν_s uniquely determines this set of equality conditions. Using internal molar flows instead would allow for different sets of values to result in the same set of equality conditions (see also Equation 4.3), rendering the solution landscape more complex.

The phase equilibrium equations based on constant relative volatilities read

$$(\alpha x_{l_r}^{\text{rect}} + (1 - x_{l_r}^{\text{rect}})) y_{l_r}^{\text{rect}} = \alpha x_{l_r}^{\text{rect}}, \quad l_r = 1, \dots, l_r^{\text{max}}, \quad (4.7)$$

$$(\alpha x^{\text{feed}} + (1 - x^{\text{feed}})) y^{\text{feed}} = \alpha x^{\text{feed}}, \quad (4.8)$$

$$(\alpha x_{l_s}^{\text{strip}} + (1 - x_{l_s}^{\text{strip}})) y_{l_s}^{\text{strip}} = \alpha x_{l_s}^{\text{strip}}, \quad l_s = 1, \dots, l_s^{\text{max}}. \quad (4.9)$$

Due to using the assumption of total reboiler and total condenser, the molar fractions of the low-boiling component in the product outlets z^{Out1Col} and

$z^{\text{Out}2\text{Col}}$ are given as

$$z^{\text{Out}1\text{Col}} = y_1^{\text{rect}}, \quad z^{\text{Out}2\text{Col}} = x_1^{\text{strip}}. \quad (4.10)$$

The column superstructure allows variable lengths of both stripping section and rectifying section. The actual number of active stages is fixed by additional constraints as in [Ballerstein et al., 2014], labeled as *coupling conditions*. As an example, for a rectifying section with length l_r , the coupling conditions enforce equality of the liquid flow leaving the stage with number l_r and the liquid flow entering the feed stage labeled with “feed–1”. The total molar flows are equal due to the assumption of constant molar overflow, reducing the coupling condition to equal molar fractions $x_{l_r}^{\text{rect}} = x^{\text{feed}-1}$. The stripping section is treated analogously to the rectifying section. Binary variables $\beta_{l_r}^{\text{rect}} \in \{0, 1\}$, $l_r = 1, \dots, l_r^{\text{max}}$, and $\beta_{l_s}^{\text{strip}} \in \{0, 1\}$, $l_s = 1, \dots, l_s^{\text{max}}$ are introduced to implement variable lengths of column sections as

$$\begin{aligned} x^{\text{feed}-1} &= \sum_{l_r=1}^{l_r^{\text{max}}} \beta_{l_r}^{\text{rect}} x_{l_r}^{\text{rect}}, & x^{\text{feed}} &= \sum_{l_r=1}^{l_r^{\text{max}}} \beta_{l_r}^{\text{rect}} x_{l_r+1}^{\text{rect}}, \\ y^{\text{feed}+1} &= \sum_{l_s=1}^{l_s^{\text{max}}} \beta_{l_s}^{\text{strip}} y_{l_s}^{\text{strip}}, & x^{\text{feed}} &= \sum_{l_s=1}^{l_s^{\text{max}}} \beta_{l_s}^{\text{strip}} x_{l_s+1}^{\text{strip}}, \end{aligned} \quad (4.11)$$

$$\sum_{l_r=1}^{l_r^{\text{max}}} \beta_{l_r}^{\text{rect}} x_{l_r+1}^{\text{rect}} = \sum_{l_s=1}^{l_s^{\text{max}}} \beta_{l_s}^{\text{strip}} x_{l_s+1}^{\text{strip}}. \quad (4.12)$$

Equation (4.12) is derived by combining Equations (4.11) and is added to the model for improved computational performance.

The number of stages in the rectifying section is fixed to l_r by setting $\beta_{l_r}^{\text{rect}} = 1$ and the number of stages in the stripping section is fixed to l_s by setting $\beta_{l_s}^{\text{strip}} = 1$. The numbers of stages in both sections are uniquely determined by

$$\sum_{l_r=1}^{l_r^{\text{max}}} \beta_{l_r}^{\text{rect}} = 1 \quad \text{and} \quad \sum_{l_s=1}^{l_s^{\text{max}}} \beta_{l_s}^{\text{strip}} = 1. \quad (4.13)$$

The total number of stages in the column l^{Col} including rectifying section, stripping section and feed stage is calculated as

$$l^{\text{Col}} := \sum_{l_r=1}^{l_r^{\text{max}}} \beta_{l_r}^{\text{rect}} l_r + \sum_{l_s=1}^{l_s^{\text{max}}} \beta_{l_s}^{\text{strip}} l_s + 1. \quad (4.14)$$

The distillation model comprises Equation (4.1)-(4.14). In the following section, properties of the distillation model are discussed and used to add further constraints to the model.

4.2.2 Properties of Distillation Model

The molar fraction profile of the low-boiling component in this distillation column model is monotonically increasing from reboiler to condenser. Although this is well-known, there seems to be no mathematically formal proof for this behavior in the literature. Therefore, a proof is given below for the monotonicity of the molar fraction profile of 2-methylundecanal in the stripping section of the distillation column model as introduced in Section 4.2.1. The proof for monotonicity in the rectifying section can be done analogously and is therefore not shown here. Superscripts indicating the stripping section are omitted in this section for better readability.

The mass balance for 2-methylundecanal, Equation (4.6), reads

$$x_{l_s+1} = \nu y(x_{l_s}) + (1 - \nu) x_1 =: f(x_{l_s}),$$

with the vapor molar fraction $y(x_{l_s})$ being a function of the liquid molar fraction x_{l_s} . It will be shown that

$$x_{l_s+1} \geq x_{l_s} \text{ holds for all } l_s = 1, \dots, l_s^{\max} - 1.$$

For this, basic properties of the function for the vapor-liquid-equilibrium $y(x_{l_s})$ are considered first.

Observation 1. *Let $y : [0, 1] \rightarrow [0, 1]$ be defined by $y(x_{l_s}) := \frac{\alpha x_{l_s}}{(\alpha-1)x_{l_s}+1}$, with parameter $\alpha > 1$. Then,*

(a) *y is strictly increasing on $[0, 1]$, and*

(b) *$y(x_{l_s}) \geq x_{l_s}$, for all $x_{l_s} \in [0, 1]$.*

Proof. Statement (a) follows from the fact that the partial derivative

$$\frac{\partial y}{\partial x_{l_s}}(x_{l_s}) = \frac{\alpha}{((\alpha - 1)x_{l_s} + 1)^2} > 0, \quad \text{for all } x_{l_s} \in [0, 1].$$

As $(\alpha - 1)x_{l_s} + 1 > 0$ is satisfied for each $x_{l_s} \in [0, 1]$, the Statement (b) holds if and only if $\alpha x_{l_s} \geq (\alpha - 1)x_{l_s}^2 + x_{l_s}$ holds for all $x_{l_s} \in [0, 1]$. As $\alpha - 1 > 0$, the latter statement is equivalent to $0 \geq x_{l_s}^2 - x_{l_s} = x_{l_s}(x_{l_s} - 1)$ for all $x_{l_s} \in [0, 1]$, which is true. \square

In particular, the proof shows that $y(x_{l_s}) > x_{l_s}$ holds for all $x_{l_s} \in (0, 1)$. Now note that the recursive formula $f(x_{l_s})$ is a linear function in y_{l_s} with non-negative slope ν . As a direct consequence of Observation 1, the following properties of $f(x_{l_s})$ are obtained.

Observation 2. *Let $\nu \in [0, 1]$ and $x_1 \in [0, 1]$ be given. Then, the function*

$$f : [0, 1] \rightarrow \mathbb{R}, x_{l_s} \mapsto f(x_{l_s}) := \nu y(x_{l_s}) + (1 - \nu)x_1$$

satisfies the following properties:

$$(a) \quad f(x_1) \geq x_1,$$

$$(b) \quad f(x_{l_s}) \text{ is monotonically non-decreasing on } [0, 1],$$

$$(c) \quad f(x_{l_s}) \in [0, 1] \text{ holds for all } x_{l_s} \in [0, 1].$$

Proof. Using $y(x_1) \geq x_1$ from Observation 1 leads to $f(x_1) = \nu y(x_1) + (1 - \nu)x_1 \geq \nu x_1 + (1 - \nu)x_1 = x_1$, which proves Statement (a).

Statement (b) follows from Observation 1 as $\frac{\partial f}{\partial x_{l_s}}(x_{l_s}) = \nu \frac{\partial y}{\partial x_{l_s}}(x_{l_s}) \geq 0$.

Statement (c) is true as the value $f(x_{l_s})$ is a convex combination of the number $x_1 \in [0, 1]$ and the number $y(x_{l_s}) \in [0, 1]$. \square

The proof of Statement (b) implies that f is strictly increasing on $[0, 1]$ if $\nu > 0$.

Iteratively applying the results of Observation (2) finally leads to

$$\begin{aligned} x_1 &\leq f(x_1) = x_2 \leq f(x_2) = x_3 \\ &\leq \dots \leq f(x_{l_s^{\max-2}}) = x_{l_s^{\max-1}} \leq f(x_{l_s^{\max-1}}) = x_{l_s^{\max}}. \end{aligned}$$

Note that the properties discussed above are given implicitly by the model equations, but are not necessarily recognized or exploited by general optimization algorithms. Therefore, corresponding explicit constraints are added to the model to improve the convergence rate of branch-and-bound algorithms.

Based on the monotonicity of molar fraction profiles, following constraints are added to the distillation model.

$$x_{l_s}^{\text{strip}} \geq x_{l_s-1}^{\text{strip}}, \quad y_{l_s}^{\text{strip}} \geq y_{l_s-1}^{\text{strip}}, \quad l_s = 2, \dots, l_s^{\text{max}} \quad (4.15)$$

$$x_{l_r}^{\text{rect}} \leq x_{l_r-1}^{\text{rect}}, \quad y_{l_r}^{\text{rect}} \leq y_{l_r-1}^{\text{rect}}, \quad l_r = 2, \dots, l_r^{\text{max}} \quad (4.16)$$

Molar fractions in consecutive stages of the rectifying and stripping section are calculated by the recursion formulas defined in Equation (4.4) and Equation (4.6). Due to monotonicity, the fixed points $y_*^{\text{rect}}, x_*^{\text{rect}}, y_*^{\text{strip}}, x_*^{\text{strip}} \in [0, 1]$ of that recursion are bounds to the molar fractions on each stage. The definitions of the fixed points are added to the model as Equation (4.17) and Equation (4.18).

$$x_*^{\text{strip}} = \nu_s y_*^{\text{strip}} + (1 - \nu_s) z^{\text{Out2Col}}, \quad (4.17)$$

$$(\alpha x_*^{\text{strip}} + (1 - x_*^{\text{strip}})) y_*^{\text{strip}} = \alpha x_*^{\text{strip}},$$

$$y_*^{\text{rect}} = \nu_r x_*^{\text{rect}} + (1 - \nu_r) z^{\text{Out1Col}}, \quad (4.18)$$

$$(\alpha x_*^{\text{rect}} + (1 - x_*^{\text{rect}})) y_*^{\text{rect}} = \alpha x_*^{\text{rect}}.$$

The fixed points are used in the following constraints to implement bounds to molar fractions in each column section.

$$x_{l_s}^{\text{strip}} \leq x_*^{\text{strip}}, \quad y_{l_s}^{\text{strip}} \leq y_*^{\text{strip}}, \quad l_s = 1, \dots, l_s^{\text{max}} \quad (4.19)$$

$$x_{l_s}^{\text{rect}} \geq x_*^{\text{rect}}, \quad y_{l_s}^{\text{rect}} \geq y_*^{\text{rect}}, \quad l_s = 1, \dots, l_s^{\text{max}} \quad (4.20)$$

Recall that the coupling conditions in Equation (4.11)-(4.12) ensure that molar fractions in different sections associated with each other are equal. Therefore, feasible ranges for molar fractions in rectifying and stripping section are required to overlap, leading to

$$x_*^{\text{rect}} \leq x_*^{\text{strip}}, \quad y_*^{\text{rect}} \leq y_*^{\text{strip}}. \quad (4.21)$$

The distillation model defined in Section 4.2.1 is expanded by Equations (4.15)-(4.21).

Note that in [Ballerstein et al., 2014] and [Mertens et al., 2016], the recursion formulas in Equation (4.4) and Equation (4.6) are used to propagate bounds on molar fractions from one stage to the next, starting from the outlets. This leads to regions comprising all possible molar fraction profiles in the column

sections as well as possible feed stage positions as illustrated in Figure 4.2. Monotonicity of molar fraction profiles, as discussed above, is one of the key requirements for this bound propagation. The technique is used to reduce the domain in each node of a branch-and-bound algorithm, significantly reducing computational effort. However, this technique requires alteration of the optimization algorithm itself, which is outside the scope of this work.

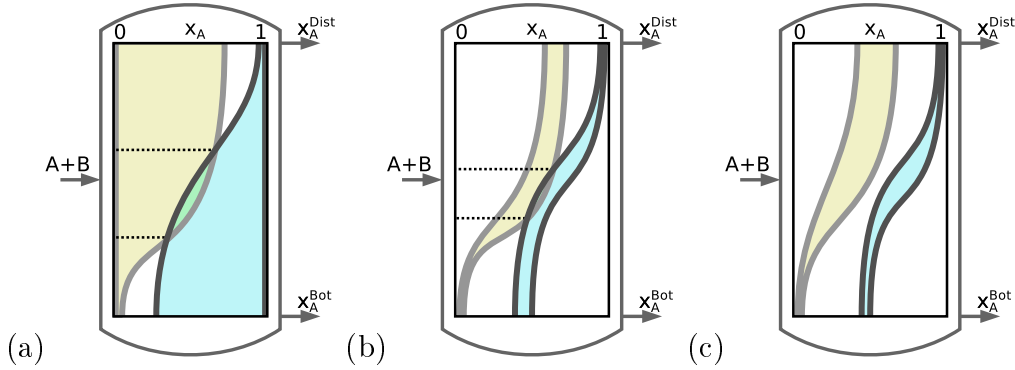


Figure 4.2: Regions of all possible molar fraction profiles and feed stage positions for (a) loose bounds on outlet molar fractions, (b) tighter bounds and (c) infeasible conditions.

Remark on Non-Ideal Phase Equilibria Monotonicity in binary distillation columns also holds for general functions y , provided that all properties of Observations (1) and (2) are valid in $[x^{\text{lo}}, x^{\text{up}}]$, $0 \leq x^{\text{lo}} < x^{\text{up}} \leq 1$ and $x_1 \in [x^{\text{lo}}, x^{\text{up}}]$. This allows for applying monotonicity-based techniques for a large range of binary mixtures. In particular, this also includes binary azeotropic mixtures.

Remarks on Multicomponent Mixtures Monotonicity of molar fraction profiles in distillation columns does not hold in general for multicomponent mixtures. However, for ideal phase equilibria, monotonicity holds for pseudo-components \tilde{x} and \tilde{y} defined as

$$\tilde{x}_{j,n} = \sum_{i=1}^j x_{i,n}, \quad \tilde{y}_{j,n} = \sum_{i=1}^j y_{i,n}, \quad j = 1, \dots, N_C - 1, \quad (4.22)$$

with N_C being the number of components in the mixture.

Given mass balances for the stripping section of a distillation column

$$x_{i,l_s+1}^{\text{strip}} = \nu_s y_{i,l_s}^{\text{strip}} + (1 - \nu_s) z_i^{\text{Out2Col}}, \quad y_{i,1}^{\text{strip}} = z_i^{\text{Out2Col}}, \quad (4.23)$$

and an ideal phase equilibrium with relative volatilities $\alpha_1 > \alpha_2 > \dots > \alpha_{N_C} = 1$

$$\left(\sum_{i=1}^{N_C-1} (\alpha_i - 1) x_{i,l_s}^{\text{strip}} + 1 \right) y_{i,l_s}^{\text{strip}} = \alpha_i x_{i,l_s}^{\text{strip}} \quad (4.24)$$

for all $l_s = 1, \dots, l_s^{\text{max}} - 1$ and $j = 1, \dots, N_C - 1$, it is shown in [Mertens et al., 2016] that

$$\tilde{x}_{j,l_s+1}^{\text{strip}} \geq \tilde{x}_{j,l_s}^{\text{strip}} \quad \text{holds for all } l_s = 1, \dots, l_s^{\text{max}} - 1, \quad j = 1, \dots, N_C - 1. \quad (4.25)$$

Note that this also implies monotonicity in the rectifying section. Consequently, the bound tightening technique developed in [Ballerstein et al., 2014] for binary mixtures is extended in [Mertens et al., 2016] to ideal multicomponent mixtures.

However, monotonicity is actually not necessary for the bound tightening technique, but rather

$$\tilde{x}_{j,l_s}^{\text{strip}} \geq \tilde{x}_{j,1}^{\text{strip}} \quad \text{holds for all } l_s = 2, \dots, l_s^{\text{max}}, \quad j = 1, \dots, N_C - 1, \quad (4.26)$$

which is true for general phase equilibria with

$$\tilde{y}_{j,l_s}^{\text{strip}} \geq \tilde{x}_{j,l_s}^{\text{strip}}. \quad (4.27)$$

This allows for extending the bound tightening strategy from [Ballerstein et al., 2014] to non-ideal mixtures with according properties. The proof for Equation (4.26) is given in Appendix B.

4.2.3 Countercurrent Crystallizer Cascade

This section describes a crystallization process for the separation of n-dodecanal and 2-methylundecanal. The solid-liquid equilibrium of the considered mixture is of the simple eutectic type. The eutectic point is close to pure 2-methylundecanal. Therefore, only crystallization of n-dodecanal with impurities of 2-methylundecanal is considered. Crystal product impurities are described by a constant differential distribution coefficient as in [Wellinghoff and

Wintermantel, 1991, Micovic et al., 2013]. The according experimental data is published in [Micovic et al., 2013] and [Beierling and Ruether, 2012]. Based on the conditions outlined above, the model presented in Section 3.2 is applied in this section as well. The configuration is fixed to a countercurrent cascade with two stages, depicted in Figure 4.3.

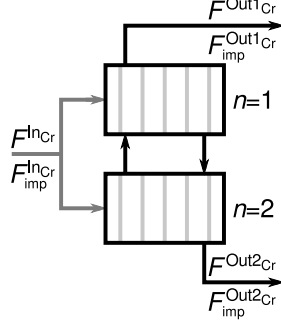


Figure 4.3: Countercurrent two-stage crystallizer with arbitrary feed stage. Molten crystal product is transported upwards. Liquid remainder is transported downwards. [Reprinted from Kunde et al., 2016, with permission from Elsevier]

Mass balances for the input of each stage read

$$F_1 = F^{\text{InCr}} \beta_1^{\text{InCr}} + S_2 \quad (4.28)$$

$$F_{\text{imp},1} = F_{\text{imp}}^{\text{InCr}} \beta_1^{\text{InCr}} + S_{\text{imp},2} \quad (4.29)$$

$$F_2 = F^{\text{InCr}} \beta_2^{\text{InCr}} + L_1 \quad (4.30)$$

$$F_{\text{imp},2} = F_{\text{imp}}^{\text{InCr}} \beta_2^{\text{InCr}} + L_{\text{imp},1}, \quad (4.31)$$

with the feed stage being determined by binary variables $\beta_1^{\text{InCr}}, \beta_2^{\text{InCr}} \in \{0, 1\}$. The following constraint ensures that exactly one of the stages is appointed as feed stage.

$$\beta_1^{\text{InCr}} + \beta_2^{\text{InCr}} = 1 \quad (4.32)$$

Model equations describing separation by melt crystallization read for each stage $n = 1, 2$:

$$\begin{aligned} L_{\text{imp},n} &= \tilde{Y}_n^{k_{\text{diff}}} F_{\text{imp},n}, & S_{\text{imp},n} &= F_{\text{imp},n} - L_{\text{imp},n}, \\ L_n &= \tilde{Y} F_n, & S_n &= F_n - L_n. \end{aligned} \quad (4.33)$$

Output flows of the crystallizer unit are defined as

$$F^{\text{Out1Cr}} = S_1, \quad F_{\text{imp}}^{\text{Out1Cr}} = S_{\text{imp},1}, \quad (4.34)$$

$$F^{\text{Out2Cr}} = L_2, \quad F_{\text{imp}}^{\text{Out2Cr}} = L_{\text{imp},2}. \quad (4.35)$$

Molar fractions of impurity in the liquid remainder are constrained to values below its eutectic value x^{eut} due to eutectic-type solid-liquid phase behavior. Practical limitations to the minimum cooling temperature may further restrict feasible values for the molar fraction of 2-methylundecanal. For simple eutectic-type solid-liquid phase behavior, each equilibrium temperature corresponds to a uniquely determined equilibrium composition on each side of the eutectic point. Therefore it is sufficient to determine a maximum molar fraction of 2-methylundecanal $x_{\text{imp}}^{\text{max}}$ to cover both eutectic point and temperature limitations, whichever is more restrictive. Physical data of 2-methylundecanal and n-dodecanal from [Micovic et al., 2013] is used here. The constraint is implemented as

$$x_{\text{imp}}^{\text{max}} L_n \geq L_{\text{imp},n}, \quad n = 1, 2. \quad (4.36)$$

4.2.4 Flowsheet Options

A straight-forward approach is used to generate flowsheet options for this case study. More complex process engineering tasks may require a systematic generation of flowsheet options as covered by the literature [e.g., Holtbruegge et al., 2014, Quaglia et al., 2015].

Flowsheets comprising up to two melt crystallization units and one distillation column are considered. Distillation is capable of separating the binary mixture of n-dodecanal and 2-methylundecanal into pure substances, while crystallization is practically only suitable to produce pure n-dodecanal due to the position of the eutectic point, thus reducing the number of feasible flowsheets. Further flowsheet options are excluded by forbidding streams previously enriched in n-dodecanal from mixing with those enriched in 2-methylundecanal. Each flow is directed to exactly one unit or alternatively collected as one of the two overall product flows, stream splitting is not considered. The resulting six flowsheets are listed in Figure 4.4, with the mixture feed flow labeled as “N,iso”, product concentrated in n-dodecanal labeled as “N” and product concentrated in 2-methylundecanal labeled as “iso”. Model parameters and specifications of the separation task determine the feasibility and optimality of those remaining flowsheets, which will be identified using deterministic global optimization.

Note that flowsheet candidates for this process are also studied in [Micovic

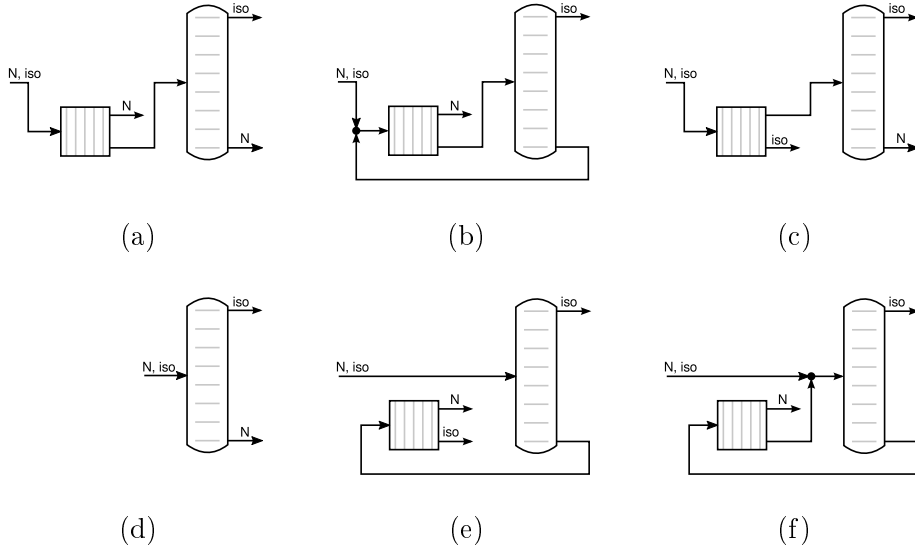


Figure 4.4: Flowsheet options. The square symbol represents a countercurrent crystallizer cascade with two stages and arbitrary feed stage. Unit outlets assigned with “N” are collected at product outlet “Out1_{sys}” and unit outlets assigned with “iso” are collected at product outlet “Out2_{sys}”. [Reprinted from Kunde et al., 2016, with permission from Elsevier]

et al., 2013] using stochastic optimization. However, flowsheet option (b) in Figure 4.4 is not included there. The following mass balances are added to model the different flowsheet options, with system feed inlet “In_{sys}” and system product outlets “Out1_{sys}” and “Out2_{sys}”.

$$F^{\text{InCr}} = F^{\text{Insys}} \beta_{\text{sys}}^{\text{Cr}} + F^{\text{Out2Col}} \beta_{\text{Col2}}^{\text{Cr}} \quad (4.37)$$

$$F_{\text{imp}}^{\text{InCr}} = z^{\text{Insys}} F^{\text{Insys}} \beta_{\text{sys}}^{\text{Cr}} + z^{\text{Out2Col}} F^{\text{Out2Col}} \beta_{\text{Col2}}^{\text{Cr}} \quad (4.38)$$

$$F^{\text{InCol}} = F^{\text{Insys}} \beta_{\text{sys}}^{\text{Col}} + F^{\text{Out1Cr}} \beta_{\text{Cr1}}^{\text{Col}} + F^{\text{Out2Cr}} \beta_{\text{Cr2}}^{\text{Col}} \quad (4.39)$$

$$z^{\text{InCol}} F^{\text{InCol}} = z^{\text{Insys}} F^{\text{Insys}} \beta_{\text{sys}}^{\text{Col}} + F_{\text{imp}}^{\text{Out1Cr}} \beta_{\text{Cr1}}^{\text{Col}} + F_{\text{imp}}^{\text{Out2Cr}} \beta_{\text{Cr2}}^{\text{Col}} \quad (4.40)$$

$$F^{\text{Out1sys}} = F^{\text{Out1Col}} + F^{\text{Out2Cr}} \beta_{\text{Cr2}}^{\text{sys1}} \quad (4.41)$$

$$z^{\text{Out1sys}} F^{\text{Out1sys}} = z^{\text{Out1Col}} F^{\text{Out1Col}} + F_{\text{imp}}^{\text{Out2Cr}} \beta_{\text{Cr2}}^{\text{sys1}} \quad (4.42)$$

$$F^{\text{Out2sys}} = F^{\text{Out2Col}} \beta_{\text{Col2}}^{\text{sys2}} + F^{\text{Out1Cr}} \beta_{\text{Cr1}}^{\text{sys2}} \quad (4.43)$$

$$z^{\text{Out2sys}} F^{\text{Out2sys}} = z^{\text{Out2Col}} F^{\text{Out2Col}} \beta_{\text{Col2}}^{\text{sys2}} + F_{\text{imp}}^{\text{Out1Cr}} \beta_{\text{Cr1}}^{\text{sys2}} \quad (4.44)$$

Binary parameters β are used to fix different flowsheet variants. Parameter values for according flowsheet options are given in Table 4.1.

Table 4.1: Parameter values defining flowsheet options in Figure 4.4.

flowsheet option	$\beta_{\text{sys}}^{\text{Cr}}$	$\beta_{\text{sys}}^{\text{Col}}$	$\beta_{\text{Cr1}}^{\text{Col}}$	$\beta_{\text{Cr1}}^{\text{sys2}}$	$\beta_{\text{Cr2}}^{\text{Col}}$	$\beta_{\text{Cr2}}^{\text{sys1}}$	$\beta_{\text{Col2}}^{\text{sys2}}$	$\beta_{\text{Col2}}^{\text{Cr}}$
(a)	1	0	0	1	1	0	1	0
(b)	1	0	0	1	1	0	0	1
(c)	1	0	1	0	0	1	1	0
(d)	0	1	0	0	0	0	1	0
(e)	0	1	0	1	0	1	0	1
(f)	0	1	0	1	1	0	0	1

Each feasible process variant needs to satisfy product purity requirements, which is implemented by setting an upper bound to z^{Out1sys} and a lower bound to z^{Out2sys} . In addition to the equations above, an overall mass balance for the entire separation network is included in the model as follows.

$$z^{\text{Insys}} F^{\text{Insys}} = z^{\text{Out1sys}} F^{\text{Out1sys}} + z^{\text{Out2sys}} F^{\text{Out2sys}} \quad (4.45)$$

4.2.5 Objective Function

An economic objective function adopted from [Micovic et al., 2013, Franke et al., 2004, 2008] and used in [Kunde et al., 2016] is also used here to evaluate the different flowsheet options. The main features of the cost model, which is mostly based on estimations from [Douglas, 1988], are described below. The original publications are referred to for more details on the cost model.

Total annual costs (TAC) of the process are used as the objective function. The objective function comprises operating costs and annualized investment costs for both the distillation column and the melt crystallization units. Calculating the contributions of shell and packings of the distillation column to the investment costs requires knowledge of the column diameter. The flooding point model from [Maćkowiak, 2010] is adapted here to estimate the column diameter. Approximating the required column cross section area for 80% of the critical vapor flow velocity as a linear function of liquid and vapor molar flows assuming constant physical properties leads to a sufficiently accurate estimation with low computational effort. Of course, this measure also implies that coefficients in the cost model need to be adjusted accordingly for different case studies. Providing heat through steam for the desired vapor flow and

cooling water for heat removal at the condenser determine the operating costs of the distillation column. The crystallizer units require a heat exchanger as well as a storage tank for each stage as investments. The equipment size is designed for crystallization in a single vessel and using tanks for intermediate storage to enable multistage operation. The capacity of the storage tanks is the same as the maximum capacity of the crystallizer. The cooling required for producing a desired amount of crystal is used to calculate the operating costs for the crystallizer units according to [Wellinghoff and Wintermantel, 1991]. The cost model employed in this work contains many parameters specific to the design task of the considered case study, reducing comparability to other design tasks. However, computational feasibility as one of the main topics of this case study requires first and foremost reproducible computational results. Therefore, the complete objective function written in the condensed form that was used for implementation is provided below.

$$\begin{aligned}
J_{\text{TAC}} = & \\
& (\quad 17544 V \text{ s mol}^{-1} \\
& +2364.5 (0.2 l^{\text{Col}} + 4)^{0.82} (0.2378 V \text{ s mol}^{-1} + 0.0221 F^{\text{Out2Col}} \text{ s mol}^{-1})^{0.533} \\
& +2009.7 l^{\text{Col}} (0.2378 V \text{ s mol}^{-1} + 0.0221 F^{\text{Out2Col}} \text{ s mol}^{-1}) \\
& -171.4 l^{\text{Col}} (0.2378 V \text{ s mol}^{-1} + 0.0221 F^{\text{Out2Col}} \text{ s mol}^{-1})^{0.5} \\
& +173.6 l^{\text{Col}} + 42030 \left(\sum_{n=1}^{n^{\text{Cr}}} S_n \text{ s mol}^{-1} \right)^{0.65} + n^{\text{Cr}} 3186.8 \left(\sum_{n=1}^{n^{\text{Cr}}} S_n \text{ s mol}^{-1} \right)^{0.32} \\
& +23465 \sum_{n=1}^{n^{\text{Cr}}} S_n \text{ s mol}^{-1} \quad) \in \text{a}^{-1}
\end{aligned} \tag{4.46}$$

4.3 Computational Results

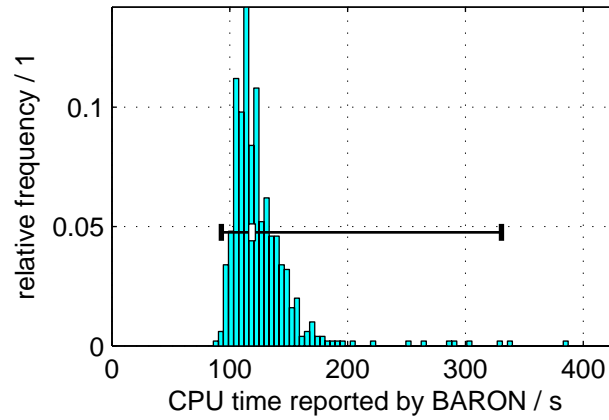
This section deals with computational results for the flowsheet selection problem defined above. First, the effect on computational performance of adding redundant equations to the model is evaluated. The computationally more efficient model formulation is then used to calculate optimal cost values for each flowsheet option.

4.3.1 Effect of Monotonicity Constraints on Computation Time

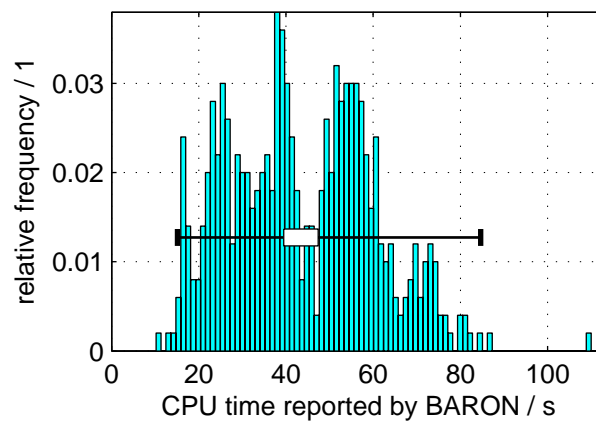
Additional constraints may be used by a solver to more efficiently reduce the search space during optimization, but they also increase model size. The effect of including redundant constraints on the computation time for solving the distillation column model is evaluated in this section. The distillation model in Section 4.2.1 is solved with regard to objective function Equation (4.46) with and without the monotonicity constraints developed in Section 4.2.2. Product purity constraints are applied directly to the column outlets compositions z^{Out1Col} and z^{Out2Col} . Results are obtained by using BARON 15.9.22 (GAMS 24.6.1, Linux, x64). CPLEX 12.6.3 and CONOPT 3.17A are facilitated as subsolvers for BARON. The solver options are left at default values except for the BARON option “NumLoc 0” and the termination condition “optcr”, the relative difference between upper and lower bound, which was set to 0.0001. The processes are run consecutively in a virtual Linux environment on a standard desktop computer (Intel® Core™ i5-6500 @ 3.20 GHz). The memory allocated to each process is 2048 MB. Global solutions as calculated beforehand by the solver are provided as initial solutions. This reduces the task of the solver to proving global optimality of the initial solution and thus removes searching for good local solutions as an influence on computation time. Parameter and domain specifications are given in Table 4.2, the resulting computation time is depicted in Figure 4.5. Including the monotonicity constraints Equations (4.15)-(4.21) leads to a reduction of the median computation time for solving the optimization problem from over 100 s to less than 50 s. Therefore, monotonicity constraints are also used in the following calculations.

Table 4.2: Monotonicity constraints: Parameter and domain specifications for computation time comparison.

parameter	value	variable	domain	variable	domain
F^{InSys}	1 mol s^{-1}	l^{Col}	$[3, 50]$	V	$[0 \text{ mol s}^{-1}, 20 \text{ mol s}^{-1}]$
z^{InSys}	0.1	z^{Out2Col}	$[0, 0.01]$	F	$[0 \text{ mol s}^{-1}, 1 \text{ mol s}^{-1}]$
$l_{\text{r}}^{\text{max}}$	50	z^{Out1Col}	$[0.99, 1]$	β	$\{0, 1\}$
$l_{\text{s}}^{\text{max}}$	50	x, y, ν	$[0, 1]$		



(a) Distillation column model without monotonicity constraints.



(b) Distillation column model with monotonicity constraints.

Figure 4.5: Distribution of CPU time reported by BARON for solving 500 instances of the distillation column model with random permutations of equation and variable order and 99 % confidence intervals for the median (white box), $P_{0.02275}$ and $P_{0.97725}$ (whiskers) of the true CPU time distribution.

4.3.2 Comparison of Mixed-Integer Design Models

There are numerous ways to implement models for distillation column optimization [Barttfeld et al., 2003, Grossmann et al., 2005]. One such implementation is selected for comparison of computational performance with the model presented in this work. The same setup as in Section 4.3.1 is solved for the well known distillation model formulation described in [Viswanathan and Grossmann, 1993]. This reference model uses liquid molar flows instead of flow ratios and a different superstructure to implement variable column configurations, illustrated in Figure 4.6. Monotonicity constraints like Equations (4.15)-(4.21) in Section 4.2.2 can not be implemented in a straight-forward way for the reference model and are thus not included. Using the reference model, the optimization problem is not solved in ten hours of computation time for a single run. The lower bound for the objective value of the reference model calculated after this time is 57.2% of the global optimum. Even considering statistical variation of computation time, this is orders of magnitude slower than solving the optimization problem using the model formulation proposed in this work. The full equations of the reference model as well as parameter and domain specifications are listed in Appendix C.

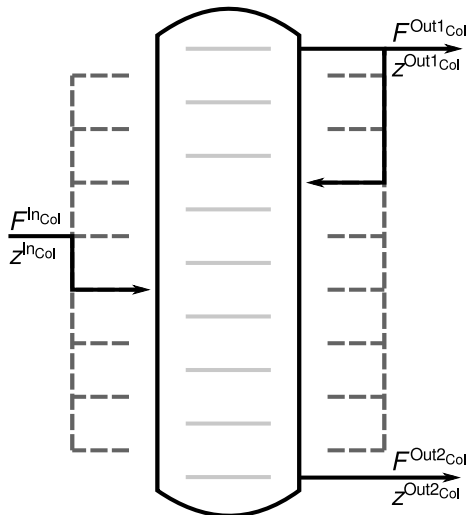
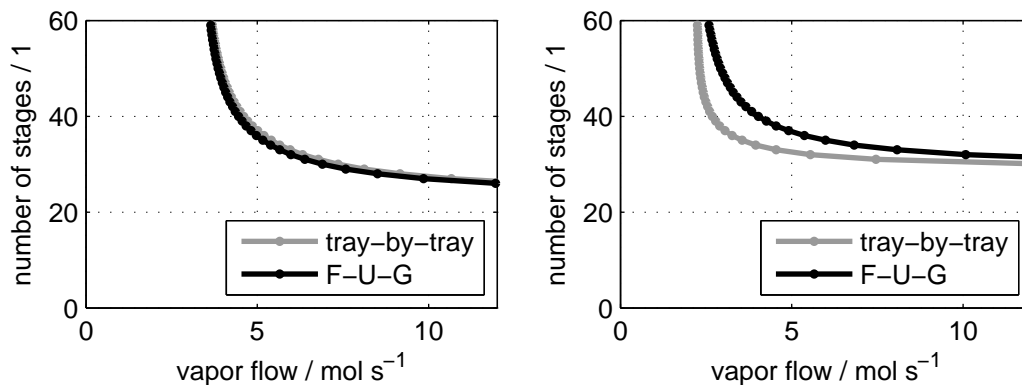


Figure 4.6: Column model superstructure as presented in [Viswanathan and Grossmann, 1993] with variable feed position and distillate reflux position.

4.3.3 Comparison with Fenske-Underwood-Gilliland

Short-cut methods are often applied to obtain first estimates for distillation column designs in early steps of design frameworks. One of the most prominent methods is based on the work of Fenske, Underwood and Gilliland, see Appendix D for a detailed description. The so called Fenske-Underwood-Gilliland (F-U-G) method provides a correlation between number of stages and reflux ratio for a given separation task, which is used for economical evaluation and optimization. It does not require a full tray-by-tray column model and therefore allows faster calculation. However, the F-U-G method deploys an empirical correlation in addition to the assumptions made for the tray-by-tray model in Section 4.2.1, introducing deviations from the exact solution. Figure 4.7 shows two example calculations comparing the F-U-G method and results obtained from the model given in Section 4.2.1. The results are calculated for fixed product specifications, obtaining a feasible solution for the vapor flow for each fixed number of stages with GAMS/BARON. Figure 4.7 demonstrates that the F-U-G method fits the exact solution well in some cases, but may also express deviations over 20 % in both number of stages and vapor flow in other cases. Therefore, it should be followed up by more rigorous methods when deployed as a first step in hierarchical design frameworks.



(a) Case 1: $z^{\text{In}}=0.5$, $F^{\text{In}}=1 \text{ mol s}^{-1}$,
 $\alpha=1.3$, $z^{\text{Out1}}=0.95$, $z^{\text{Out2}}=0.05$, $q=1$

(b) Case 2: $z^{\text{In}}=0.9$, $F^{\text{In}}=1 \text{ mol s}^{-1}$,
 $\alpha=1.3$, $z^{\text{Out1}}=0.95$, $z^{\text{Out2}}=0.01$, $q=1$

Figure 4.7: Correlation between number of stages and vapor flow for binary separation tasks.

4.3.4 Optimal Flowsheet Results

In this section, flowsheet options for the separation of n-dodecanal and 2-methylundecanal using distillation and crystallization units are evaluated based on globally optimal solutions of a conceptual process model. Utilizing deterministic global optimization prevents results from being adversely affected by poor local optima. Hierarchical design frameworks profit from this strategy as later design steps rely on optimization results from prior steps.

The deterministic global optimization software BARON 11.5.2 (GAMS 23.9.5, Linux, x64) is applied for minimizing the objective function of the process model described above. CPLEX 12.4.0.1 and CONOPT 3.15G are chosen as subsolvers required by BARON for linear programming and non-linear programming. Solver options are set to default values except. Only the termination condition “optcr”, the relative difference between upper and lower bound, is set to 0.0001. Note that only one global optimum is identified using these options even in the case of multiple global optima. The GAMS processes are executed consecutively with 2048 MB of memory allocated to each process. A standard desktop computer (Intel® Core™ i5-6500 @ 3.20 GHz) with a virtual Linux environment is used for the computations.

There is no initial solution provided to the solver. Finding good local solutions early allows for more efficient bounding and thereby influences the overall computation time. Therefore, the complete evolution of upper and lower bound to the objective function during branch-and-bound is reported Table 4.3 lists the parameters and domains of variables used in this case study.

GAMS reports the size of the optimization problem as 1008 equality and inequality conditions and 525 variables with 156 of these being binary variables. The model has 3640 nonzero elements with 1816 being non-linear. The superstructure for the distillation column allows approximately 3200 possible configurations and the operating parameters correspond to two real-numbered degrees of freedom. The superstructures for the distillation units each allow two possible configurations with two real-numbered degrees of freedom for the operating parameters.

The computational results are given in Figure 4.8. The computation time ranges in the order of over twelve minutes to under five hours, which is feasible for this optimization task also considering the size of the problem. Flowsheet

Table 4.3: Parameter and domain specifications for the hybrid separation process.
 [Reprinted from Kunde et al., 2016, with permission from Elsevier]

parameter	value	variable	domain
F^{InSys}	1.8 mol s^{-1}	l^{Col}	$[3, 80]$
z^{InSys}	0.1	z^{Out1Sys}	$[0, 0.01]$
k_{diff}	0.086^{a}	z^{Out2Sys}	$[0.99, 1]$
x^{minT}	0.9	w, x, y, z, Y, k, ν	$[0, 1]$
α	1.37	S, L, V, F	$[0 \text{ mol s}^{-1}, 64.8 \text{ mol s}^{-1}]$
$l_{\text{r}}^{\text{max}}$	80	β	$\{0, 1\}$
$l_{\text{s}}^{\text{max}}$	80		

^a[Beierling and Ruether, 2012, Beierling et al., 2013]

option (b) (see Figure 4.4 for the graphical representation) is identified as the globally optimal flowsheet. The optimal cost of flowsheet option (b) is approximately 2 % lower than the optimal cost of flowsheet option (a), which is essentially the same flowsheet without feedback loops. The feedback flow in flowsheet option (b) is small resulting in a correspondingly small difference of the objective function values for both flowsheets. However, the modeling detail of conceptual process models used in this design step does not cover possible undesired effects of feedback loops that may arise in later design steps with more detailed models. Therefore, both flowsheet options (a) and (b) should be included in further investigations. The stand-alone distillation column (d) is better than flowsheet options (c) and (e) despite added crystallizer units.

Note that parallelization is expected to significantly increase computational performance as is already implied in Chapter 2. As a second note, good local optima are quickly determined by BARON. The majority of time is spent on identifying solutions within the range of the termination conditions and on converging the lower bound to prove that no better solution exists. Recall, lower bounds to the objective function for evaluation of the quality of local solutions are not provided by local or stochastic methods, potentially leading to wrong results for the design task.

It should be noted that the computational performance may strongly depend on the software version of BARON and utilized subsolvers. Figure 4.9 depicts the computation time for solving flowsheet option (c) with selected GAMS

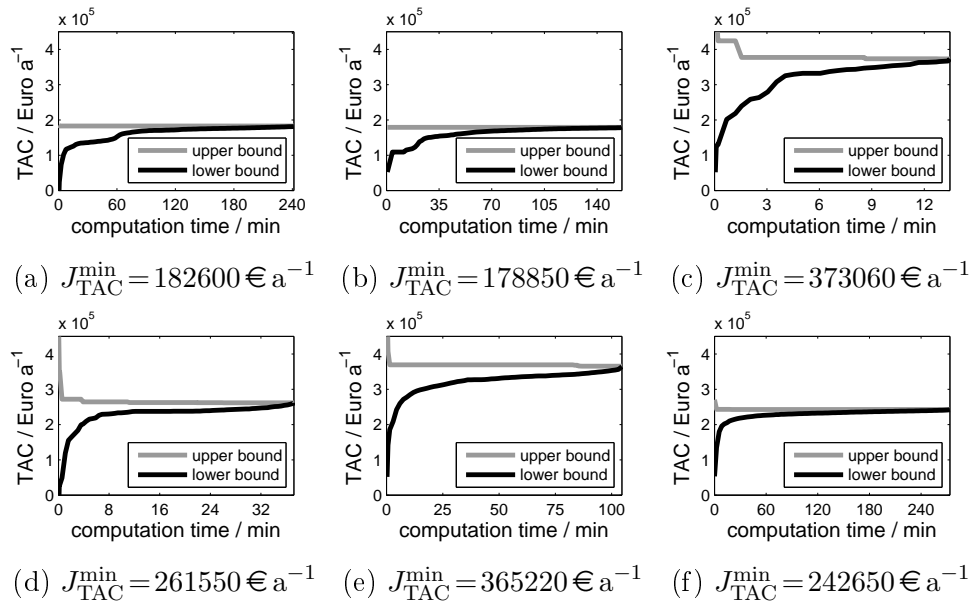


Figure 4.8: Optimization progress and globally optimal objective function for each flowsheet option. Same order as in Figure 4.4.

versions and according versions of BARON and subsolvers. Hardware, software and options are the same as for Figure 4.8. A globally optimal solution is provided as initial point. The resulting computation time varies over one order of magnitude, with newer software versions not being strictly faster than older versions. Regardless of this variation, the model formulation presented in this work provides a feasible method for obtaining globally optimal solutions for conceptual design of combined distillation/melt crystallization processes.

4.4 Conclusion

Flowsheet selection is a fundamental step in process design that is adversely affected by poor local optima. Application of deterministic global optimization for reliable flowsheet selection is demonstrated for a process combining distillation and melt crystallization units. Providing suitable model formulations allows for globally solving more complex models than previously published. This enables using tray-by-tray distillation models instead of or subsequent to shortcut methods, e.g. Fenske-Underwood-Gilliland, in hierarchical design frameworks, increasing model validity for the cost of increased model complexity.

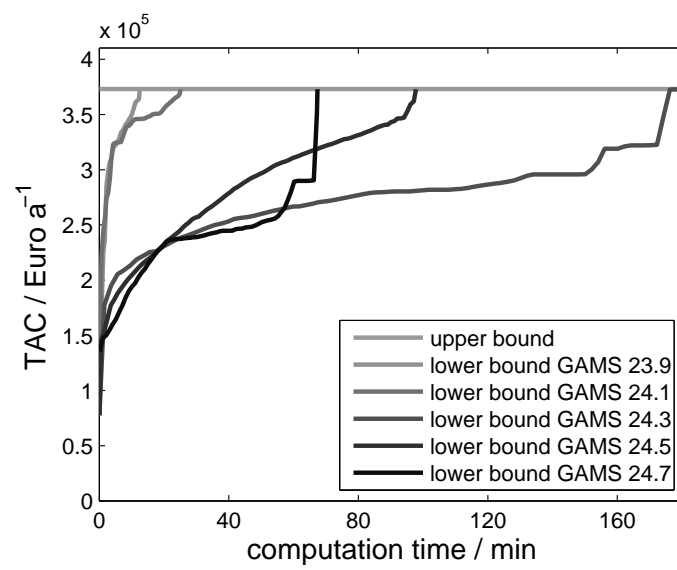


Figure 4.9: Optimization progress for flowsheet option (c) in Figure 4.4 for different GAMS versions and according solver versions.

Chapter 5

Conclusion and Future Perspectives

Hierarchical design frameworks allow to apply deterministic global optimization when computationally feasible and only switch to other methods when it becomes necessary. Thereby the most fundamental choices for design tasks solved in hierarchical frameworks can be guaranteed not to suffer from poor local optima. In this work the application of deterministic global optimization to conceptual process models originating from early design stages or lower steps of a hierarchical design framework is demonstrated. Suitable model formulations are provided that allow analysis and design of selected processes based on globally optimal solutions.

The work presented here allows to extend the application of global optimization to new processes. As one of the results, design rules for multistage separation processes are derived from analyzing the influence of process parameters on globally optimal configurations. In more detail, multistage configurations for three separation processes, namely melt crystallization, solution crystallization and filtration, are studied using global optimization. The findings are qualitatively the same in all three cases, allowing for generalization of corresponding design rules.

The complexity of problems solved globally is increased by exploiting problem-specific properties. Most notably, specific monotonicity properties for distillation column models are proven and exploited to reduce the computational effort of global optimization.

Furthermore, a method based on statistical analysis for evaluating the computational effort of solving optimization problems with branch-and-bound algorithms is proposed.

Process design tools based on global optimization require suitable problem formulations and solution methods to at least partly compensate the increased computational effort compared to local optimization. Model formulations adapted to the applied algorithm and solution methods exploiting problem-specific properties enable significant reduction of the computational effort for global optimization. However, general solvers are not guaranteed to identify all beneficial properties of a problem. As a future perspective, this may be addressed by a database compiling suitable problem formulations and according specialized solution algorithms. Such a database may provide the means to determine global solutions to commonly encountered problems.

Appendix A

Integral Distribution Coefficient for Melt Crystallization

The differential distribution coefficient is a measure for the efficiency of separation by crystallization processes. It is used in this work for melt crystallization of eutectic mixtures with impurity inclusions in the crystals. The differential distribution coefficient is defined as the molar fraction of impurities in the crystal w_{imp} divided by the molar fraction of impurities in the liquid x_{imp} [Lewis et al., 2015]:

$$k_{\text{diff}} := \frac{w_{\text{imp}}}{x_{\text{imp}}}. \quad (\text{A.1})$$

Note that k_{diff} is defined for infinitely small amounts of crystal produced, i. e. a constant composition of the liquid during the crystallization.

The definition of k_{diff} can be rewritten as

$$\frac{\partial S_{\text{imp}}}{\partial S} = k_{\text{diff}} \frac{L_{\text{imp}}}{L}, \quad (\text{A.2})$$

with S and L being the amounts (or cumulated molar flows) of the crystal and the liquid, respectively.

The integral distribution coefficient is defined as

$$k_{\text{int}} := \frac{w_{\text{imp}}^{\text{end}}}{x_{\text{imp}}^{\text{start}}} = \frac{S_{\text{imp}}^{\text{end}} L_{\text{imp}}^{\text{start}}}{S_{\text{end}} L_{\text{imp}}^{\text{start}}}, \quad (\text{A.3})$$

With superscripts “start” and “end” describing conditions before and after crystallization, respectively.

Two intermediate steps are needed to determine k_{int} . Firstly, S^{end} is obtained from the definition of the crystal yield Y .

$$Y := \frac{S^{\text{end}}}{L^{\text{start}}} \quad (\text{A.4})$$

Secondly, the cumulative amount of impurity in the crystal $S_{\text{imp}}^{\text{end}}$ is calculated, starting from the equation for k_{diff} . In this context, the crystal amount S can be interpreted as the crystallization progress, with $S = S^{\text{start}} = 0$ meaning zero progress and $S = S^{\text{end}}$ meaning completed crystallization. Reordering Equation (A.2) leads to

$$\frac{1}{L_{\text{imp}}^{\text{start}} - S_{\text{imp}}} \frac{\partial S_{\text{imp}}}{\partial S} = k_{\text{diff}} \frac{1}{L^{\text{start}} - S}, \quad (\text{A.5})$$

which is integrated over the crystallization progress S from S^{start} to S^{end} with the assumption of $k_{\text{diff}} := \text{constant}$ to obtain

$$\frac{L_{\text{imp}}^{\text{start}}}{L_{\text{imp}}^{\text{start}} - S_{\text{imp}}^{\text{end}}} = \left(\frac{L^{\text{start}}}{L^{\text{start}} - S^{\text{end}}} \right)^{k_{\text{diff}}}. \quad (\text{A.6})$$

Note that if k_{diff} depends on the crystallization progress, this integration gets more complicated and may only be solved analytically for special choices of $k_{\text{diff}}(S)$. Rearranging this result and using the definition in Equation (A.4) leads to the formula for calculating the cumulative impurity in the crystal $S_{\text{imp}}^{\text{end}}$ as a function of the yield Y :

$$S_{\text{imp}}^{\text{end}} = L_{\text{imp}}^{\text{start}} \left(1 - (1 - Y)^{k_{\text{diff}}} \right). \quad (\text{A.7})$$

Recall the definition for k_{int} in Equation (A.3). The intermediate results in Equation (A.4) and Equation (A.7) are used to rewrite k_{int} for constant differential distribution coefficients in terms of k_{diff} and Y only.

$$k_{\text{int}} = \frac{1 - (1 - Y)^{k_{\text{diff}}}}{Y} \quad (\text{A.8})$$

Appendix B

A Property of Multicomponent Distillation

In this section, it is shown that

$$\tilde{x}_{j,l_s} \geq \tilde{x}_{j,1} \quad (\text{B.1})$$

holds for pseudo-components defined as

$$\tilde{x}_{j,l_s} = \sum_{i=1}^j x_{i,l_s}, \quad \tilde{y}_{j,l_s} = \sum_{i=1}^j y_{i,l_s}, \quad (\text{B.2})$$

in mixtures of N_C species with invariable order of relative volatilities

$$\alpha_1 > \alpha_2 > \dots > \alpha_{N_C} = 1 \quad (\text{B.3})$$

for the stripping section of a distillation column with mass balance equation

$$x_{j,l_s+1} = \nu y_{j,l_s} + (1 - \nu) x_{j,1}. \quad (\text{B.4})$$

for all species $j=1, \dots, N_C-1$ and stages $l_s=1, \dots, l_s^{\max}$. Superscripts indicating the stripping section are omitted in this section for better readability.

First, a property of the phase equilibrium is discussed in Observation 3. Then, Equation (B.1) is proven in Observation 4. Note that this proof also implies a corresponding property in the rectifying section of a distillation column. Also note that relative volatilities do not need to be constant, rendering Equation (B.1) valid for a class of non-ideal multicomponent mixtures.

Observation 3. Let $\alpha \in \mathbb{R}^{N_C}$, $\mathbf{x}, \mathbf{y} \in [0, 1]^{N_C}$ and $\tilde{\mathbf{x}}, \tilde{\mathbf{y}} \in [0, 1]^{N_C-1}$ be given, with

$$\begin{aligned} \alpha_1 &> \alpha_2 > \dots > \alpha_{N_C} > 1, \\ \sum_{i=1}^{N_C} x_i &= 1, \\ \tilde{x}_j &= \sum_{i=1}^j x_i, \quad \tilde{y}_j = \sum_{i=1}^j y_i, \quad j = 1, \dots, N_C-1, \end{aligned}$$

then the function

$$\mathbf{g} : [0, 1]^{N_C} \rightarrow \mathbb{R}^{N_C}, \quad \mathbf{x} \mapsto y_i := \frac{\alpha_i x_i}{\sum_{k=1}^{N_C} \alpha_k x_k}, \quad i = 1, \dots, N_C,$$

satisfies the property

$$\tilde{y}_j \geq \tilde{x}_j \quad \text{for all } j = 1, \dots, N_C-1.$$

Proof. Let $\bar{x}_j \in [0, 1]$, $\bar{x}_j = \sum_{i=j+1}^{N_C} x_i$, and relative volatilities $\tilde{\alpha}_j \in [\alpha_j, \alpha_1]$, $\bar{\alpha}_j \in [\alpha_{N_C}, \alpha_{j+1}]$ be defined by

$$\tilde{\alpha}_j := \frac{\sum_{i=1}^j \alpha_i x_i}{\sum_{i=1}^j x_i}, \quad \bar{\alpha}_j := \frac{\sum_{i=j+1}^{N_C} \alpha_i x_i}{\sum_{i=j+1}^{N_C} x_i}.$$

Then \tilde{y}_j satisfies

$$\tilde{y}_j = \frac{\tilde{\alpha}_j \tilde{x}_j}{\tilde{\alpha}_j \tilde{x}_j + \bar{\alpha}_j \bar{x}_j} \geq \frac{\tilde{\alpha}_j \tilde{x}_j}{\tilde{\alpha}_j \tilde{x}_j + \tilde{\alpha}_j \bar{x}_j} = \frac{\tilde{\alpha}_j \tilde{x}_j}{\tilde{\alpha}_j (\tilde{x}_j + \bar{x}_j)} = \tilde{x}_j$$

for all $j = 1, \dots, N_C-1$. \square

Observation 4. Let $\nu \in [0, 1]$ and $\tilde{\mathbf{x}}_1 \in [0, 1]^{N_C-1}$ be given. Then, the iteration defined by

$$\mathbf{f} : [0, 1]^{N_C-1} \rightarrow \mathbb{R}^{N_C-1}, \quad \tilde{\mathbf{x}}_{l_s} \mapsto \tilde{\mathbf{x}}_{l_s+1} := \nu \mathbf{y}(\tilde{\mathbf{x}}_{l_s}) + (1 - \nu) \tilde{\mathbf{x}}_1$$

satisfies the following property:

$$\tilde{x}_{j,l_s} \geq \tilde{x}_{j,1} \quad \text{holds for all } j = 1, \dots, N_C-1, \quad l_s = 1, \dots, l_s^{\max}.$$

Proof. Observation 3 is used to show that

$$\tilde{x}_{j,2} = \nu \tilde{y}_{j,1} + (1 - \nu) \tilde{x}_{j,1} \geq \nu \tilde{x}_{j,1} + (1 - \nu) \tilde{x}_{j,1} = \tilde{x}_{j,1}.$$

Now suppose $\tilde{x}_{j,l_s-1} \geq \tilde{x}_{j,1}$, then

$$\begin{aligned} \tilde{x}_{j,l_s} &= \nu \tilde{y}_{j,l_s-1} + (1 - \nu) \tilde{x}_{j,1} \dots \\ &\geq \nu \tilde{x}_{j,l_s-1} + (1 - \nu) \tilde{x}_{j,1} \geq \nu \tilde{x}_{j,1} + (1 - \nu) \tilde{x}_{j,1} = \tilde{x}_{j,1}, \end{aligned}$$

which completes the proof. \square

Appendix C

Reference Distillation Model

Given below is an implementation of a distillation model with variable length and variable feed stage given in [Viswanathan and Grossmann, 1993]. Parameter and domain specifications are listed in Table C.1. The feasible solution space of this model is equivalent to that of the model used in Section 4.3.1 except for restrictions on the domain of liquid flows L . Liquid flows L do not appear in the latter model and therefore no domain is defined.

Objective function:

$$\begin{aligned}
 J_{\text{TAC}} = & \\
 & (17544 V \text{ s mol}^{-1} \\
 & +2364.5 (0.2 l^{\text{Col}} + 4)^{0.82} (0.2378 V \text{ s mol}^{-1} + 0.0221 F^{\text{Out2Col}} \text{ s mol}^{-1})^{0.533} \\
 & +2009.7 l^{\text{Col}} (0.2378 V \text{ s mol}^{-1} + 0.0221 F^{\text{Out2Col}} \text{ s mol}^{-1}) \\
 & -171.4 l^{\text{Col}} (0.2378 V \text{ s mol}^{-1} + 0.0221 F^{\text{Out2Col}} \text{ s mol}^{-1})^{0.5} \\
 & +173.6 l^{\text{Col}}) \text{ € a}^{-1}
 \end{aligned} \tag{C.1}$$

Mass balances for each stage:

$$0 = \beta_1^{\text{InCol}} F^{\text{InCol}} z^{\text{InCol}} + V (y_2 - y_1) - L_1 x_1 + \beta_1^{\text{L}} L^{\text{reflux}} y_1 \tag{C.2}$$

$$\begin{aligned}
 0 = & \beta_l^{\text{InCol}} F^{\text{InCol}} z^{\text{InCol}} + V (y_{l+1} - y_l) \\
 & + L_{l-1} x_{l-1} - L_l x_l + \beta_l^{\text{L}} L^{\text{reflux}} y_1, \quad l = 2, \dots, l^{\text{max}} - 1
 \end{aligned} \tag{C.3}$$

$$\begin{aligned}
 0 = & \beta_{l^{\text{max}}}^{\text{InCol}} F^{\text{InCol}} z^{\text{InCol}} + V (x_{l^{\text{max}}} - y_{l^{\text{max}}}) \\
 & + L_{l^{\text{max}}-1} x_{l^{\text{max}}-1} - L_{l^{\text{max}}} x_{l^{\text{max}}} + \beta_{l^{\text{max}}}^{\text{L}} L^{\text{reflux}} y_1
 \end{aligned} \tag{C.4}$$

Mass balance for liquid flow:

$$0 = \beta_1^{\text{InCol}} F^{\text{InCol}} - L_1 + \beta_1^L L^{\text{reflux}} \quad (\text{C.5})$$

$$0 = \beta_l^{\text{InCol}} F^{\text{InCol}} + L_{l-1} - L_l + \beta_l^L L^{\text{reflux}}, \quad l = 2, \dots, l^{\text{max}} \quad (\text{C.6})$$

Phase equilibrium:

$$0 = (-y_l ((\alpha - 1) x_l + 1) + \alpha x_l), \quad l = 1, \dots, l^{\text{max}} \quad (\text{C.7})$$

Mass balance for condenser:

$$0 = L^{\text{reflux}} - V + F^{\text{Out1Col}} \quad (\text{C.8})$$

Mass balance for whole column:

$$0 = F^{\text{InCol}} - F^{\text{Out1Col}} - F^{\text{Out2Col}} \quad (\text{C.9})$$

$$0 = F^{\text{InCol}} z^{\text{InCol}} - F^{\text{Out1Col}} y_1 - F^{\text{Out2Col}} x_{l^{\text{max}}} \quad (\text{C.10})$$

Configuration constraints:

$$1 = \sum_l \beta_l^{\text{InCol}}, \quad 1 = \sum_l \beta_l^L, \quad 0 \leq \sum_l \beta_l^{\text{InCol}} - \sum_l \beta_l^L \quad (\text{C.11})$$

Calculation of column length:

$$0 = -l^{\text{Col}} + l^{\text{max}} + 1 - \sum_{l=1}^{l^{\text{max}}} \beta_l^L l \quad (\text{C.12})$$

Table C.1: Alternative distillation model: Parameter and domain specifications.

parameter	value	variable	domain	variable	domain
F^{InCol}	1 mol s^{-1}	l^{Col}	$[3, 50]$	x, y	$[0, 1]$
z^{InCol}	0.1	$x_{l^{\text{max}}}$	$[0, 0.01]$	V, L	$[0 \text{ mol s}^{-1}, 20 \text{ mol s}^{-1}]$
l^{max}	50	y_1	$[0.99, 1]$	F	$[0 \text{ mol s}^{-1}, 1 \text{ mol s}^{-1}]$
				β	$\{0, 1\}$

Appendix D

Fenske-Underwood-Gilliland Method for Global Optimization

This chapter describes an implementation of the distillation column design method based on the works of Fenske, Underwood and Gilliland. The notation is kept close to that of the distillation model in Section 4.2.1. The method is given below for mixtures of N^C components since it is generally applied to multicomponent mixtures. The Fenske-Underwood-Gilliland equations are solved in GAMS with branch-and-bound solver BARON. In the following, superscripts denoting the distillation column are omitted for simplicity.

The minimum stage number is determined via the Fenske equation [Fenske, 1932] using the pre-defined light key component i_{LK} and heavy key component i_{HK} :

$$0 = - \left(\frac{\alpha_{i_{LK}}}{\alpha_{i_{HK}}} \right)^{l_{\min}^{\text{Col}}} F_{i_{HK}}^{\text{Out1}} F_{i_{LK}}^{\text{Out2}} + F_{i_{LK}}^{\text{Out1}} F_{i_{HK}}^{\text{Out2}}. \quad (\text{D.1})$$

In case of binary mixtures $\alpha_{i_{HK}}$ equals one. Note that non-key components are not considered in the equation above, resulting in deviations from the exact solution for multicomponent mixtures.

The minimum reflux ratio is calculated with the Underwood method, described

in e. g. [Doherty et al., 2008]:

$$0 = -(1 - q) + \sum_{i=1}^{N^C} \alpha_i z_i^{\text{In}} b_{ij}, \quad j = 1, \dots, N^C - 1, \quad (\text{D.2})$$

$$0 = \beta_{2,j} \beta_{1,j+1} (-V_{\min} + \sum_{i=1}^{N^C} \alpha_i F_i^{\text{Out1}} b_{ij}), \quad j = 1, \dots, N^C - 1, \quad (\text{D.3})$$

$$0 = -b_{ij} (\alpha_i - \phi_j) + 1, \quad i = 1, \dots, N^C, \quad j = 1, \dots, N^C - 1, \quad (\text{D.4})$$

with variables ϕ obeying $\alpha_1 \geq \phi_1 \geq \alpha_2 \geq \phi_2 \geq \dots$

Equation (D.3) is only applied for distributing components, e. g. if and only if corresponding binary control variables $\beta \in \{0, 1\}$ equal one, otherwise control variables equal zero. Non-distributing components are determined by probing for output flows with infeasible values. The control variables are calculated as

$$0 = -V_{\text{probe},\min} + \sum_{i=1}^{N^C} \alpha_i F_{\text{probe},i}^{\text{Out1}} b_{ij}, \quad j = 1, \dots, N^C - 1 \quad (\text{D.5})$$

$$0 \geq -\beta_{1,j} z_j^{\text{In}} F^{\text{In}} + F_{\text{probe},j}^{\text{Out1}}, \quad j = i_{\text{LK}}, \dots, N^C, \quad (\text{D.6})$$

$$0 \leq -\beta_{1,j} z_j^{\text{In}} F^{\text{In}} + z_j^{\text{In}} F^{\text{In}} + F_{\text{probe},j}^{\text{Out1}}, \quad j = i_{\text{LK}}, \dots, N^C, \quad (\text{D.7})$$

$$0 \geq -\beta_{2,j} z_j^{\text{In}} F^{\text{In}} + z_j^{\text{In}} F^{\text{In}} - F_{\text{probe},j}^{\text{Out1}}, \quad j = 1, \dots, i_{\text{HK}}, \quad (\text{D.8})$$

$$0 \leq -\beta_{2,j} z_j^{\text{In}} F^{\text{In}} + 2 z_j^{\text{In}} F^{\text{In}} - F_{\text{probe},j}^{\text{Out1}}, \quad j = 1, \dots, i_{\text{HK}}, \quad (\text{D.9})$$

e. g. if $F_{\text{probe},j}^{\text{Out1}} < 0$ then $\beta_{1,j} = 0$ and component j is non-distributing; otherwise, if $F_{\text{probe},j}^{\text{Out1}} > 0$ then $\beta_{1,j} = 1$.

The control variables are used to set actual recovery rates for non-distributing components.

$$0 \geq -\beta_{1,j} z_j^{\text{In}} F^{\text{In}} + F_j^{\text{Out1}}, \quad j = i_{\text{LK}}, \dots, N^C \quad (\text{D.10})$$

$$0 \geq -\beta_{2,j} z_j^{\text{In}} F^{\text{In}} + z_j^{\text{In}} F^{\text{In}} - F_j^{\text{Out1}}, \quad j = 1, \dots, i_{\text{HK}} \quad (\text{D.11})$$

Note that auxiliary variables b_{ij} may be unbounded when considering the equations given above, therefore they are artificially restricted to large values. Note that a bilinear implementation of the Underwood equations is also given in [Nallasivam et al., 2016] for the global optimization of near-ideal multicomponent distillation at minimum reflux conditions.

The correlation between actual number of stages and reflux ratio in [Gilliland,

1940] is applied in the version from [Eduljee, 1975] with vapor molar flow V instead of reflux ratio:

$$0 = -(l^{\text{Col}} - l_{\text{min}}^{\text{Col}}) + 0.75(1 - a^{0.5668})(l^{\text{Col}} + 1), \quad (\text{D.12})$$

$$0 = (1 - a)V - V_{\text{min}}, \quad (\text{D.13})$$

with auxiliary variable $a \in [0, 1]$.

Mass balances for the distillation column read

$$0 = -F^{\text{In}} z_j^{\text{In}} + F_j^{\text{Out1}} + F_j^{\text{Out2}}, \quad j = 1, \dots, N^{\text{C}}, \quad (\text{D.14})$$

$$0 = -F^{\text{Out1}} + \sum_{i=1}^{N^{\text{C}}} F_i^{\text{Out1}}, \quad (\text{D.15})$$

$$0 = -F^{\text{Out2}} + \sum_{i=1}^{N^{\text{C}}} F_i^{\text{Out2}}. \quad (\text{D.16})$$

Additional restrictions for the distillate flow F^{Out1} read

$$0 \geq -V_{\text{min}} + F^{\text{Out1}}, \quad (\text{D.17})$$

$$0 \geq -V + F^{\text{Out1}}. \quad (\text{D.18})$$

Product specifications are given as molar fractions of the respective desired products at both outlets z^{Out1} and z^{Out2} :

$$0 = -z^{\text{Out1}} F^{\text{Out1}} + \sum_{i=1}^{i_{\text{LK}}} F_i^{\text{Out1}}, \quad (\text{D.19})$$

$$0 = -z^{\text{Out2}} F^{\text{Out2}} + \sum_{i=i_{\text{HK}}}^{N^{\text{C}}} F_i^{\text{Out2}}. \quad (\text{D.20})$$

Table D.1: Fenske-Underwood-Gilliland: Domain specifications.

variable	domain	variable	domain
$l^{\text{Col}}, l_{\text{min}}^{\text{Col}}$	$[1, 200]$	V	$[0 \text{ mol s}^{-1}, 100F^{\text{In}}]$
$F_{\text{probe}}^{\text{Out1}}$	$[-20F^{\text{In}}, 20F^{\text{In}}]$	F	$[0 \text{ mol s}^{-1}, F^{\text{In}}]$
a	$[0, 1]$	β	$\{0, 1\}$
b	$[-1 \cdot 10^5, 1 \cdot 10^5]$		

Bibliography

MINLP Library 2. Revision: 327. URL <http://www.gamsworld.org/minlp/minlplib2/html/>.

T. Achterberg. *Constraint Integer Programming*. PhD thesis, Technische Universität Berlin (Germany), 2007.

M. Ballerstein, A. Kienle, C. Kunde, D. Michaels, and R. Weismantel. Towards global optimization of combined distillation-crystallization processes for the separation of closely boiling mixtures. volume 29 of *Computer Aided Chemical Engineering*, pages 552 – 556. Elsevier, 2011. doi: 10.1016/B978-0-444-53711-9.50111-5.

M. Ballerstein, A. Kienle, C. Kunde, D. Michaels, and R. Weismantel. Deterministic global optimization of binary hybrid distillation/melt-crystallization processes based on relaxed MINLP formulations. *Optimization and Engineering*, 16:409–440, 2014. doi: 10.1007/s11081-014-9267-5.

M. Barttfeld, P. A. Aguirre, and I. E. Grossmann. Alternative representations and formulations for the economic optimization of multicomponent distillation columns. *Computers & Chemical Engineering*, 27(3):363–383, 2003. doi: 10.1016/S0098-1354(02)00213-2.

T. Beierling and F. Ruether. Separation of the isomeric long-chain aldehydes dodecanal/2-methylundecanal via layer melt crystallization. *Chemical Engineering Science*, 77:71–77, 2012. doi: 10.1016/j.ces.2012.01.055.

T. Beierling, J. Osiander, and G. Sadowski. Melt crystallization of isomeric long-chain aldehydes from hydroformylation. *Separation and Purification Technology*, 118:13–24, 2013. doi: 10.1016/j.seppur.2013.06.023.

- T. Beierling, J. Micovic, P. Lutze, and G. Sadowski. Using complex layer melt crystallization models for the optimization of hybrid distillation/melt crystallization processes. *Chemical Engineering and Processing: Process Intensification*, 85:10–23, 2014. doi: 10.1016/j.cep.2014.07.011.
- L. T. Biegler and I. E. Grossmann. Retrospective on optimization. *Computers & Chemical Engineering*, 28(8):1169–1192, 2004. doi: 10.1016/j.compchemeng.2003.11.003.
- M. R. Bussieck, A. S. Drud, and A. Meeraus. MINLPLib—a collection of test models for mixed-integer nonlinear programming. *INFORMS Journal on Computing*, 15(1):114–119, January 2003. doi: 10.1287/ijoc.15.1.114.15159.
- M. M. Daichendt and I. E. Grossmann. Integration of hierarchical decomposition and mathematical programming for the synthesis of process flowsheets. *Computers & Chemical Engineering*, 22(1-2):147–175, 1998.
- M. F. Doherty, Z. T. Fidkowski, M. F. Malone, and R. Taylor. *Perry's Chemical Engineers' Handbook*, chapter Distillation. McGraw-Hill, 8th edition, 2008.
- J. M. Douglas. Hierarchical decision procedure for process synthesis. *AIChE Journal*, 31(3):353–362, 1985.
- J. M. Douglas. *Conceptual design of chemical processes*. McGraw-Hill Book Company, 1988.
- H. E. Eduljee. Equations replace Gilliland Plot. *Hydrocarbon Processing*, 54(9), 1975.
- M. R. Fenske. Fractionation of straight-run pennsylvania gasoline. *Industrial & Engineering Chemistry*, 24(5):482–485, 1932. doi: 10.1021/ie50269a003.
- M. B. Franke, A. Górak, and J. Strube. Auslegung und Optimierung von hybriden Trennverfahren. *Chemie-Ingenieur-Technik*, 76(3):199–210, 2004.
- M. B. Franke, N. Nowotny, E. Ndocko, A. Górak, and J. Strube. Design and optimization of a hybrid distillation/melt crystallization process. *AIChE Journal*, 54(11):2925–2942, 2008. doi: 10.1002/aic.11605.

- E. R. Gilliland. Multicomponent rectification. *Industrial & Engineering Chemistry*, 32(8):1101–1106, 1940. doi: 10.1021/ie50368a017.
- A. Górak and E. Sorensen. *Distillation: Fundamentals and Principles*. Academic Press, 2014. ISBN 9780123865472.
- I. E. Grossmann. Mixed-integer programming approach for the synthesis of integrated process flowsheets. *Computers & Chemical Engineering*, 9(5):463–482, 1985.
- I. E. Grossmann and L. T. Biegler. Part II. Future perspective on optimization. *Computers & Chemical Engineering*, 28(8):1193–1218, 2004. doi: 10.1016/j.compchemeng.2003.11.006.
- I. E. Grossmann, P. A. Aguirre, and M. Barttfeld. Optimal synthesis of complex distillation columns using rigorous models. *Computers & Chemical Engineering*, 29(6):1203–1215, 2005. doi: 10.1016/j.compchemeng.2005.02.030.
- J. Holtbruegge, H. Kuhlmann, and P. Lutze. Conceptual design of flowsheet options based on thermodynamic insights for (reaction-)separation processes applying process intensification. *Industrial and Engineering Chemistry Research*, 53(34):13412–13429, 2014. doi: 10.1021/ie502171q.
- R. Horst and H. Tuy. *Global optimization: Deterministic approaches*. Springer Science & Business Media, 1996. doi: 10.1007/978-3-662-03199-5.
- M. Kaspereit, S. Swernath, and A. Kienle. Evaluation of competing process concepts for the production of pure enantiomers. *Organic Process Research and Development*, 16(2):353–363, 2012. doi: 10.1021/op200285v.
- T. Koch, T. Achterberg, E. Andersen, O. Bastert, T. Berthold, R. E. Bixby, E. Danna, G. Gamrath, A. M. Gleixner, S. Heinz, A. Lodi, H. Mittelmann, T. Ralphs, D. Salvagnin, D. E. Steffy, and K. Wolter. MIPLIB 2010. *Mathematical Programming Computation*, 3(2):103–163, 2011. doi: 10.1007/s12532-011-0025-9.
- S. Kossack, K. Kraemer, and W. Marquardt. Efficient optimization-based design of distillation columns for homogenous azeotropic mixtures. *Industrial*

- and Engineering Chemistry Research*, 45(25):8492–8502, 2006. doi: 10.1021/ie060117h.
- S. Kossack, K. Kraemer, R. Gani, and W. Marquardt. A systematic synthesis framework for extractive distillation processes. *Chemical Engineering Research and Design*, 86(7):781–792, 2008. doi: 10.1016/j.cherd.2008.01.008.
- S. Kravanja, S. Šilih, and Z. Kravanja. The multilevel MINLP optimization approach to structural synthesis: The simultaneous topology, material, standard and rounded dimension optimization. *Advances in Engineering Software*, 36(9):568–583, 2005. doi: 10.1016/j.advengsoft.2005.03.004.
- C. Kunde and A. Kienle. Deterministic global optimization of multistage melt crystallization processes in hydroformylation. volume 37 of *Computer Aided Chemical Engineering*, pages 1061–1066. Elsevier, 2015. doi: 10.1016/B978-0-444-63577-8.50022-X.
- C. Kunde, D. Michaels, J. Micovic, P. Lutze, A. Górak, and A. Kienle. Deterministic global optimization in conceptual process design of distillation and melt crystallization. *Chemical Engineering and Processing: Process Intensification*, 99:132–142, 2016. doi: 10.1016/j.cep.2015.09.010.
- A. Lewis, M. Seckler, H. Kramer, and G. van Rosmalen. *Industrial Crystallization - Fundamentals and Applications*. 2015.
- M. Locatelli and F. Schoen. *Global Optimization: Theory, Algorithms, and Applications*, volume 15. SIAM, 2013.
- J. Maćkowiak. *Fluid Dynamics of Packed Columns*. Springer-Verlag GmbH, Heidelberg, 2010.
- W. Marquardt, S. Kossack, and K. Kraemer. A framework for the systematic design of hybrid separation processes. *Chinese Journal of Chemical Engineering*, 16(3):333–342, 2008. doi: 10.1016/S1004-9541(08)60084-1.
- A. Mersmann, editor. *Crystallization Technology Handbook*. 2001.
- N. Mertens, C. Kunde, A. Kienle, and D. Michaels. A reformulation strategy for deterministic global optimization of ideal multi-component distillation

- processes. volume 38 of *Computer Aided Chemical Engineering*, pages 691–696. Elsevier, 2016. doi: 10.1016/B978-0-444-63428-3.50120-X.
- J. Micovic, T. Beierling, P. Lutze, G. Sadowski, and A. Górak. Design of hybrid distillation/melt crystallisation processes for separation of close boiling mixtures. *Chemical Engineering and Processing: Process Intensification*, 67:16–24, 2013. doi: 10.1016/j.cep.2012.07.012.
- J. Micovic, K. Werth, and P. Lutze. Hybrid separations combining distillation and organic solvent nanofiltration for separation of wide boiling mixtures. *Chemical Engineering Research and Design*, 92:2131–2147, 2014. doi: 10.1016/j.cherd.2014.02.012.
- R. Misener and C. A. Floudas. ANTIGONE: Algorithms for coNTinuous / Integer Global Optimization of Nonlinear Equations. *Journal of Global Optimization*, 59(2-3):503–526, 2014. doi: 10.1007/s10898-014-0166-2.
- M. Müller, V. A. Merchan, H. Arellano-Garcia, R. Schomäcker, and G. Wozny. A novel process design for the hydroformylation of higher alkenes. *Computer Aided Chemical Engineering*, 29:226–230, 2011. doi: 10.1016/B978-0-444-53711-9.50046-8.
- S. Münzberg, H. Lorenz, and Seidel-Morgenstern A. Multistage countercurrent crystallization for the separation of solid solutions. *Chemical Engineering and Technology*, 39(7):1242–1250, 2016.
- U. Nallasivam, V.H. Shah, A. A. Shenvi, M. Tawarmalani, and R. Agrawal. Global optimization of multicomponent distillation configurations: 1. need for a reliable global optimization algorithm. *AIChE Journal*, 59(3):971–981, 2013. doi: 10.1002/aic.13875.
- U. Nallasivam, V.H. Shah, A.A. Shenvi, J. Huff, M. Tawarmalani, and R. Agrawal. Global optimization of multicomponent distillation configurations: 2. Enumeration based global minimization algorithm. *AIChE Journal*, 62(6):2071–2086, 2016. ISSN 1547-5905. doi: 10.1002/aic.15204.
- A. Quaglia, C.L. Gargalo, S. Chairakwongsa, G. Sin, and R. Gani. Systematic network synthesis and design: Problem formulation, superstructure genera-

- tion, data management and solution. *Computers and Chemical Engineering*, 72:68–86, 2015. doi: 10.1016/j.compchemeng.2014.03.007.
- E. D. Sacerdoti. Planning in a hierarchy of abstraction spaces. *Artificial Intelligence*, 5(2):115–135, 1974.
- R. W. H. Sargent. A functional approach to process synthesis and its application to distillation systems. *Computers & Chemical Engineering*, 22(1-2): 31–45, 1998. doi: 10.1016/S0098-1354(96)00350-X.
- R. W. H. Sargent. Process systems engineering: A retrospective view with questions for the future. *Computers & Chemical Engineering*, 29(6 SPEC. ISS.):1237–1241, 2005. doi: 10.1016/j.compchemeng.2005.02.008.
- E. Schäfer, Y. Brunsch, G. Sadowski, and A. Behr. Hydroformylation of 1-dodecene in the thermomorphic solvent system dimethylformamide/decane. Phase behavior-reaction performance-catalyst recycling. *Industrial and Engineering Chemistry Research*, 51(31):10296–10306, 2012. doi: 10.1021/ie300484q.
- H. Schmid and A. Huber. Measuring a small number of samples, and the 3σ fallacy: Shedding light on confidence and error intervals. *IEEE Solid-State Circuits Magazine*, 6(2):52–58, Spring 2014. doi: 10.1109/MSSC.2014.2313714.
- M. Skiborowski, A. Harwardt, and W. Marquardt. Conceptual design of distillation-based hybrid separation processes. *Annual Review of Chemical and Biomolecular Engineering*, 4:45–68, 2013. doi: 10.1146/annurev-chembioeng-061010-114129.
- P. Stephan, K. Stephan, K. Schaber, and F. Mayinger. *Thermodynamik*. Springer, 2010. ISBN 9783540368557.
- M. Tawarmalani and N. V. Sahinidis. A polyhedral branch-and-cut approach to global optimization. *Mathematical Programming*, 103:225–249, 2005. doi: 10.1007/s10107-005-0581-8.
- G. Towler and R. Sinnott. *Chemical Engineering Design - Principles, Practice and Economics of Plant and Process Design*. Elsevier, 2008.

- J. Ulrich, J. Bierwirth, and S. Henning. Solid layer melt crystallization. *Separation & Purification Reviews*, 25(1):1–45, 1996. doi: 10.1080/03602549608006625.
- J. Viswanathan and I. E. Grossmann. Optimal feed locations and number of trays for distillation columns with multiple feeds. *Industrial & Engineering Chemistry Research*, 32(11):2942–2949, 1993. doi: 10.1021/ie00023a069.
- G. Wellinghoff and K. Wintermantel. Melt crystallization - theoretical pre-
sumptions and technical limitations [Schmelzkristallisation - theoretische
Voraussetzungen und technische Grenzen]. *Chemie-Ingenieur-Technik*, 63
(9):881–888, 89, 1991.
- J. G. Wijmans and R. W. Baker. The solution-diffusion model: a review. *Journal of Membrane Science*, 107:1–21, 1995.